

CMS Draft Analysis Note

The content of this note is intended for CMS internal use and distribution only

2019/02/28

Head Id: 479326

Archive Id: 490550M

Archive Date: 2018/10/25

Archive Tag: trunk

Search for stau production in the all-hadronic final state with 2016 and 2017 data

Maria Cepeda², Owen Colegrove¹, Valentina Dutta¹, Joseph Incandela¹, and Jan Steggemann²

¹ University of California, Santa Barbara

² CERN

Abstract

A search for tau slepton production in pp collisions at a center-of-mass energy of 13 TeV is presented. The data correspond to an integrated luminosity of 35.9 fb^{-1} collected with the CMS detector in 2016 and 41.5 fb^{-1} collected in 2017. The search is performed using events with two hadronically decaying tau leptons and a significant imbalance in the measured transverse momentum of the event.

This box is only visible in draft mode. Please make sure the values below make sense.

PDFAuthor:	M. Cepeda, O. Colegrove, V. Dutta, J. Incandela, J. Steggemann
PDFTitle:	Search for stau production in the all-hadronic final state with 2016 and 2017 data
PDFSubject:	CMS
PDFKeywords:	CMS, physics, SUSY

Please also verify that the abstract does not use any user defined symbols

1 Introduction

The standard model (SM) has been extremely successful at describing particle physics phenomena. Nevertheless, it suffers from shortcomings such as the hierarchy problem [1–6], the need for fine-tuned cancellations of large quantum corrections to keep the Higgs boson mass near the electroweak scale, and a failure to explain the observed abundance of dark matter. Supersymmetry (SUSY), based on a symmetry between bosons and fermions, is an attractive extension of the SM that solves some of these outstanding problems. SUSY introduces a superpartner for every SM particle, with identical quantum numbers with the exception of spin, which differs by one half unit. In R-parity conserving SUSY models [7, 8], supersymmetric particles are created in pairs, and the lightest supersymmetric particle (LSP) is stable [9, 10] and considered to be a candidate for dark matter [11].

SUSY may provide a “natural,” i.e. not fine-tuned, solution to the hierarchy problem through the cancellation of quadratic divergences in particle and sparticle loop corrections to the Higgs boson mass. In natural SUSY models, light top and bottom squarks with masses below a TeV are preferred, while the gluino is expected to have a mass of the order of a few TeV or less. Searches for the strong production of SUSY particles, such as third generation squarks and gluinos, were therefore a focal point of the LHC SUSY program at the start of Run-2. However, neither CMS or ATLAS have seen deviations from SM expectations in the context of these searches, and stringent limits of up to ≈ 1 (≈ 2) TeV on the top squark (gluino) mass have been placed [12, 13]. Probing the electroweak production of SUSY particles has been a greater challenge due to the relatively small production cross-section, as can be seen in Fig. 2 (left). With the growing LHC dataset at $\sqrt{s} = 13$ TeV (77.2 fb^{-1} collected by CMS in 2016 and 2017 and analyzed in this note) we now have improved sensitivity for these searches.

In natural SUSY models light third generation sparticles with masses close to the electroweak scale are preferred. In many SUSY scenarios $\tan(\beta)$ is large which constrains the τ slepton or stau ($\tilde{\tau}$), the supersymmetric partner of the τ lepton, to be lighter than the selectron and smuon, resulting in τ -rich final states. In particular, models where the $\tilde{\tau}$ is the next-to-lightest supersymmetric particle (NLSP) are well motivated in early universe neutralino co-annihilation scenarios. Co-annihilation processes can explain the observed relic density and favor a relatively light $\tilde{\tau}$ that has a small mass splitting with a bino LSP.

In this analysis, we examine simplified SUSY models of direct $\tilde{\tau}$ pair production, as shown in Fig. 1. We assume that the $\tilde{\tau}$ decays to a τ lepton and $\tilde{\chi}_1^0$. The most sensitive searches for direct $\tilde{\tau}$ pair production to date were performed at the CERN LEP [14]. At the CERN LHC, the ATLAS [15, 16] and CMS [17] Collaborations have both performed searches for direct and indirect $\tilde{\tau}$ production with 8 TeV LHC data, while CMS has carried out searches for direct $\tilde{\tau}$ pair production with early 13 TeV data [18, 19].

As can be seen in Fig. 2 (right), the cross section of direct $\tilde{\tau}$ pair production depends strongly on the chirality of the SM partner [20], while the experimental acceptance also changes considerably due to differences in the polarization of the τ leptons. We use the terms left- or right-handed $\tilde{\tau}$ to refer to a $\tilde{\tau}$ whose SM partner has left- or right-handed chirality respectively. In the case of a purely right-handed $\tilde{\tau}$, the decay products of hadronically decaying τ leptons originating from $\tilde{\tau}$ decays have larger visible transverse momentum (p_T) than in the purely left-handed scenario, while the reverse is true for leptonically decaying τ leptons. Three different scenarios of direct $\tilde{\tau}$ pair production are considered in this note: (i) a purely left-handed $\tilde{\tau}$ (LH), (ii) a purely right-handed $\tilde{\tau}$ (RH), and (iii) the degenerate production scenario wherein pairs of both right- and left-handed eigenstates are produced with the same $\tilde{\tau}$ mass.

In this analysis, we focus on the final state with two hadronically decaying τ leptons (τ_h). This analysis was previously performed with 2016 data as described in Refs. [18, 21]. It has been updated to incorporate the data collected in 2017. Several improvements have been introduced in this iteration, mainly the incorporation of an improved τ_h selection method developed using a deep neural network. Additionally, the background estimation techniques have been more extensively validated and the overall analysis structure has been reworked for greater sensitivity.

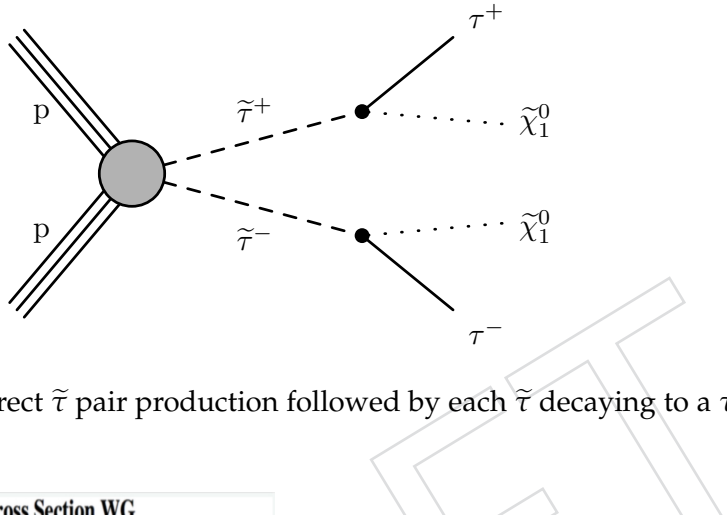


Figure 1: Diagram for direct $\tilde{\tau}$ pair production followed by each $\tilde{\tau}$ decaying to a τ lepton and $\tilde{\chi}_1^0$ (left).

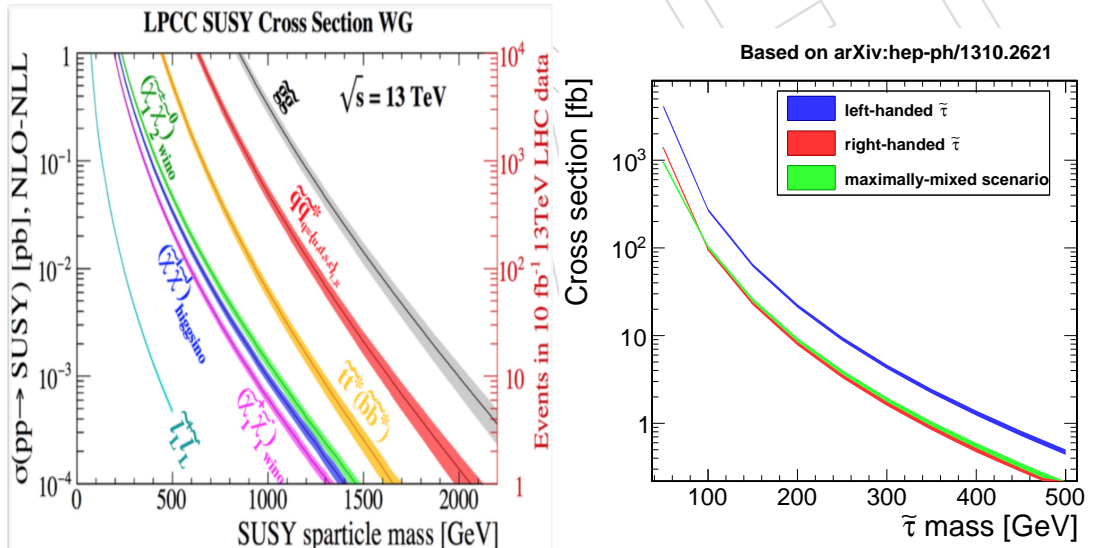


Figure 2: Left: Cross section for SUSY particle production at $\sqrt{s} = 13$ TeV. The curve corresponding to slepton pair production represents the production of purely left-handed sleptons (including staus). Right: cross section for direct $\tilde{\tau}$ pair production under different assumptions for the mixing of the left-handed and right-handed staus (based on [20]).

2 Triggers and datasets

The data for this search is recorded using a combination of di- τ_h triggers and p_T^{miss} triggers. The HLT paths corresponding to these triggers are listed in Table 1. The turn-on for the di- τ_h trigger is quite slow and does not achieve full efficiency at the plateau. We therefore recover some signal efficiency by including events with high p_T^{miss} recorded by the p_T^{miss} triggers. For

59 events with offline p_T^{miss} below 200 GeV, the di- τ_h triggers are used, while for those with offline
 60 p_T^{miss} above 200 GeV, the p_T^{miss} triggers are used. For the di- τ_h triggered events, we require
 61 a minimum offline p_T of 40 (45) GeV for the reconstructed τ_h in 2016 (2017), in order to be
 62 sufficiently far into the trigger turn on.

Table 1: HLT paths corresponding to the di- τ_h and p_T^{miss} triggers used to record events selected
 for the analysis in 2016 and 2017, as well as single muon triggers used to select events in the
 $\mu\tau_h$ final state. Not all trigger paths were available for the full data-taking period.

Data-taking period	HLT path
2016	HLT_DoubleMediumIsoPFTau35_Trk1_eta2p1_Reg
	HLT_DoubleMediumCombinedIsoPFTau32_Trk1_eta2p1_Reg
	HLT_PFMET120_PFMHT120_IDTight
	HLT_IsoMu22 or HLT_IsoMu24
2017	HLT_DoubleTightChargedIsoPFTau35_Trk1_TightID_eta2p1_Reg
	HLT_DoubleTightChargedIsoPFTau40_Trk1_eta2p1_Reg
	HLT_DoubleMediumChargedIsoPFTau40_Trk1_TightID_eta2p1_Reg
	HLT_PFMET120_PFMHT120_IDTight_PFHT60
	HLT_PFMETNoMu120_PFMHTNoMu120_IDTight_PFHT60
	HLT_PFMETTypeOne120_PFMHT120_IDTight_PFHT60
	HLT_PFMET140_PFMHT140_IDTight
	HLT_PFMETNoMu140_PFMHTNoMu140_IDTight
	HLT_PFMETTypeOne140_PFMHT140_IDTight
	HLT_IsoMu27 or HLT_IsoMu29

63 The di- τ_h trigger efficiencies have been measured by the trigger subgroup of the Tau POG. The
 64 efficiencies were measured using a tag-and-probe method in the $\mu\tau_h$ final state. The tag is an
 65 identified and isolated muon passing the single muon triggers, while the probe is a τ_h passing
 66 ID and isolation and matching to the τ_h leg of a $\mu\tau_h$ cross trigger corresponding to the same
 67 trigger requirements as in the di- τ_h triggers. In this way efficiencies are derived for the τ_h -leg
 68 of the $\mu\tau_h$ cross trigger. The corresponding data-MC scale factors for a very tight Tau POG
 69 MVA isolation cut are applied to each τ_h leg of the di- τ_h triggers. Studies in the supplementary
 70 Section F validate the application of these scale factors after cutting on the DeepPF isolation.
 71 The DeepPF isolation data-MC scale factor is also measured in an analogous way in the $\mu\tau_h$
 72 final state.

73 The p_T^{miss} trigger efficiency is measured in data with the help of an auxiliary, single electron trigger
 74 (HLT_Ele27_WPTight_Gsf in 2016, HLT_Ele32_WPTight_Gsf OR HLT_Ele32_WPTight_Gsf.L1DoubleEG
 75 in 2017). The denominator of the efficiency ratio is given by the number of events passing the
 76 auxiliary trigger and the following additional selection criteria. Events must have an electron
 77 with $p_T > 35$ GeV, passing tight selection criteria, that is within $\Delta R < 0.1$ of the trigger object
 78 that fired the electron trigger. The MET filters listed in Section 3.1.6 are also applied. In order to
 79 be close to the phase space of the analysis, we require the presence of at least two jets. Jets are
 80 only counted if they are at least $\Delta R = 0.4$ away from the electron trigger object. From this sam-
 81 ple, the numerator of the trigger efficiency ratio is then given by the number of events that also
 82 passed the search trigger. The two plots in Figure 3 show the trigger efficiency measured as a
 83 function of p_T^{miss} for 2016 and 2017 respectively. The p_T^{miss} trigger scale factor is obtained by tak-
 84 ing the ratio of scale factors obtained for data and simulation and is applied to the background
 85 and signal simulated samples.

86 The datasets used in the analysis are listed in Table 3 and the simulated Monte Carlo (MC)
 87 samples used for the background prediction for the 2016 and 2017 data analyses are listed in

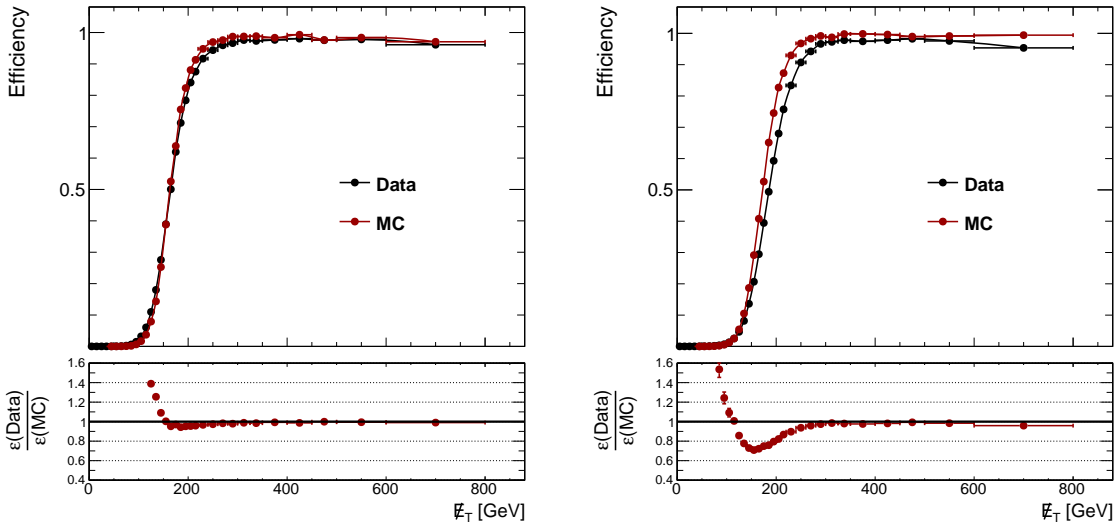


Figure 3: Measured p_T^{miss} trigger efficiencies in data and simulation for 2016 (2017) on the left (right).

Table 4 and Table 5 respectively. For the signal we use officially produced samples generated with MADGRAPH5_aMC@NLO for left-handed and right-handed scenarios with benchmark $\tilde{\tau}$ masses of 90, 100, 125, 150, 175, and 200 GeV and $\tilde{\chi}_1^0$ masses of 0, 10, and 20 GeV (Table 6). The full GEANT4-based detector simulation is used for all simulation samples (both signal and background).

3 Event selection

The event selection requires the presence of two reconstructed τ_h with opposite charge. We provide below a description of the selection criteria used for the different physics objects in this analysis, followed by a description of the baseline event selection and search region definitions.

3.1 Object selection

3.1.1 Vertex selection

The following standard CMS selection criteria are applied to interaction vertices reconstructed in an event:

- The vertices must come from fits to trajectories of reconstructed particle tracks with positive χ^2 values.
- There are at least 5 degrees of freedom in the vertex fit.
- The distance, absolute z , along the beam line from the nominal center of the detector is less than 24 cm.
- The transverse displacement, ρ , from the beam line is less than 2 cm.

Selected events are required to have at least one vertex fulfilling these requirements. The reconstructed vertex with the largest value of summed physics-object p_T^2 is taken to be the primary pp interaction vertex (PV) from which the physics objects used in this analysis originate. The physics objects are the jets, clustered using the jet finding algorithm [22, 23] with the tracks assigned to the vertex as inputs, and the associated missing transverse momentum, taken as the negative vector sum of the p_T of those jets.

Table 2: Datasets used in the 2016 analysis.

Dataset
/Tau/Run2016B-03Feb2017-ver1-v2/MINIAOD
/Tau/Run2016B-03Feb2017-ver2-v2/MINIAOD
/Tau/Run2016C-03Feb2017-v1/MINIAOD
/Tau/Run2016D-03Feb2017-v1/MINIAOD
/Tau/Run2016E-03Feb2017-v1/MINIAOD
/Tau/Run2016F-03Feb2017-v1/MINIAOD
/Tau/Run2016G-03Feb2017-v1/MINIAOD
/Tau/Run2016H-03Feb2017-ver2-v1/MINIAOD
/Tau/Run2016H-03Feb2017-ver3-v1/MINIAOD
/MET/Run2016B-03Feb2017_ver1-v1/MINIAOD
/MET/Run2016B-03Feb2017_ver2-v2/MINIAOD
/MET/Run2016C-03Feb2017-v1/MINIAOD
/MET/Run2016D-03Feb2017-v1/MINIAOD
/MET/Run2016E-03Feb2017-v1/MINIAOD
/MET/Run2016F-03Feb2017-v1/MINIAOD
/MET/Run2016G-03Feb2017-v1/MINIAOD
/MET/Run2016H-03Feb2017_ver2-v1/MINIAOD
/MET/Run2016H-03Feb2017_ver3-v1/MINIAOD
/SingleMuon/Run2016B-03Feb2017_ver1-v1/MINIAOD
/SingleMuon/Run2016B-03Feb2017_ver2-v2/MINIAOD
/SingleMuon/Run2016C-03Feb2017-v1/MINIAOD
/SingleMuon/Run2016D-03Feb2017-v1/MINIAOD
/SingleMuon/Run2016E-03Feb2017-v1/MINIAOD
/SingleMuon/Run2016F-03Feb2017-v1/MINIAOD
/SingleMuon/Run2016G-03Feb2017-v1/MINIAOD
/SingleMuon/Run2016H-03Feb2017_ver2-v1/MINIAOD
/SingleMuon/Run2016H-03Feb2017_ver3-v1/MINIAOD

Table 3: Datasets used in the 2017 analysis.

Dataset
/Tau/Run2017B-31Mar2018-v1/MINIAOD
/Tau/Run2017C-31Mar2018-v1/MINIAOD
/Tau/Run2017D-31Mar2018-v1/MINIAOD
/Tau/Run2017E-31Mar2018-v1/MINIAOD
/Tau/Run2017F-31Mar2018-v1/MINIAOD
/MET/Run2017B-31Mar2018-v1/MINIAOD
/MET/Run2017C-31Mar2018-v1/MINIAOD
/MET/Run2017D-31Mar2018-v1/MINIAOD
/MET/Run2017E-31Mar2018-v1/MINIAOD
/MET/Run2017F-31Mar2018-v1/MINIAOD
/SingleMuon/Run2017B-31Mar2018-v1/MINIAOD
/SingleMuon/Run2017C-31Mar2018-v1/MINIAOD
/SingleMuon/Run2017D-31Mar2018-v1/MINIAOD
/SingleMuon/Run2017E-31Mar2018-v1/MINIAOD
/SingleMuon/Run2017F-31Mar2018-v1/MINIAOD

Table 4: Simulated samples used for the background prediction in the analysis of 2016 data. The Moriond17 datasets are used.

Category	Sample name	Cross section [pb]
DY+jets	DYJetsToLL_M-50_TuneCUETP8M1_13TeV-madgraphMLM-pythia8	5765.4
DY+jets	DY1JetsToLL_M-50_TuneCUETP8M1_13TeV-madgraphMLM-pythia8	1231.20
DY+jets	DY2JetsToLL_M-50_TuneCUETP8M1_13TeV-madgraphMLM-pythia8	404.685
DY+jets	DY3JetsToLL_M-50_TuneCUETP8M1_13TeV-madgraphMLM-pythia8	123.789
DY+jets	DY4JetsToLL_M-50_TuneCUETP8M1_13TeV-madgraphMLM-pythia8	66.6368
DY+jets	DYJetsToLL_M-10to50_TuneCUETP8M1_13TeV-madgraphMLM-pythia8	18610
Top	TTTo2L2Nu_TuneCUETP8M2_ttHtranche3_13TeV-powheg-pythia8	87.315
Top	ST_tW_antitop_5f_NoFullyHadronicDecays_13TeV-powheg-pythia8_TuneCUETP8M1	19.6
Top	ST_tW_top_5f_NoFullyHadronicDecays_13TeV-powheg-pythia8_TuneCUETP8M1	19.6
Top	TTWJetsToLNu_TuneCUETP8M1_13TeV-amcatnloFXFX-madspin-pythia8	0.204
Top	TTZToLLNuNu_M-10_TuneCUETP8M1_13TeV-amcatnlo-pythia8	0.253
Other SM	ZZTo2L2Nu_13TeV_powheg_pythia8	0.564
Other SM	ZZTo2L2Q_13TeV_amcatnloFXFX_madspin_pythia8	3.22
Other SM	ZZTo4L_13TeV_amcatnloFXFX_pythia8	1.212
Other SM	WZTo2L2Q_13TeV_amcatnloFXFX_madspin_pythia8	5.6
Other SM	WZTo3LNu_TuneCUETP8M1_13TeV-powheg_pythia8	4.43
Other SM	WWTo2L2Nu_13TeV-powheg	10.481
Other SM	WWW_4F_TuneCUETP8M1_13TeV-amcatnlo-pythia8	0.209
Other SM	WWZ_TuneCUETP8M1_13TeV-amcatnlo-pythia8	0.165
Other SM	WZZ_TuneCUETP8M1_13TeV-amcatnlo-pythia8	0.056
Other SM	ZZZ_TuneCUETP8M1_13TeV-amcatnlo-pythia8	0.014
Other SM	GluGluHToTauTau_M125_13TeV_powheg_pythia8	2.78
Other SM	ZHToTauTau_M125_13TeV_powheg_pythia8	0.0532144
Other SM	WplusHToTauTau_M125_13TeV_powheg_pythia8	0.0340648
Other SM	WminusHToTauTau_M125_13TeV_powheg_pythia8	0.0549587

Table 5: Simulated samples used for the background prediction in the analysis of 2017 data. The 12Apr2018 re-miniAOD datasets are used.

Category	Sample name	Cross section [pb]
DY+jets	DYJetsToLL_M-50_TuneCP5_13TeV-madgraphMLM-pythia8	5765.4
DY+jets	DY1JetsToLL_M-50_TuneCP5_13TeV-madgraphMLM-pythia8	1070.5
DY+jets	DY2JetsToLL_M-50_TuneCP5_13TeV-madgraphMLM-pythia8	375.03
DY+jets	DY3JetsToLL_M-50_TuneCP5_13TeV-madgraphMLM-pythia8	147.11
DY+jets	DY4JetsToLL_M-50_TuneCP5_13TeV-madgraphMLM-pythia8	49.741
Top	TTTo2L2Nu_TuneCP5_13TeV-powheg_pythia8	87.31
Top	TTToSemiLeptonic_TuneCP5_PSweights_13TeV-powheg_pythia8	364.36
Top	ST_tW_antitop_5f_NoFullyHadronicDecays_TuneCP5_13TeV-powheg_pythia8	19.56
Top	ST_tW_antitop_5f_NoFullyHadronicDecays_TuneCP5_13TeV-powheg_pythia8	19.56
Top	ST_tW_top_5f_inclusiveDecays_TuneCP5_13TeV-powheg_pythia8	19.56
Top	TTWJetsToLNu_TuneCP5_13TeV-amcatnloFXFX-madspin-pythia8	0.2125
Top	TTZToLLNuNu_M-10_TuneCP5_13TeV-amcatnlo-pythia8	0.2432
Other SM	ZZTo2L2Nu_13TeV_powheg_pythia8	0.60
Other SM	ZZTo2L2Q_13TeV_amcatnloFXFX_madspin_pythia8	5.07
Other SM	ZZTo4L_13TeV_amcatnloFXFX_pythia8	1.325
Other SM	WZTo2L2Q_13TeV_amcatnloFXFX_madspin_pythia8	9.24
Other SM	WZTo3LNu_TuneCUETP8M1_13TeV-powheg_pythia8	4.43
Other SM	WWTo2L2Nu_13TeV-powheg	4.9
Other SM	WWW_4F_TuneCUETP8M1_13TeV-amcatnlo-pythia8	0.209
Other SM	WWZ_TuneCUETP8M1_13TeV-amcatnlo-pythia8	0.165
Other SM	WZZ_TuneCUETP8M1_13TeV-amcatnlo-pythia8	0.056
Other SM	ZZZ_TuneCUETP8M1_13TeV-amcatnlo-pythia8	0.014
Other SM	GluGluHToTauTau_M125_13TeV_powheg_pythia8	2.78
Other SM	ZHToTauTau_M125_13TeV_powheg_pythia8	0.0532144
Other SM	WplusHToTauTau_M125_13TeV_powheg_pythia8	0.0340648
Other SM	WminusHToTauTau_M125_13TeV_powheg_pythia8	0.0549587

3.1.2 Tau candidate selection

The main background after the baseline selection consists of QCD multijet, W+jets, Drell-Yan+jets, and top quark events. Separating the background into prompt τ_h events, where both

Table 6: Simulated signal samples used for 2016 and 2017 analyses. The Moriond17 campaign was used for 2016 samples, and the 12Apr2018 MiniAOD is used for 2017.

Signal model	Sample name	Cross section [pb]
2016		
Direct $\tilde{\tau}$ pair, left-handed	SMS-TStauStau.lefthanded.TuneCUETP8M1_13TeV-madgraphMLM-pythia8	mass-dependent
Direct $\tilde{\tau}$ pair, right-handed	SMS-TStauStau.righthanded.TuneCUETP8M1_13TeV-madgraphMLM-pythia8	mass-dependent
2017		
Direct $\tilde{\tau}$ pair, left-handed	SMS-TStauStau.lefthanded.TuneCP5_13TeV-madgraphMLM-pythia8	mass-dependent
Direct $\tilde{\tau}$ pair, right-handed	SMS-TStauStau.righthanded.TuneCP5_13TeV-madgraphMLM-pythia8	mass-dependent

116 reconstructed taus are matched to a generator τ_h , and misidentified events, where one or more
 117 non-generator matched jets has been misidentified as prompt τ_h , we find that the misidentified
 118 background dominates our search regions. This background can be reduced by applying
 119 stringent isolation requirements on the τ_h candidates.

120 The τ_h candidates are reconstructed using the CMS hadron-plus-strips (HPS) algorithm [24, 25].
 121 The constituents of the reconstructed jets are used to identify three distinct τ lepton decay
 122 modes wherein the τ lepton decays to one charged hadron (decay mode 0), one charged hadron
 123 and a neutral pion (decay mode 1), or three charged hadrons (decay mode 10). Electrons and
 124 muons misidentified as τ_h are suppressed using dedicated criteria based on the consistency be-
 125 tween the measurements in the tracker, calorimeters, and muon detectors [25, 26]. The presence
 126 of extra particles within the jet, not compatible with the reconstructed decay mode, is used as
 127 a criterion to discriminate τ_h decays from other jets. A multivariate (MVA) discriminator [26],
 128 which contains isolation as well as lifetime information, is provided by the Tau POG for this
 129 purpose, and provides an efficiency of around 70% for genuine τ_h , with a misidentification
 130 rate of approximately 1% for light-quark or gluon jets corresponding to a “very loose” working
 131 point. In order to further improve the suppression of the fake jet background while retaining
 132 high signal efficiency, we have pursued a new approach for improved τ_h isolation, based on the
 133 use of a deep neural network (DNN) using the properties of PF candidates within an isolation
 134 cone ($\Delta R < 0.5$) around the τ_h candidate. We refer to this approach as the “Deep Particle Flow”
 135 (DeepPF) isolation. The criteria used to select τ_h candidates in this analysis are as follows [27]:

- $p_T > 40(45)$ GeV for 2016 (2017)
- $|\eta_{\tau_h}| < 2.1$
- matched to one of the legs of the trigger for di- τ_h triggered events
- decay mode finding: one-prong, one-prong + π_0 s, or three-prong
- very loose anti-electron discriminator (againstElectronVLooseMVA6)
- loose anti-muon discriminator (againstMuonLoose3)
- very loose MVA isolation
- tight requirement on the DeepPF isolation discriminator, described below

144 The DeepPF isolation is based on information from the PF candidates within a $\Delta R < 0.5$ cone
 145 around the τ_h candidate as follows:

- charged candidates matched to the PV with $p_T > 0.5$ GeV
- neutral particle candidates with $p_T > 0.5$ GeV

148 The list of particle features incorporated for each candidate includes: candidate p_T relative to
 149 the τ_h jet, $\Delta R(\text{candidate}, \tau_h)$, PDG ID, d_{xy} , d_z , $\sigma(d_{xy})$, $\sigma(d_z)$, and other track quality information.
 150 For the purposes of training the DNN, signal τ_h candidates are truth-matched to generator-
 151 level τ leptons in simulated samples of $Z/\gamma^* \rightarrow \tau\tau$, $Z' \rightarrow \tau\tau$, and MSSM $\Phi \rightarrow \tau\tau$ events.
 152 Background candidates are taken from simulated W+jets and QCD multijet event samples. A

convolutional neural network is ensembled with the nominal POG MVA to obtain the final discriminator value for the optimal performance. Figure 4 shows a comparison of the ROC curve obtained for the DeepPF isolation in simulated events passing the baseline selection with the nominal POG MVA isolation. The DeepPF isolation provides a significant improvement in the rejection of fake τ_h backgrounds for the same signal efficiency. Appendix Section A provides a more complete explanation of the algorithmic implementation.

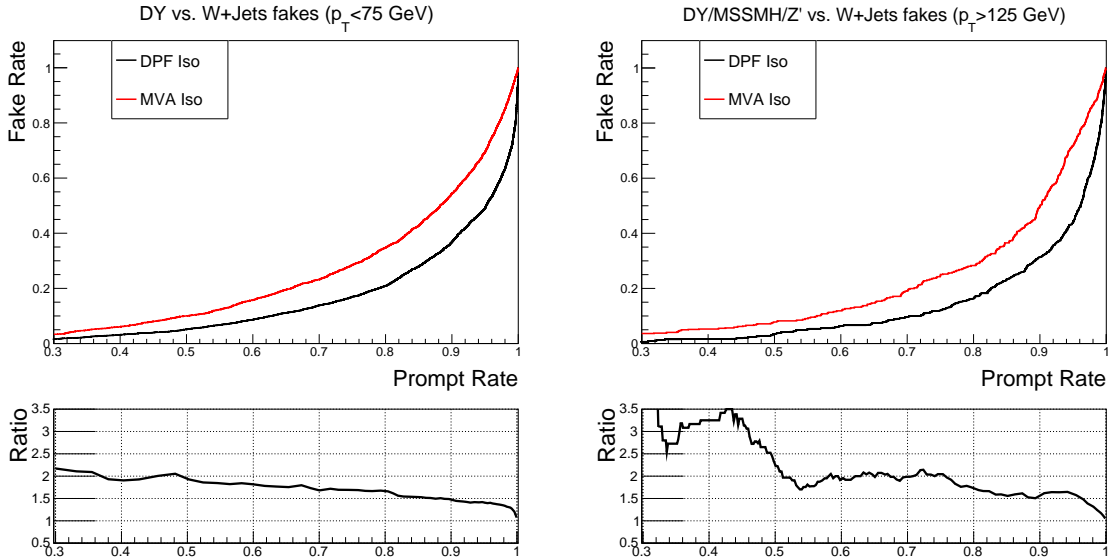


Figure 4: ROC curve for the DeepPF isolation (red), compared with corresponding curve for the nominal POG MVA isolation (black). The comparison has been carried out using fake and prompt τ_h candidates coming from events passing the loose analysis baseline. Left: the genuine τ_h efficiency is evaluated for truth-matched τ leptons in simulated $Z/\gamma^* \rightarrow \tau\tau$ events, while the misidentification probability is evaluated for fake candidates in simulated $W+jets$ and $t\bar{t}$ events satisfying $p_T(\tau_h) < 75$ GeV. Right: the signal sample is expanded to include $Z' \rightarrow \tau\tau$, and MSSM $\Phi \rightarrow \tau\tau$ events and the τ_h candidate p_T is increased by requiring $p_T(\tau_h) > 125$ GeV.

A tight working point for the DeepPF isolation is chosen to maintain a flat efficiency of $\approx 70, 80$, and 80% vs p_T for decay modes 0, 1, and 10, respectively. The corresponding fake rate to pass the very loose MVA is 1-2%, depending upon p_T . The fake rate is then reduced by an additional 15-20% by including the DeepPF isolation, resulting in a 0.15-0.4% fake rate overall. The trend in discriminator threshold vs p_T needed to maintain these constant efficiencies by decay mode is seen to be approximately linear (Fig. 5). We therefore carry out a linear fit to these distributions and obtain the working points for the DeepPF isolation as tabulated in Table 7.

Table 7: DeepPF working points used in this analysis.

Decay Mode	Working Point
1-Prong	$DeepPF(\tau_h) > 0.898328 - 0.000160992 * p_T(\tau_h)$ [GeV]
1-Prong+ π^0	$DeepPF(\tau_h) > 0.910138 - 0.000229923 * p_T(\tau_h)$ [GeV]
3-Prong	$DeepPF(\tau_h) > 0.873958 - 0.0002328 * p_T(\tau_h)$ [GeV]

3.1.3 $\mu\tau_h$ event selection

The validation of the DeepPF isolation is performed in $\mu\tau_h$ events that are selected from among those passing a single muon trigger. We select events with an isolated muon passing the

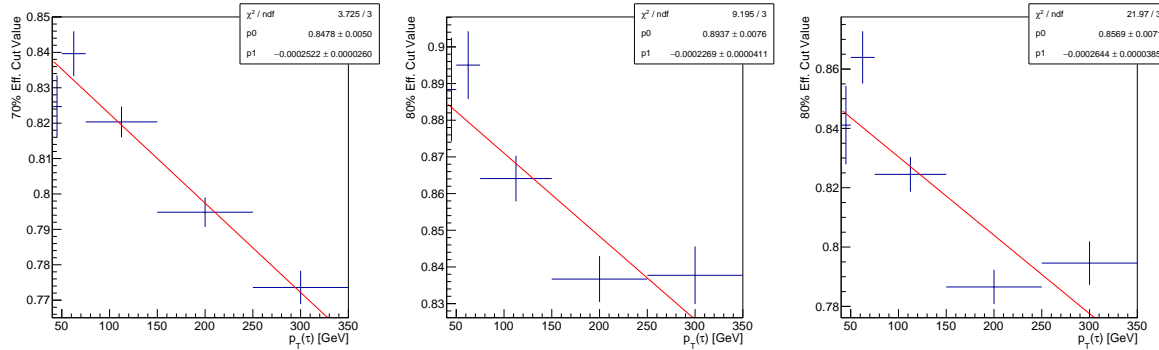


Figure 5: DeepPF discriminator threshold vs p_T needed to maintain a constant efficiency of 70, 70, and 80% for decay modes 0, 1, and 10, respectively, from left to right, for generator matched reconstructed τ_h passing the loose MVA isolation. A clear linear trend can be seen in these plots and the resulting fit, which is used to obtain the working points for this analysis.

170 medium cut-based selection and $p_T >= 24(29)$ GeV in 2016 (2017), and a τ_h candidate of op-
 171 posite charge, with $p_T > 30$ GeV, passing the very loose anti-electron discriminator, the loose
 172 anti-muon discriminator, and the loose MVA isolation as a preselection. Pile-up, b-tagging effi-
 173 ciency, LO Drell-yan mass and p_T (Section 4.2), and muon isolation and trigger corrections are
 174 applied to the selected MC events. The contribution from QCD events is estimated by inverting
 175 the SS region after subtracting the expected MC contamination and scaling the yields by 8% to
 176 account for the SS to OS QCD transfer factor. A baseline selection of $M_{vis}(\mu, \tau) >= 50$ GeV is
 177 then applied.

178 Figure 6 shows the visible $\mu\tau_h$ mass distribution corresponding to the passing candidates for
 179 the tight DeepPF isolation working point in 2016 and 2017. A significant increase in genera-
 180 tor matched efficiency for roughly the same number of fake events is seen with the DeepPF
 181 isolation in this sample. A data/MC efficiency scale factor of $0.93(0.96) \pm 0.05$ in 2016 (2017)
 182 is evaluated from this sample and is propagated throughout the analysis. Studies included
 183 in the appendix show that within statistical uncertainties, there is no evidence for any addi-
 184 tional dependence on either p_T or decay mode (Appendix, Fig. 25 and Fig. 57). As additional
 185 validation we show the distribution of the two machine learning scores that are averaged to
 186 form the DeepPF isolation discriminator after applying the measured isolation SFs to events
 187 passing the baseline $\mu\tau_h$ selection described above (Appendix, Fig. 24, 23). Compareable or
 188 better agreement is seen for the deep-neural network discriminant, and all input variables ap-
 189 pear to be reasonably well modeled (Appendix Section A). These studies confirm that by using
 190 the DeepPF isolation we benefit from a significant decrease in the τ_h misidentification rate for
 191 the same efficiency with respect to the Tau POG MVA isolation, and that the approach is well
 192 validated in data.

193 The tau energy scale in MC is corrected according to measurements from the Tau POG. The
 194 measured shifts are -0.5 (0.7)%, 1.1 (-0.3) %, 0.6 (-1) % for one prong, one prong + π_0 , and
 195 three prong decays, respectively, in 2016 (2017). An uncertainty in this correction of 1.2 % is
 196 propagated through to the final results.

197 3.1.4 Electron and muon veto

198 To keep the analysis disjoint from the complementary analysis in the semi-leptonic decay
 199 channels and reduce rare standard model backgrounds (dibosons, $t\bar{t} + V$), we apply a veto on
 200 muons (electrons) with $p_T > 10$ GeV and $|\eta| < 2.4(2.5)$. The muons have to pass the loose

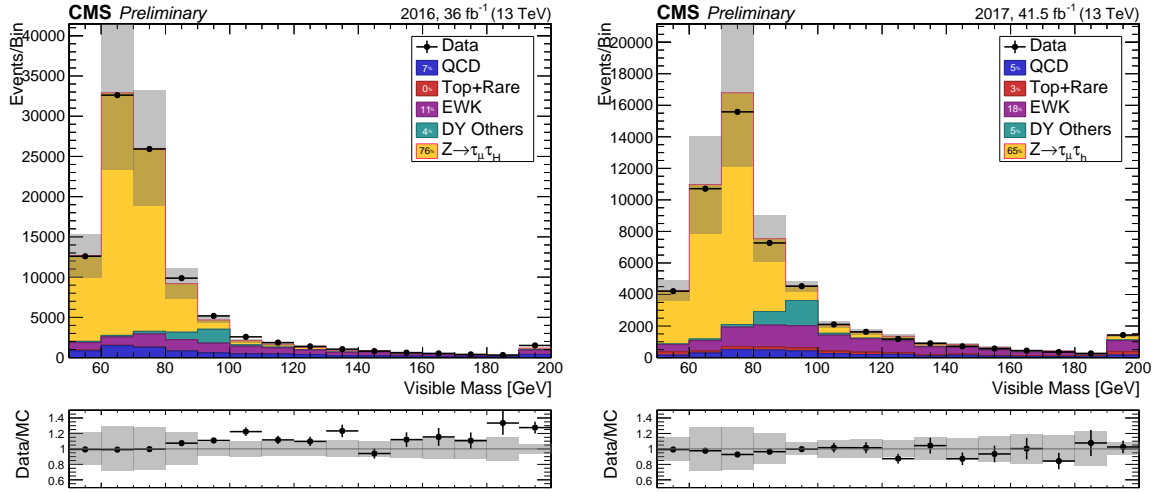


Figure 6: Visible mass spectrum for an inclusive sample of $\mu\tau_h$ events passing the selection described in 3.1.3. The probe tau in these event passes the DeepPF isolation working point in 2016 and 2017 (left and right respectively). On the left a scale factor of 0.93 has been applied whereas a scale factor of 0.96 has been applied on the right.

201 POG muon selection and a $\Delta\beta$ -corrected relative isolation cut of 0.3 [28]. For the electrons the
 202 POG-recommended cut-based medium selection is applied [29]. The isolation calculated for
 203 electrons mitigated for the effects of pileup via an effective area correction using the average
 204 energy density.

205 3.1.5 Jets

206 Jets are reconstructed using the anti- k_T algorithm, with a distance parameter of 0.4. They are
 207 required to have $p_T > 30 \text{ GeV}$, $|\eta| < 2.4$ and satisfy the loose jet ID working point. B-tagged
 208 jets are identified with the loose working point of the DeepCSV b-tagging algorithm. Jets are
 209 cleaned with respect to the selected tau leptons. We veto events with at least one (loosely)
 210 b-tagged jet.

211 3.1.6 E_T^{miss}

212 The E_T^{miss} is calculated as the negative vector sum of all particle flow (PF) candidates recon-
 213 structed in the event. We use type-1 corrected E_T^{miss} , where the jet energy corrections are ap-
 214 plied to the jets in the E_T^{miss} calculation. The lightest supersymmetric particles leave the detector
 215 undetected and therefore create additional E_T^{miss} in the signal events. This characteristic is ex-
 216 ploited by using M_T and M_{T2} -like variables.

217 We apply the following E_T^{miss} filters as recommended by the JetMET group:

- 218 • primary vertex filter
- 219 • CSC beam halo filter
- 220 • HBHE noise filter
- 221 • HBHEiso noise filter
- 222 • ee badSC noise filter (2016 only)
- 223 • ECAL TP filter
- 224 • bad PF muon filter
- 225 • bad charged hadron filter

226 • ECAL bad calibration filter (2017 only)

227 In 2017 an issue relating to the forward ECAL readout resulted in additional noise. This re-
 228 sulted in a significant discrepancy between data and MC. This discrepancy is mitigated by
 229 removing forward jets with raw $p_T < 50$ GeV and $2.65 < |\eta| < 3.139$ from the E_T^{miss} calculation
 230 in both data and MC. This results in significantly improved data/MC agreement, but it comes
 231 at the cost of degraded performance (Appendix Section G). For the systematic uncertainties
 232 relating to E_T^{miss} in 2017, we also neglect jets in this region.

233 To mitigate the increased background coming from this redefinition of p_T^{miss} for the 2017 anal-
 234 ysis, we introduce a new variable, $H_T(\text{Soft,Forward})$, which is defined as the H_T of the jets
 235 neglected from the p_T^{miss} V2 calculation. Events with large $H_T(\text{Soft,Forward})$ may contain gen-
 236 uine underlying soft activity which in turn is not included in the p_T^{miss} calculation, and therefore
 237 backgrounds associated with Drell–Yan and misidentified τ_h are increased. To control this new
 238 background we introduce a veto: $H_T(\text{Soft,Forward}) < 50$ GeV after correcting the distribution
 239 in simulation for the discrepancies observed between data and simulation (see Appendix).

240 Finally, in order to avoid effects related to jet mismeasurement that can contribute to fake p_T^{miss} ,
 241 we require jets to have a minimum separation in $|\Delta\phi|$ of 0.25 from \vec{p}_T^{miss} , for jets with $p_T >$
 242 30 GeV and $|\eta| < 2.4$ and for jets with uncorrected $p_T > 50$ GeV in the region $2.4 < |\eta| < 3.139$.

243 **3.2 Baseline selection**

244 The baseline event selection is defined by requiring two isolated τ_h candidates of opposite
 245 charge fulfilling the selection requirements described above, and no additional τ_h candidates
 246 with $p_T > 30$ GeV passing the very loose MVA selection. We veto events with additional elec-
 247 trons or muons, and reject any events with a b-tagged jet in order to suppress top quark related
 248 backgrounds.

249 **3.3 Discriminating variables**

250 In order to further improve discrimination against the SM background, we take advantage of
 251 the expected presence of two $\tilde{\chi}_1^0$ in the final state for signal events, which would lead to addi-
 252 tional p_T^{miss} . The correlations between \vec{p}_T^{miss} and the reconstructed leptons are expected to be
 253 different between signal and background processes, even those with genuine p_T^{miss} , and these
 254 differences can be exploited. In particular, mass observables that can be calculated from the
 255 reconstructed leptons and the \vec{p}_T^{miss} provide strong discriminants between signal and back-
 256 ground. For a mother particle decaying to a visible and an invisible particle, the transverse
 257 mass (M_T), calculated using only the \vec{p}_T of the decay products, should have a kinematic end-
 258 point at the mass of the mother particle. Assuming that the p_T^{miss} corresponds to the p_T of the
 259 invisible particle, we calculate the M_T observable for the visible particle q and the invisible
 260 particle as follows:

$$M_T(q, \vec{p}_T^{\text{miss}}) \equiv \sqrt{2p_{T,q}p_T^{\text{miss}}(1 - \cos \Delta\phi(\vec{p}_{T,q}, \vec{p}_T^{\text{miss}}))}. \quad (1)$$

261 In this analysis we only utilize the sum of the transverse mass between each tau and p_T^{miss} ,
 262 $\Sigma M_T = M_T(\tau_1, p_T^{\text{miss}}) + M_T(\tau_2, p_T^{\text{miss}})$. Another discriminating variable found to be useful in
 263 the discrimination of signal against background is the “stransverse mass” M_{T2} [30, 31]. This
 264 kinematic mass variable is a generalization of the variable M_T for situations with multiple
 265 invisible particles. It serves as an estimator of the mass of pair-produced particles in situations
 266 in which both particles decay to a final state containing the same invisible particle. For direct

267 $\tilde{\tau}$ pair production, with both $\tilde{\tau}$ decaying to a τ lepton and a $\tilde{\chi}_1^0$, M_{T2} should be correlated with
 268 the $\tilde{\tau}$ mass. Large values of M_{T2} can therefore be used to discriminate between models with
 269 large $\tilde{\tau}$ masses and the SM background. This variable is again calculated using the \vec{p}_T of the
 270 different particles:

$$M_{T2} = \min_{\vec{p}_T^{X(1)} + \vec{p}_T^{X(2)} = \vec{p}_T^{\text{miss}}} \left[\max \left(M_T^{(1)}, M_T^{(2)} \right) \right], \quad (2)$$

271 where $\vec{p}_T^{X(i)}$ (with $i=1,2$) are the unknown transverse momenta of the two undetected particles
 272 and $M_T^{(i)}$ are the transverse masses obtained by pairing any of the two invisible particles with
 273 one of the two leptons. The minimization is done over the possible momenta of the invisible
 274 particles, which should add up to the \vec{p}_T^{miss} in the event.

275 3.4 Cut-and-count selection

276 The SR selections for this analysis, shown in Table 8, are based on a cut-and-count approach
 277 after applying the baseline selection and $|\Delta\phi(\tau_{h1}, \tau_{h2})| > 1.5$, a requirement that suppresses
 278 background events while retaining high signal efficiency. The regions are defined by selections
 279 on the following quantities: M_{T2} , ΣM_T , N_{jet} (the number of reconstructed jets in an event).

280 An initial selection of $M_{T2} > 25$ GeV is required for all prompt SRs. After applying this mini-
 281 mum M_{T2} requirement, the ΣM_T distribution is exploited to provide sensitivity towards a large
 282 range of $\tilde{\tau}$ mass signals. We define three bins in ΣM_T : [200,250), [250,300), [300, ∞) GeV. We
 283 then subdivide events in each ΣM_T region into the following categories based on N_{jet} : $N_{\text{jet}} = 0$,
 284 and $N_{\text{jet}} \geq 1$. This binning is highly beneficial as background events passing the SR kinematic
 285 selections are largely characterized by additional jet activity, while in the case of signal very few
 286 events have additional jets. The 0-jet category therefore provides us with nearly background-
 287 free SRs. However, we retain the SRs with $N_{\text{jet}} \geq 1$ in order to avoid losing any signal sensitivity
 288 from the presence of signal events in these SRs. Finally, we subdivide all ΣM_T and N_{jet} regions
 289 into two M_{T2} regions: low M_{T2} (25–50 GeV) and high M_{T2} (> 50 GeV), which provide enhanced
 290 sensitivity for low and high mass $\tilde{\tau}$ signals respectively. Figure 7 shows distributions of N_{jet}
 291 and $|\Delta\phi(\tau_{h1}, \tau_{h2})|$ after the baseline selection for simulated signal and background events, as
 292 well as distributions for M_{T2} and ΣM_T for events in the 0-jet search category.

293 **N.B.: the displaced category has been removed from the analysis for this iteration pending fur-
 294 ther studies, however for the current SRs, targeting prompt signals, we still retain the orthog-
 295 onalization against the displaced tau region by inverting the displaced category requirements:
 296 both τ_h with absolute values of IP3D above 0.01 and absolute d_{xy} significance above 5.**

297 We also define several validation regions (VRs) corresponding to each SR but with orthogonal
 298 selections in order to validate the background estimation methods in signal-depleted regions.
 299 These VRs are chosen by inverting the $\Delta\phi(\tau_{h1}, \tau_{h2}) > 1.5$ cut, τ_h pair opposite sign requirement,
 300 or b jet veto, in order to provide regions enriched in the different background processes. Table 9
 301 contains the definitions for these validation regions.

302 4 Background estimation

303 The largest background in the analysis originates from QCD multijet and W+jets processes,
 304 where one or more of the τ_h candidates comes from a jet and is misidentified as a prompt τ_h .

Table 8: Definition of the search regions used in this analysis.

High M_{T2} SRs	Selections (After Baseline, $ \Delta\phi(\tau, \tau) > 1.5, M_{T2} > 50$ GeV)
SR-HighMT-EQ0J	$\Sigma M_T \in [300, \infty]$ GeV and $N_{jet} = 0$
SR-HighMT-GEQ1J	$\Sigma M_T \in [300, \infty]$ GeV and $N_{jet} \geq 1$
SR-MidMT-EQ0J	$\Sigma M_T \in [250, 300]$ GeV and $N_{jet} = 0$
SR-MidMT-GEQ1J	$\Sigma M_T \in [250, 300]$ GeV and $N_{jet} \geq 1$
SR-LowMT-EQ0J	$\Sigma M_T \in [200, 250]$ GeV and $N_{jet} = 0$
SR-LowMT-GEQ1J	$\Sigma M_T \in [200, 250]$ GeV and $N_{jet} \geq 1$
Low M_{T2} SRs	Selections (After Baseline, $ \Delta\phi(\tau, \tau) > 1.5, 25 < M_{T2} < 50$ GeV)
SR-HighMT-EQ0J-lowMT2	$\Sigma M_T \in [300, \infty]$ GeV and $N_{jet} = 0$
SR-HighMT-GEQ1J-lowMT2	$\Sigma M_T \in [300, \infty]$ GeV and $N_{jet} \geq 1$
SR-MidMT-EQ0J-lowMT2	$\Sigma M_T \in [250, 300]$ GeV and $N_{jet} = 0$
SR-MidMT-GEQ1J-lowMT2	$\Sigma M_T \in [250, 300]$ GeV and $N_{jet} \geq 1$
SR-LowMT-EQ0J-lowMT2	$\Sigma M_T \in [200, 250]$ GeV and $N_{jet} = 0$
SR-LowMT-GEQ1J-lowMT2	$\Sigma M_T \in [200, 250]$ GeV and $N_{jet} \geq 1$

Table 9: Definition of the validation regions used in this analysis.

VR Selection Menu	Note : Each region is binned in ΣM_T and N_J where applicable
Low M_{T2} VR	Nominal analysis with new selection $< M_{T2} < 25$ GeV
High M_{T2} Same-Sign VR	Nominal analysis with inverted sign selection
Low M_{T2} Same-Sign VR	Nominal analysis with inverted sign and M_{T2} selection
High M_{T2} B-Enriched VR	Nominal analysis with inverted jet selections
Low M_{T2} B-Enriched VR	Nominal analysis with inverted jet and M_{T2} selections
High M_{T2} Small $\Delta\phi$ VR	Nominal analysis with modified selection $.5 < \Delta\phi(\tau_h, \tau_h) < 1.5$

305 This background is predicted using a data-driven method. The second largest background
 306 originates from Drell-Yan events. We correct the Z boson mass and p_T spectrum based on a
 307 comparison in $Z \rightarrow \mu\mu$ events and assign an uncertainty for this correction. We also evaluate
 308 the other relevant systematic uncertainties and verify the corrections in a dedicated control
 309 region. Finally we have some other smaller contributions from SM backgrounds, like Higgs
 310 boson and diboson production and top pair production (with or without extra vector bosons).
 311 Those are estimated from simulation, using the normal suite of experimental and theoretical
 312 uncertainties.

313 4.1 Non-prompt and misidentified tau leptons

314 For non-prompt and misidentified tau leptons coming from jets (dominantly from QCD and
 315 W+jets) we use a fake rate method. We use a sideband of loosely isolated tau candidates to
 316 predict the amount of tau candidates passing the tight isolation requirement in our final se-
 317 lection. We use a QCD-enriched region with same-charge τ_h candidates to measure the fake
 318 rates. Since the τ_h isolation has a considerable inefficiency, we have to take this inefficiency
 319 into account when calculating the fake rates.

320 The τ_h fake rate depends on the flavor and p_T of the mother parton and the decay mode of the
 321 jet. We bin our measured fake rates in p_T and τ_h decay mode to remove the dependence on these

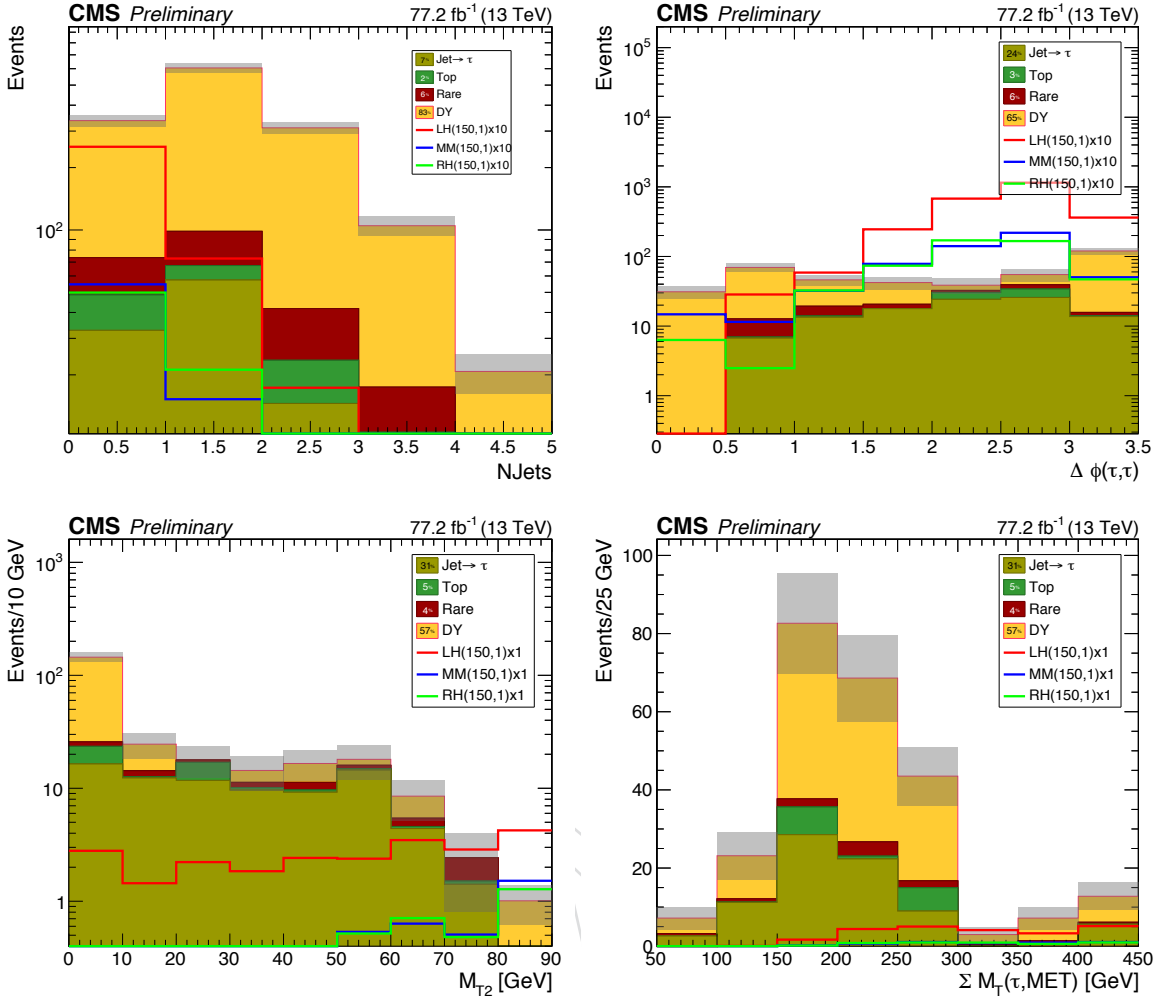


Figure 7: Distributions of variables used to define the SRs for simulated background and signal events. Top left: N_{jet} after baseline selection, Top right : $|\Delta\phi(\tau_1, \tau_2)|$ after the baseline selection and the requirement $N_{\text{jet}} = 0$. Bottom row: M_{T2} and $\sum M_{\text{T}}$ in the $N_{\text{jet}} = 0$ category, after requiring $|\Delta\phi(\tau_1, \tau_2)| > 1.5$. The signal distributions shown are for benchmark points with a $\tilde{\tau}$ mass of 150 GeV and a $\tilde{\chi}_1^0$ mass of 1 GeV, corresponding to left-handed (LH), right-handed (RH) and maximally-mixed (MM) scenarios. The signal cross sections are scaled by a factor of 10 for the plots in the upper row.

322 effects, as well as in the number of primary vertices (N_{PV}) to capture the effects of pileup. We
 323 still suffer from possible differences in fake rate due to the different jet flavors. By requiring the
 324 tau fakeable objects to be loosely isolated (passing the MVA VLoose working point) however,
 325 the jet flavor dependence is significantly reduced. Figure 8 shows the p_{T} dependence of the
 326 fake rate for different jet flavors as measured in simulation. Since we cannot determine the
 327 jet flavor in data, we vary the fake rate up and down by a factor of 30% and propagate the
 328 uncertainty to cover the residual jet flavor dependence.

329 4.1.1 Fake rate measurement in data

330 We measure the fake rate in a QCD control region, consisting of events with two same-sign
 331 τ_h candidates. The denominator fakeable objects are required to pass the very loose MVA
 332 selection. We also require $M_{\text{T2}} < 40 \text{ GeV}$ to avoid any possible signal contamination and to

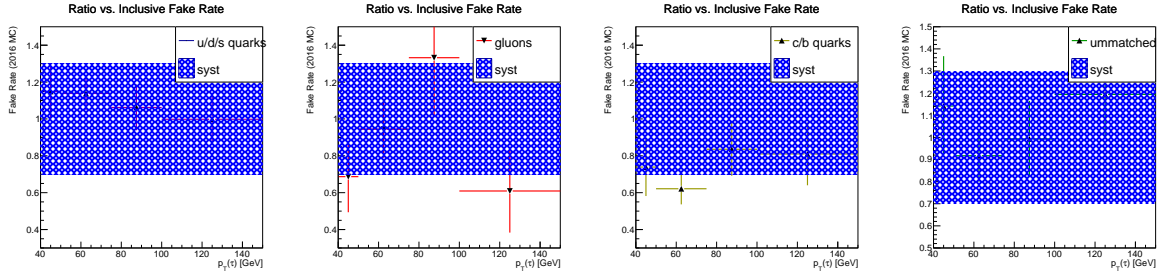


Figure 8: The p_T dependence of the fake rate on the parton flavor. A systematic uncertainty to cover the dependence of the fake rate on jet parton flavor is derived by re-calculating the fake rate yields after varying the per-object fake rate up and down by a factor of 30%.

reduce the contribution of W+jets in this control region. The measurement is binned in τ_h decay mode and p_T , as well as in N_{PV} , as shown in Fig. 9 and for 2016 and 2017. Dedicated studies were performed to illustrate the strong variance in fake rate as a function of N_{PV} and the absence of variation in fake rate as a function of M_{T2} (Appendix, Fig. 55).

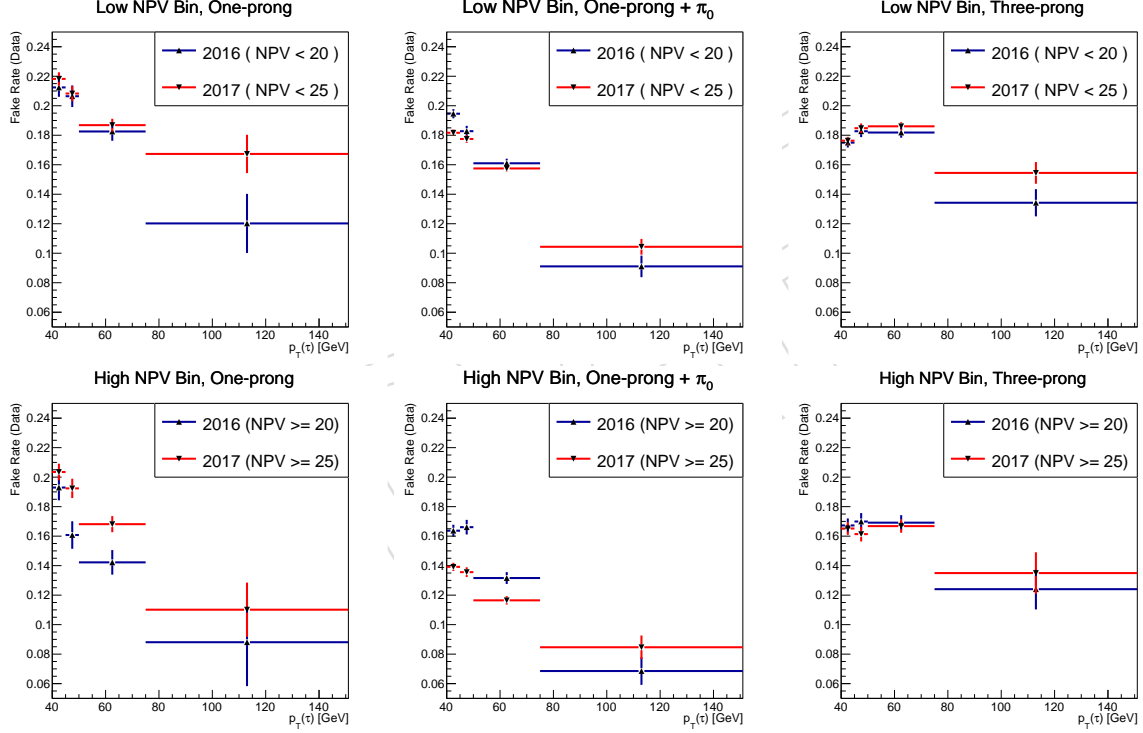


Figure 9: Fake rates measured in (2016, 2017) data for the different τ_h decay modes (left: one-prong, middle: one-prong+ π_0 , right: three-prong) as a function of τ_h p_T , for $N_{PV} < (20, 25)$ (upper row) and $N_{PV} \geq (20, 25)$ (lower row).

4.1.2 Fake rate calculation

Since the isolation efficiency for prompt τ_h candidates is only around 70-80%, processes with genuine τ_h may leak into the data sideband regions and need to be taken into account when calculating the final estimate for the background processes with misidentified τ_h . To take this correctly into account, we define three categories for events that have at least two loosely isolated τ_h candidates: events with both τ_h candidates passing the very tight isolation requirement (N_{tt}), events with one passing and one failing the very tight isolation requirement (N_{tl}), and finally events with both τ_h candidates failing the very tight isolation requirement (N_{ll}).

We then equate these observable quantities with the expected sum totals of contributions from events with two prompt τ_h candidates, two misidentified τ_h candidates, or one prompt and one misidentified τ_h candidate to each of these populations. The contributions of background events with one or two misidentified τ_h candidates in the SRs can then be determined analytically by inverting this set of equations, using the measured prompt efficiencies and fake rates. The system of equations used is shown below, and follows the prescription described in AN-2010-261 [32] where more detail is given about the analytical calculation:

$$\begin{aligned} N &= N_{pp} + N_{pf} + N_{ff} = N_{tt} + N_{tl} + N_{ll} \\ N_{ll} &= (1-p)^2 N_{pp} + (1-p)(1-f)N_{pf} + (1-f)^2 N_{ff} \\ N_{tl} &= 2p(1-p)N_{pp} + [f(1-p) + p(1-f)] N_{pf} + 2f(1-f)N_{ff} \\ N_{tt} &= p^2 N_{pp} + pfN_{pf} + f^2 N_{ff} \end{aligned} \quad (3)$$

Here p is the prompt rate, f the fake rate, N_{pp} the number of events with two real prompt τ_h , N_{pf} the number of events with one real prompt τ_h and one τ_h candidate coming from a jet, N_{ff} the number of events with both τ_h candidates coming from a jet. Our signal region yield will be N_{tt} . The background contribution to the term $p^2 N_{pp}$ (the prompt backgrounds) are taken from simulation with corrections applied.

By inverting this set of equations, we can calculate the number of events with two prompt τ_h , with one prompt and one fake τ_h and with two fake τ_h :

$$\begin{aligned} N_{pp} &= \frac{1}{(p-f)^2} [(1-f)^2 N_{tt} - f(1-f)N_{tl} + f^2 N_{ll}] \\ N_{pf} &= \frac{1}{(p-f)^2} [-2fpN_{ll} + [f(1-p) + p(1-f)] N_{tl} - 2(1-p)(1-f)N_{tt}] \\ N_{ff} &= \frac{1}{(p-f)^2} [p^2 N_{ll} - p(1-p)N_{tl} + (1-p)^2 N_{tt}] \end{aligned} \quad (4)$$

The corresponding backgrounds surviving the tight selection cuts are then pfN_{pf} for single-fake events and f^2N_{ff} for double-fake events, respectively. In our case the single-fake events are mostly W+jets events, while the double fakes come from QCD multijet processes.

The closure of the method is checked as a function of M_{T2} in same-charge di- τ_h events, after requiring $p_T(\tau_{h1}, \tau_{h2}) > 50$ GeV in order to be closer to our phase space of interest. Since this sample overlaps with the sample where the fake rates were measured, we expect very good agreement, however differences could occur at high values of M_{T2} , where the fraction of W+jets events increases. Figure 10 (left) shows very good agreement across the full M_{T2} distribution, even in the tails. We also validate the background prediction in an opposite-charge di- τ_h validation region, selected with $p_T(\tau_{h1}, \tau_{h2}) > 50$ GeV, and $\Sigma M_T < 250$ GeV or $M_{T2} < 50$ GeV in order to be orthogonal to the SR selection (Fig. 10 right). Again, very good agreement is seen between data and the background prediction across the full M_{T2} spectrum.

4.2 Drell-Yan background

The Drell-Yan background is taken from data-corrected simulation. If the Z boson p_T spectrum is incorrectly described, or the amount of off-shell Z bosons is badly modeled in the simulation, then this can affect the E_T^{miss} and M_{T2} distribution, especially at the high-end tail. Therefore we

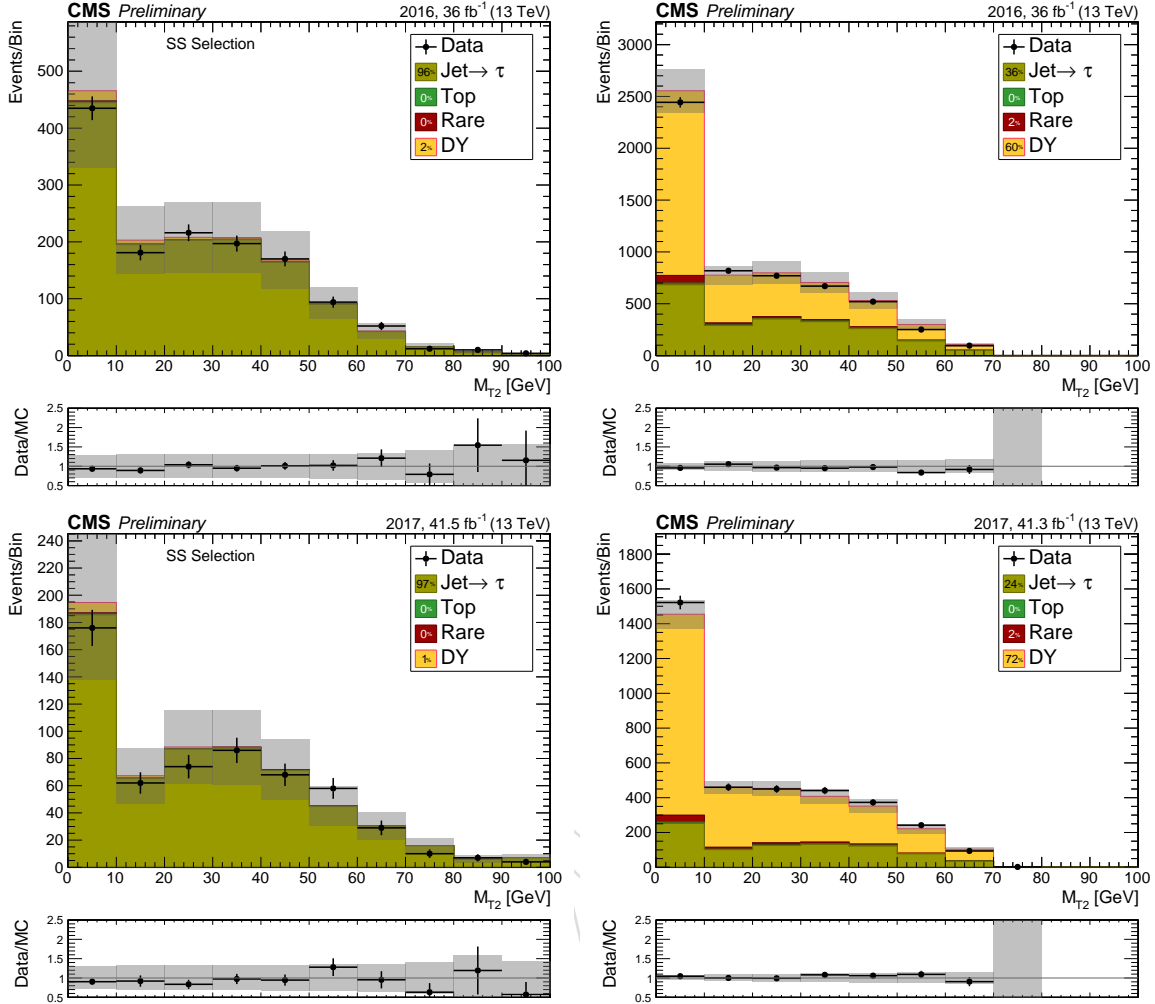


Figure 10: Closure test for the fake rate method in same-sign events (left) and validation of the background prediction in opposite-sign (right) events for 2016 (top row) and 2017 (bottom row). We see very good agreement for the M_{T2} spectrum in all cases.

measure the Z boson mass and p_T spectra in $Z \rightarrow \mu\mu$ data and then apply the corrections to the simulation. Fig. 56 shows the mass and p_T comparison for DY before applying corrections, the derived correction factors, and a comparison between 2016 and 2017 corrections. Aside from this, the standard experimental uncertainties (e.g. jet energy scale and efficiency) are evaluated since those can also effect our final Drell-Yan background estimate. The detailed numbers are shown in Sec. 5.

A cross-check in a $Z \rightarrow \tau\tau$ validation region is added. We require the p_T of the di- τ_h system to be at least 50 GeV to reduce the QCD multijet background and then compare the visible mass spectrum between data and the background prediction. After correcting for the known efficiency differences between data and simulation we observe good agreement within the experimental uncertainties as can be seen in Figs. 10, 11. Additional studies of E_T^{miss} , ΣM_T , and other relevant kinematics are relegated to the Appendix Figs. 57, 58, 59.

4.3 Top background

Top related backgrounds corresponding to $t\bar{t}$ and other more exotic process, such as single top, are taken from simulation. The agreement between data and simulation is performed by

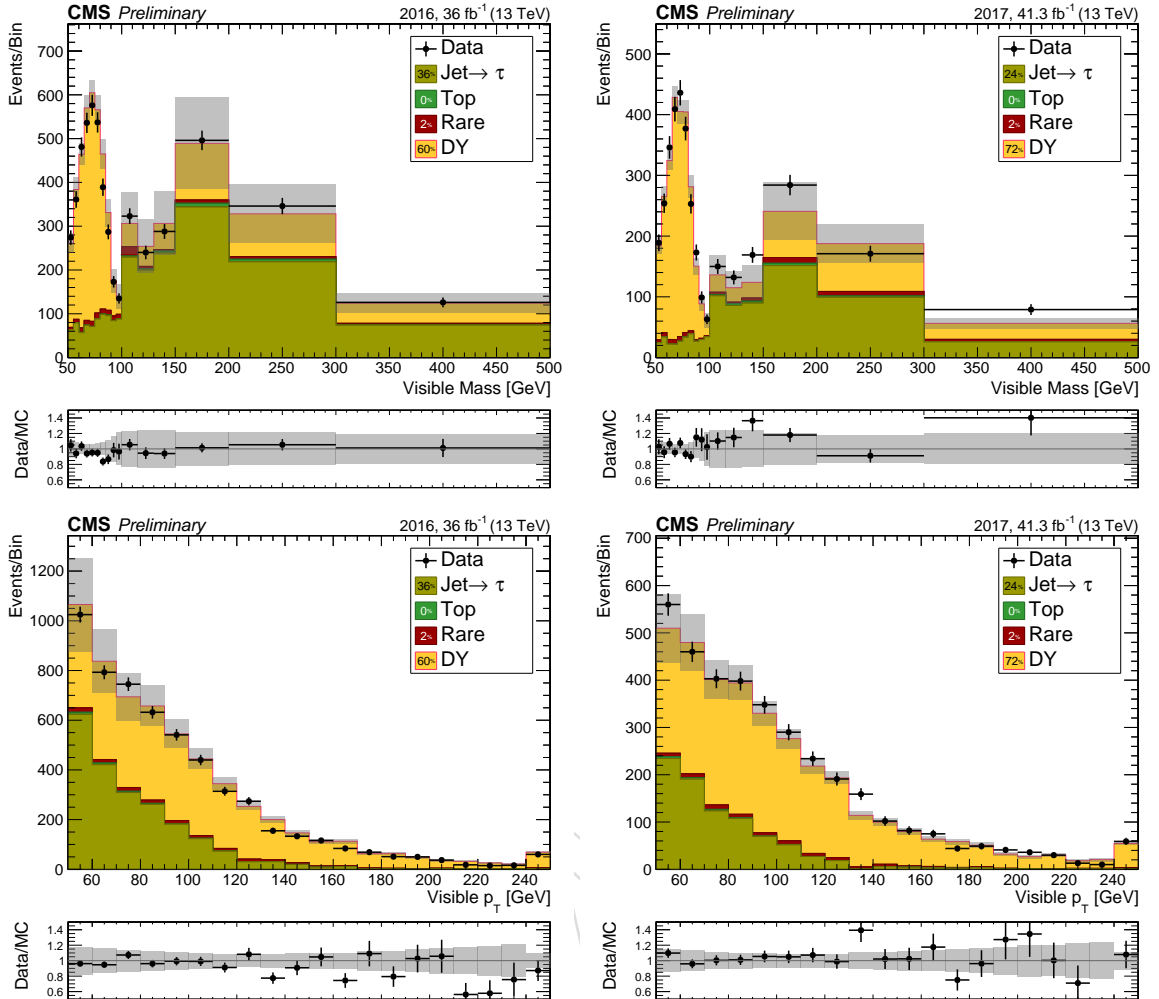


Figure 11: The visible mass and the visible $p_T(Z)$ spectrum in data and the corresponding prediction for the SM background for 2016 (left) and 2017 (right) agrees within the experimental uncertainties. The events shown above pass the di-tau validation region selection described in 4.2.

390 inverting the nominal b-jet requirement. After studying the tau and p_T^{miss} related kinematics in
 391 this region (Figure 12) no evidence was found that any background specific corrections to the
 392 simulation are necessary. A dedicated top kinematic validation region is created by inverting
 393 the loose b-jet baseline selection. In addition to the baseline we require $p_T^{\text{miss}} > 50$ GeV and
 394 requiring $M_{\text{vis}} > 100$ GeV. More detailed studies are again relegated to the Appendix (Figs. 60,
 395 61, 62).

396 4.4 Remaining small SM backgrounds

397 The remaining small SM backgrounds consist of Higgs boson production, di- and triboson pro-
 398 duction. All these backgrounds are rather minor and difficult to isolate, therefore we estimate
 399 them purely from simulation. The theoretical and experimental uncertainties are evaluated and
 400 propagated through to the final background estimate.

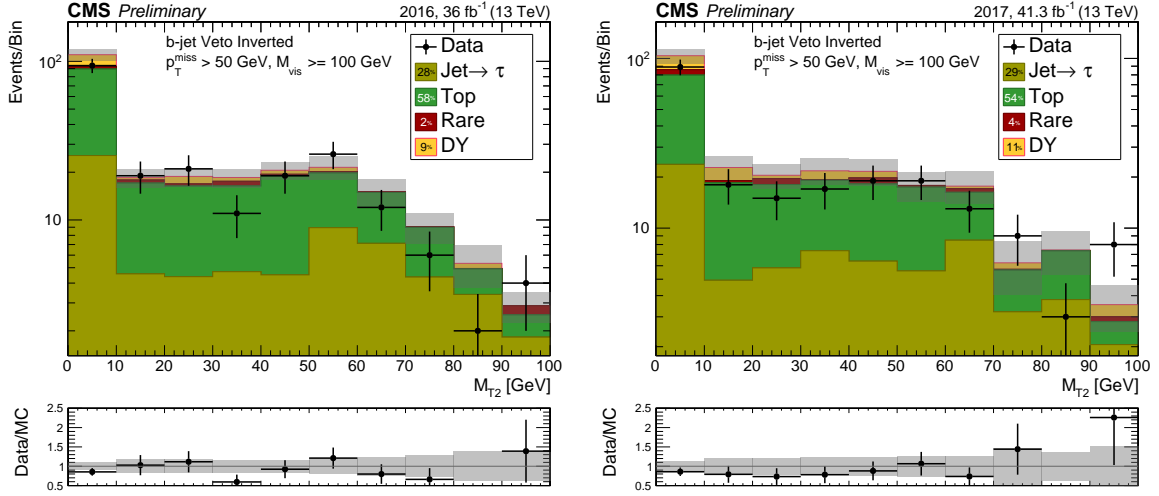


Figure 12: Validation of the top background is carried out in the M_{T2} spectrum after applying the selections described in Section 4.3.

4.5 Validation

In Appendix D, we show distributions of the relevant kinematic variables in a DY and fake enriched control region specified by selecting events passing the baseline selection, with $p_T(\tau_h, \tau_h) > 50 \text{ GeV}$, and $\sum M_T < 250 \text{ GeV}$ or $M_{T2} < 50 \text{ GeV}$. Tables 16 and 17 provided the observed and predicted event yields in the SR-specific validation regions defined in Table 9. These results are also shown below in Fig. 13.

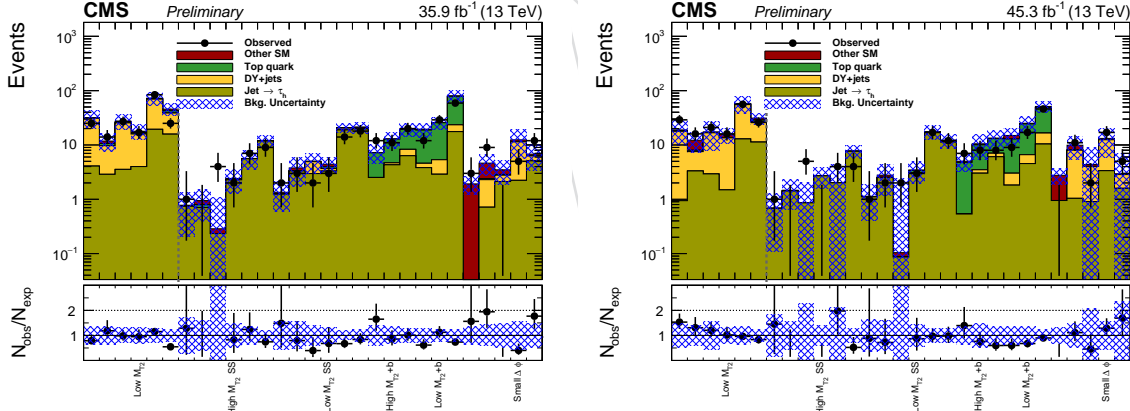


Figure 13: Observed and predicted event yields in the SR-specific validation regions for 2016 (left) and 2017 (right).

5 Systematic uncertainties

The two dominant uncertainties in this analysis are the statistical uncertainty driven by the limited event counts in the data sidebands or simulated samples used to obtain the background estimates, and the systematic uncertainty (30%) on the data-driven fake background estimate that covers the dependence of the fake rate on jet flavor.

For the other background estimates we rely mostly on simulation. We take a 15% normalization uncertainty for the cross section uncertainties based on CMS differential cross section measurements. For the τ_h selection (trigger and identification), we assign a 5% uncertainty

415 per τ_h . For high $p_T \tau_h$, with $p_T > 150 \text{ GeV}$, we assign an additional asymmetric uncertainty
 416 evaluated as $p_T(\tau_h)/1 \text{ TeV} * 5(35) \%$ up (down) as recommended by the Tau POG, although
 417 no significant deviations in data-MC agreement are observed in the high p_T region. There is a
 418 1.2% uncertainty on the tau energy scale for 2016, taken as uncorrelated across decay modes,
 419 that has a considerable effect on the estimated yields in the search regions. For 2017, this un-
 420 certainty was 0.8–0.9%, depending on decay mode. For the DY+jets estimate, we propagate
 421 an uncertainty corresponding to the mass and p_T corrections derived from a $Z \rightarrow \mu\mu$ sample.
 422 Since these corrections are meant to account for missing higher order corrections in the sim-
 423 ulation, we assign an uncertainty based on a comparison of LO and NLO shapes in simulation.
 424 We also propagate through b-tagging uncertainties, renormalization and factorization scale un-
 425 certainties, PDF uncertainties and uncertainties on jet energy scale, jet energy resolution, un-
 426 clustered energy. For pileup reweighting, we propagate an uncertainty derived by varying the
 427 MinBias cross section used to derive pileup reweighting factors by $\pm 5\%$. In general, we fol-
 428 low the recipes documented in [https://twiki.cern.ch/twiki/bin/viewauth/CMS/
 429 SUSRecommendationsMoriond17](https://twiki.cern.ch/twiki/bin/viewauth/CMS/SUSRecommendationsMoriond17).

430 For signal events, we improve the modeling of initial-state radiation (ISR) by reweighting the
 431 $p_{T,\text{ISR}}$ distribution (evaluated as the p_T of the di- $\tilde{\tau}$ system) using correction factors derived from
 432 comparisons of the Z p_T distribution between data and simulation. We take the deviation of
 433 the reweighting factors from 1 as a systematic uncertainty.

434 We also take into account the uncertainty in the integrated luminosity measurement for sig-
 435 nals and background estimates obtained from simulation. This uncertainty corresponds to 2.5
 436 (2.3)% for 2016 (2017).

437 In general we treat all statistical uncertainties as uncorrelated and systematic uncertainties re-
 438 lated to the same modeling effect are taken to be correlated across the different background
 439 predictions and signal predictions. Between the 2016 and 2017 data analyses, we treat all un-
 440 certainties deriving from statistical limitations as uncorrelated, and all systematic uncertainties
 441 as correlated.

Table 10: Uncertainties in the analysis affecting signal and the different SM backgrounds.

Uncertainty	signal	Jets to Fakes	Drell-Yan	Top	Rare SM
Tau Efficiency	10–20%	–%	10–30%	10–13%	10–22%
Fake rate	–	30–60%	–	–	–
Tau energy scale	0–35%	–	0–33%	0–28%	0–34%
Jet energy scale	0–50%	–	0–24%	0–25%	0–20%
Jet energy resolution	0–75%	–	0–95%	0–53%	1–19%
Unclustered energy	0–55%	–	0–27%	0–100%	0–35%
B-tagging	0.5–1%	–	0–5%	0–27%	0–1%
Scale	0.5–6%	–	4–8%	8–24%	8–13%
PDF	–	–	1–2%	0.5–1.5%	±1%
PileUp	0–20%	–	0–20%	0–10%	1–5%
DY cross section	–	–	15%	–	–
Top cross section	–	–	–	15%	–
Rare SM cross section	–	–	–	–	15%
Luminosity	2.3–2.5%	–	2.3–2.5%	2.3–2.5%	2.3–2.5%

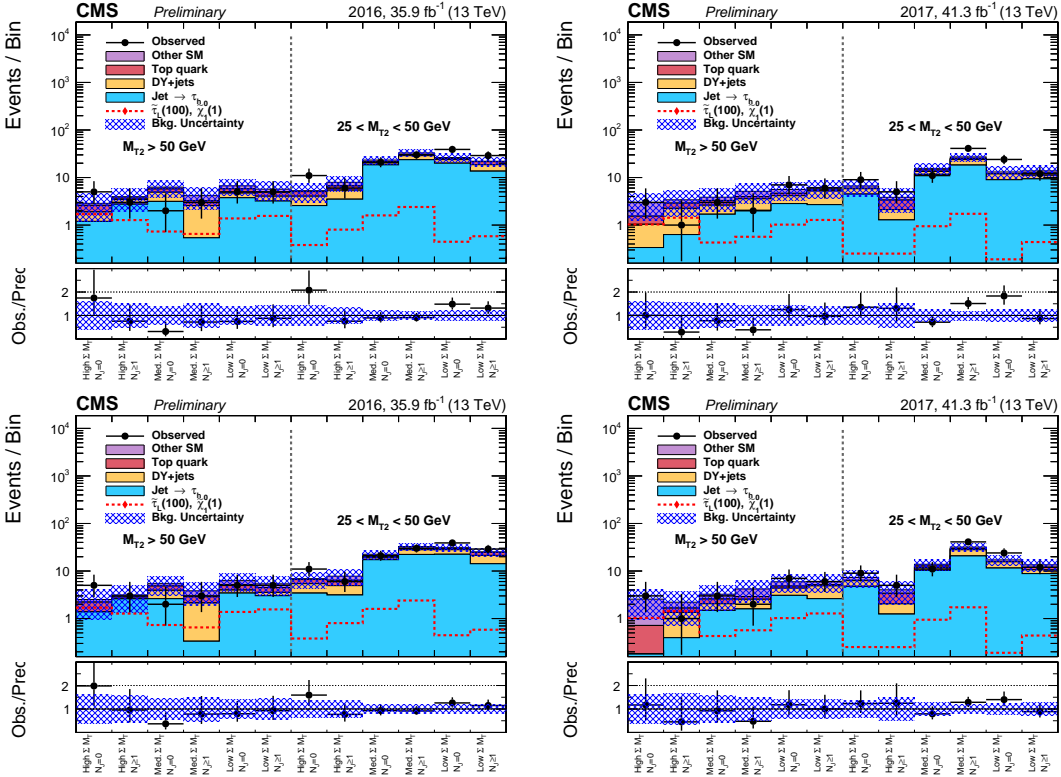


Figure 14: Observed and predicted event yields in each SR for 2016 (left) and 2017 (right) before and after fitting to background (top, bottom, respectively).

6 Results

The observed and predicted event yields for each SR are shown in Fig. 14. Table 11 summarizes the results for 2016 and Table 12 those from 2017. The background is predominantly composed of events with misidentified τ_h and the largest uncertainty originates from the statistical uncertainties affecting the background estimates. Listed in Tables 13, 14 are the expected bin-by-bin signal yields for degenerate $\tilde{\tau}$ pair production (simultaneous production of LH and RH $\tilde{\tau}$ pairs for a given $\tilde{\tau}$ mass) assuming a nearly massless $\tilde{\chi}_1^0$.

7 Interpretation

The results are interpreted as limits on the production of $\tilde{\tau}$ pairs in the context of simplified models [33–36]. We assume that the $\tilde{\tau}$ decays with 100% branching fraction to a τ lepton and a $\tilde{\chi}_1^0$. The 95% confidence level (CL) upper limits on SUSY production cross sections are calculated using a modified frequentist approach with the CL_S criterion [37, 38] and asymptotic results for the test statistic [39, 40]. We use all the exclusive search regions in a full statistical combination. The expected 95% CL cross section upper limits are shown in Fig. 15–17 for the considered range of $\tilde{\tau}$ masses in the degenerate, purely left-handed, and purely right-handed $\tilde{\tau}$ scenarios respectively. In general, constraints are reduced for higher values of the $\tilde{\chi}_1^0$ mass, due to the smaller experimental acceptance. In the degenerate scenario, we exclude $\tilde{\tau}$ masses up to 200 GeV for a nearly massless $\tilde{\chi}_1^0$. In the purely left-handed scenario, a $\tilde{\tau}$ mass of around 125 GeV is excluded. These are the first exclusion limits placed on direct $\tilde{\tau}$ pair production in this scenario since LEP [14].

Table 11: Predicted background yields and observed event counts in all $\tau_h \tau_h$ SRs, corresponding to 35.9 fb^{-1} of data collected in 2016. For the background estimates with no events in the sideband or the simulated sample, the 68% statistical upper limit is taken. The uncertainties listed in quadrature are statistical and systematic respectively. We also list the predicted signal yields corresponding to a $\tilde{\tau}$ mass of 150 GeV and a $\tilde{\chi}_1^0$ mass of 1 GeV.

Search Region	Misidentified τ_h	DY+jets	Top quark	Other SM	Total Pred.	Obs.	$m(\tilde{\tau}_L) = 100 \text{ GeV}$
	$M_{T2} > 50 \text{ GeV}$						
$300 < \Sigma M_T, N_J = 0$	$1.1 \pm 0.6 \pm 0.6$	< 0.7	$0.7 \pm 0.2 \pm 0.1$	$0.3 \pm 0.1 \pm 0.1$	$2.1 \pm 0.6 \pm 0.6$	5	$1.7 \pm 0.2 \pm 0.4$
$300 < \Sigma M_T, N_J >= 1$	$2.9 \pm 0.8 \pm 1.6$	$1.3 \pm 0.8 \pm 0.5$	$0.8 \pm 0.2 \pm 0.1$	$0.5 \pm 0.2 \pm 0.2$	$5.5 \pm 1.2 \pm 1.7$	1	$0.7 \pm 0.2 \pm 0.2$
$250 < \Sigma M_T < 300, N_J = 0$	$3.7 \pm 1.0 \pm 2.2$	$0.5 \pm 0.5 \pm 0.1$	$1.1 \pm 0.2 \pm 0.2$	$0.9 \pm 0.4 \pm 0.1$	$6.2 \pm 1.2 \pm 2.2$	5	$1.4 \pm 0.2 \pm 0.2$
$250 < \Sigma M_T < 300, N_J >= 1$	$2.7 \pm 1.1 \pm 0.5$	$1.0 \pm 0.7 \pm 0.1$	$1.0 \pm 0.2 \pm 0.1$	$0.2 \pm 0.1 \pm 0.1$	$4.9 \pm 1.3 \pm 0.5$	7	$0.4 \pm 0.1 \pm 0.1$
$200 < \Sigma M_T < 250, N_J = 0$	$18.2 \pm 2.8 \pm 9.5$	$1.1 \pm 0.8 \pm 0.2$	$0.2 \pm 0.3 \pm 0.1$	$2.0 \pm 0.6 \pm 0.3$	$22.5 \pm 3.0 \pm 9.5$	19	$1.6 \pm 0.2 \pm 0.3$
$200 < \Sigma M_T < 250, N_J >= 1$	$18.1 \pm 2.9 \pm 6$	$3.3 \pm 1.3 \pm 0.7$	$1.3 \pm 0.2 \pm 0.3$	$1.2 \pm 0.4 \pm 0.2$	$23.9 \pm 3.3 \pm 6$	26	$0.4 \pm 0.1 \pm 0.1$
$25 < M_{T2} < 50 \text{ GeV}$							
$300 < \Sigma M_T, N_J = 0$	$2.8 \pm 0.8 \pm 1.8$	< 0.7	$0.2 \pm 0.1 \pm 0.1$	$0.3 \pm 0.2 \pm 0.1$	$3.2 \pm 0.9 \pm 1.8$	3	$1.3 \pm 0.2 \pm 0.4$
$300 < \Sigma M_T, N_J >= 1$	$0.5 \pm 0.5 \pm 0.2$	$1.5 \pm 0.9 \pm 0.5$	$0.6 \pm 0.2 \pm 0.2$	$0.9 \pm 0.4 \pm 0.2$	$3.5 \pm 1.1 \pm 0.6$	3	$0.7 \pm 0.2 \pm 0.2$
$250 < \Sigma M_T < 300, N_J = 0$	$3.1 \pm 1.0 \pm 1.7$	$0.4 \pm 0.4 \pm 0.1$	$0.8 \pm 0.2 \pm 0.1$	$0.7 \pm 0.4 \pm 0.1$	$5.1 \pm 1.2 \pm 1.7$	5	$1.6 \pm 0.2 \pm 0.2$
$250 < \Sigma M_T < 300, N_J >= 1$	$3.6 \pm 1.1 \pm 2.0$	$1.6 \pm 0.9 \pm 0.3$	$1.3 \pm 0.2 \pm 0.2$	$1.2 \pm 0.5 \pm 0.3$	$7.7 \pm 1.5 \pm 2.1$	4	$0.8 \pm 0.2 \pm 0.1$
$200 < \Sigma M_T < 250, N_J = 0$	$23.5 \pm 2.9 \pm 9.8$	$4.3 \pm 2.1 \pm 0.7$	$1.7 \pm 0.3 \pm 0.3$	$2.4 \pm 0.7 \pm 0.4$	$31.9 \pm 3.7 \pm 9.8$	28	$2.4 \pm 0.3 \pm 0.4$
$200 < \Sigma M_T < 250, N_J >= 1$	$12.7 \pm 2.4 \pm 4.2$	$4.5 \pm 1.5 \pm 0.9$	$2.9 \pm 0.4 \pm 0.3$	$0.5 \pm 0.2 \pm 0.1$	$20.6 \pm 2.9 \pm 4.3$	25	$0.6 \pm 0.2 \pm 0.1$

Table 12: Predicted background yields and observed event counts in all $\tau_h \tau_h$ SRs, corresponding to 41.3 fb^{-1} of data collected in 2017. For the background estimates with no events in the sideband or the simulated sample, the 68% statistical upper limit is taken. The uncertainties listed in quadrature are statistical and systematic respectively. We also list the predicted signal yields corresponding to the purely left-handed scenario for a $\tilde{\tau}$ mass of 100 GeV and a $\tilde{\chi}_1^0$ mass of 1 GeV.

Search Region	Misidentified τ_h	DY+jets	Top quark	Other SM	Total Pred.	Obs.	$m(\tilde{\tau}_L) = 100 \text{ GeV}$
	$M_{T2} > 50 \text{ GeV}$						
$300 < \Sigma M_T, N_J = 0$	$0.2 \pm 0.7 \pm 0.5$	< 0.7	$0.4 \pm 0.3 \pm 0.1$	$1.4 \pm 0.7 \pm 0.3$	$2.0 \pm 1.0 \pm 0.6$	3	$1.0 \pm 0.2 \pm 0.2$
$300 < \Sigma M_T, N_J >= 1$	$1.6 \pm 0.8 \pm 0.2$	$0.5 \pm 0.5 \pm 0.1$	$0.6 \pm 0.5 \pm 0.2$	$0.6 \pm 0.4 \pm 0.2$	$3.2 \pm 1.1 \pm 0.4$	3	$0.4 \pm 0.1 \pm 0.1$
$250 < \Sigma M_T < 300, N_J = 0$	$2.8 \pm 1.3 \pm 0.3$	$1.0 \pm 0.6 \pm 0.1$	$0.3 \pm 0.3 \pm 0.1$	$0.9 \pm 0.5 \pm 0.1$	$5.1 \pm 1.5 \pm 0.3$	7	$1.0 \pm 0.2 \pm 0.2$
$250 < \Sigma M_T < 300, N_J >= 1$	$4.5 \pm 1.4 \pm 1.8$	$1.0 \pm 0.6 \pm 0.1$	$0.1 \pm 0.1 \pm 0.0$	$0.7 \pm 0.5 \pm 0.1$	$6.3 \pm 1.6 \pm 1.8$	9	$0.3 \pm 0.1 \pm 0.0$
$200 < \Sigma M_T < 250, N_J = 0$	$11.2 \pm 2.3 \pm 4.7$	$1.3 \pm 0.8 \pm 0.2$	$0.8 \pm 0.4 \pm 0.1$	$1.0 \pm 0.4 \pm 0.2$	$14.3 \pm 2.5 \pm 4.7$	11	$0.9 \pm 0.2 \pm 0.1$
$200 < \Sigma M_T < 250, N_J >= 1$	$9.0 \pm 2.6 \pm 1.1$	$2.6 \pm 1.0 \pm 0.4$	< 0.2	$1.2 \pm 0.6 \pm 0.2$	$12.8 \pm 2.8 \pm 1.2$	24	$0.2 \pm 0.1 \pm 0.0$
$25 < M_{T2} < 50 \text{ GeV}$							
$300 < \Sigma M_T, N_J = 0$	$0.5 \pm 0.5 \pm 0.1$	$1.1 \pm 0.8 \pm 0.3$	$0.3 \pm 0.3 \pm 0.1$	$0.5 \pm 0.3 \pm 0.1$	$2.4 \pm 1.0 \pm 0.4$	1	$1.4 \pm 0.2 \pm 0.4$
$300 < \Sigma M_T, N_J >= 1$	$1.9 \pm 0.8 \pm 1.3$	$1.0 \pm 0.8 \pm 0.1$	$0.5 \pm 0.2 \pm 0.1$	$0.6 \pm 0.4 \pm 0.3$	$4.0 \pm 1.2 \pm 1.4$	2	$0.6 \pm 0.1 \pm 0.2$
$250 < \Sigma M_T < 300, N_J = 0$	$2.7 \pm 0.9 \pm 1.0$	$1.9 \pm 1.4 \pm 0.5$	$0.2 \pm 0.1 \pm 0.1$	$0.7 \pm 0.5 \pm 0.1$	$5.4 \pm 1.8 \pm 1.1$	6	$1.3 \pm 0.2 \pm 0.2$
$250 < \Sigma M_T < 300, N_J >= 1$	$1.1 \pm 0.8 \pm 0.3$	$0.6 \pm 0.4 \pm 0.2$	$1.0 \pm 0.6 \pm 0.1$	$0.5 \pm 0.5 \pm 0.1$	$3.2 \pm 1.2 \pm 0.4$	5	$0.3 \pm 0.1 \pm 0.0$
$200 < \Sigma M_T < 250, N_J = 0$	$18.6 \pm 3.1 \pm 3.6$	$5.0 \pm 2.0 \pm 0.7$	$1.2 \pm 0.6 \pm 0.2$	$1.9 \pm 0.7 \pm 0.4$	$26.7 \pm 3.8 \pm 3.7$	40	$1.7 \pm 0.2 \pm 0.2$
$200 < \Sigma M_T < 250, N_J >= 1$	$9.4 \pm 2.1 \pm 1.7$	$1.5 \pm 0.7 \pm 0.2$	$1.1 \pm 0.5 \pm 0.2$	$1.4 \pm 0.6 \pm 0.4$	$13.3 \pm 2.3 \pm 1.8$	12	$0.4 \pm 0.1 \pm 0.1$

Table 13: Predicted signal yields, \pm stat \pm syst, in all SRs for $M(\tilde{\tau}_L)$ in [100,150,200] GeV and $M(\tilde{\chi}_1^0) = 0$ GeV for the 36 fb^{-1} of data collected in 2016.

Search Region	$M(\tilde{\tau}_L)=100$ GeV	$M(\tilde{\tau}_L)=150$ GeV	$M(\tilde{\tau}_L)=200$ GeV
High M_{T2} SR			
$300 < \Sigma M_T, N_J = 0$	$1.7 \pm 0.2 \pm 0.4$	$3.1 \pm 0.2 \pm 0.7$	$2.6 \pm 0.1 \pm 0.7$
$300 < \Sigma M_T, N_J \geq 1$	$0.7 \pm 0.2 \pm 0.2$	$1.5 \pm 0.1 \pm 0.3$	$1.4 \pm 0.1 \pm 0.4$
$250 < \Sigma M_T < 300, N_J = 0$	$1.4 \pm 0.2 \pm 0.2$	$1.1 \pm 0.1 \pm 0.1$	$0.6 \pm 0.0 \pm 0.1$
$250 < \Sigma M_T < 300, N_J \geq 1$	$0.4 \pm 0.1 \pm 0.1$	$0.5 \pm 0.1 \pm 0.1$	$0.2 \pm 0.0 \pm 0.0$
$200 < \Sigma M_T < 250, N_J = 0$	$1.6 \pm 0.2 \pm 0.3$	$0.9 \pm 0.1 \pm 0.1$	$0.3 \pm 0.0 \pm 0.0$
$200 < \Sigma M_T < 250, N_J \geq 1$	$0.4 \pm 0.1 \pm 0.1$	$0.3 \pm 0.0 \pm 0.0$	$0.1 \pm 0.0 \pm 0.0$
Low M_{T2} SR			
$300 < \Sigma M_T, N_J = 0$	$1.3 \pm 0.2 \pm 0.4$	$0.9 \pm 0.1 \pm 0.3$	$0.5 \pm 0.0 \pm 0.2$
$300 < \Sigma M_T, N_J \geq 1$	$0.7 \pm 0.2 \pm 0.2$	$0.4 \pm 0.1 \pm 0.1$	$0.3 \pm 0.0 \pm 0.1$
$250 < \Sigma M_T < 300, N_J = 0$	$1.6 \pm 0.2 \pm 0.2$	$0.6 \pm 0.1 \pm 0.1$	$0.3 \pm 0.0 \pm 0.1$
$250 < \Sigma M_T < 300, N_J \geq 1$	$0.8 \pm 0.2 \pm 0.1$	$0.2 \pm 0.0 \pm 0.0$	$0.1 \pm 0.0 \pm 0.0$
$200 < \Sigma M_T < 250, N_J = 0$	$2.4 \pm 0.3 \pm 0.4$	$0.8 \pm 0.1 \pm 0.1$	$0.3 \pm 0.0 \pm 0.0$
$200 < \Sigma M_T < 250, N_J \geq 1$	$0.6 \pm 0.2 \pm 0.1$	$0.4 \pm 0.1 \pm 0.1$	$0.2 \pm 0.0 \pm 0.0$

Table 14: Predicted signal yields, \pm stat \pm syst, in all SRs for $M(\tilde{\tau}_L)$ in [100,150,200] GeV and $M(\tilde{\chi}_1^0) = 0$ GeV for the 41.5 fb^{-1} of data collected in 2017.

Search Region	$M(\tilde{\tau}_L)=100$ GeV	$M(\tilde{\tau}_L)=150$ GeV	$M(\tilde{\tau}_L)=200$ GeV
High M_{T2} SR			
$300 < \Sigma M_T, N_J = 0$	$1.0 \pm 0.2 \pm 0.2$	$2.6 \pm 0.1 \pm 0.6$	$2.2 \pm 0.1 \pm 0.5$
$300 < \Sigma M_T, N_J \geq 1$	$0.4 \pm 0.1 \pm 0.1$	$0.9 \pm 0.1 \pm 0.2$	$1.0 \pm 0.1 \pm 0.2$
$250 < \Sigma M_T < 300, N_J = 0$	$1.0 \pm 0.2 \pm 0.2$	$0.8 \pm 0.1 \pm 0.1$	$0.3 \pm 0.0 \pm 0.0$
$250 < \Sigma M_T < 300, N_J \geq 1$	$0.3 \pm 0.1 \pm 0.0$	$0.2 \pm 0.0 \pm 0.0$	$0.1 \pm 0.0 \pm 0.0$
$200 < \Sigma M_T < 250, N_J = 0$	$0.9 \pm 0.2 \pm 0.1$	$0.5 \pm 0.1 \pm 0.1$	$0.1 \pm 0.0 \pm 0.0$
$200 < \Sigma M_T < 250, N_J \geq 1$	$0.2 \pm 0.1 \pm 0.0$	$0.1 \pm 0.0 \pm 0.0$	$0.1 \pm 0.0 \pm 0.0$
Low M_{T2} SR			
$300 < \Sigma M_T, N_J = 0$	$1.4 \pm 0.2 \pm 0.4$	$0.8 \pm 0.1 \pm 0.3$	$0.5 \pm 0.0 \pm 0.1$
$300 < \Sigma M_T, N_J \geq 1$	$0.6 \pm 0.1 \pm 0.2$	$0.4 \pm 0.1 \pm 0.1$	$0.3 \pm 0.0 \pm 0.1$
$250 < \Sigma M_T < 300, N_J = 0$	$1.3 \pm 0.2 \pm 0.2$	$0.4 \pm 0.1 \pm 0.1$	$0.3 \pm 0.0 \pm 0.0$
$250 < \Sigma M_T < 300, N_J \geq 1$	$0.3 \pm 0.1 \pm 0.0$	$0.2 \pm 0.0 \pm 0.0$	$0.1 \pm 0.0 \pm 0.0$
$200 < \Sigma M_T < 250, N_J = 0$	$1.7 \pm 0.2 \pm 0.2$	$0.7 \pm 0.1 \pm 0.1$	$0.3 \pm 0.0 \pm 0.0$
$200 < \Sigma M_T < 250, N_J \geq 1$	$0.4 \pm 0.1 \pm 0.1$	$0.3 \pm 0.0 \pm 0.0$	$0.1 \pm 0.0 \pm 0.0$

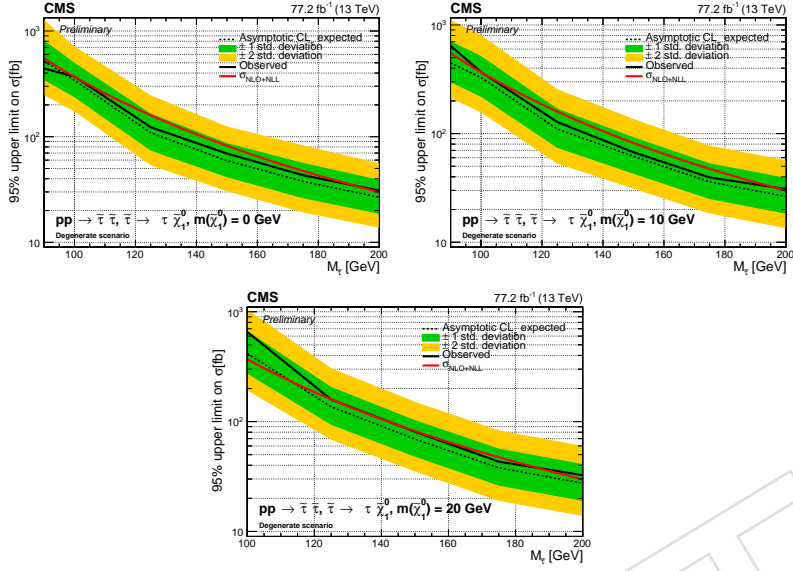


Figure 15: Expected and observed combined limits for 2016+2017 as a function of $\tilde{\tau}$ mass in the degenerate $\tilde{\tau}$ scenario for $\tilde{\chi}_1^0$ masses of 1 (left), 10 (middle), and 20 (right) GeV.

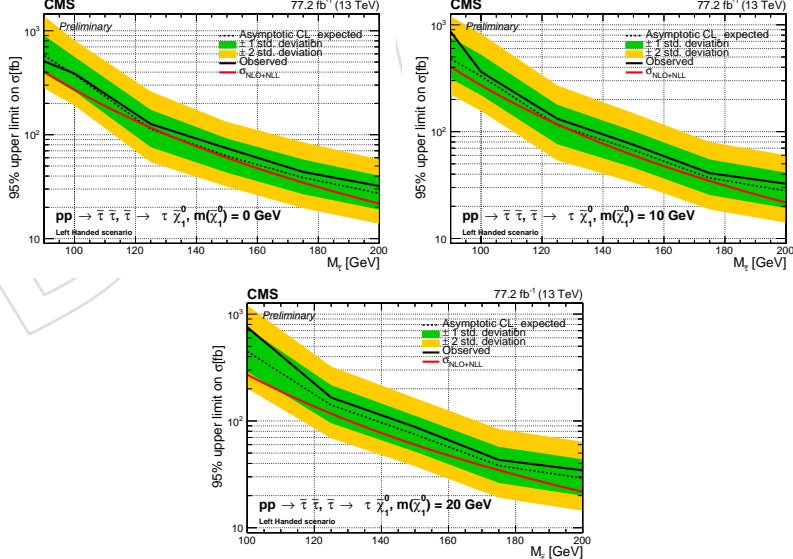


Figure 16: Expected and observed combined limits for 2016+2017 as a function of $\tilde{\tau}$ mass in the left-handed $\tilde{\tau}$ scenario for $\tilde{\chi}_1^0$ masses of 1 (left), and 10 (right) GeV.

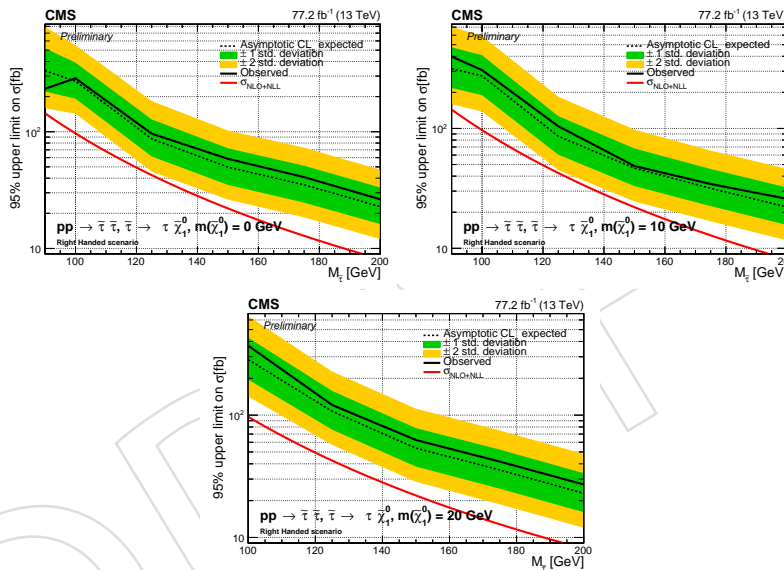


Figure 17: Expected and observed combined limits for 2016+2017 as a function of $\tilde{\tau}$ mass in the right-handed $\tilde{\tau}$ scenario for $\tilde{\chi}_1^0$ masses of 1 (left), and 10 (right) GeV.

462 References

- 463 [1] G. 't Hooft, "Naturalness, chiral symmetry, and spontaneous chiral symmetry breaking",
464 *NATO Sci. Ser. B* **59** (1980) 135.
- 465 [2] E. Witten, "Dynamical breaking of supersymmetry", *Nucl. Phys. B* **188** (1981) 513,
466 doi:10.1016/0550-3213(81)90006-7.
- 467 [3] M. Dine, W. Fischler, and M. Srednicki, "Supersymmetric technicolor", *Nucl. Phys. B* **189**
468 (1981) 575, doi:10.1016/0550-3213(81)90582-4.
- 469 [4] S. Dimopoulos and S. Raby, "Supercolor", *Nucl. Phys. B* **192** (1981) 353,
470 doi:10.1016/0550-3213(81)90430-2.
- 471 [5] S. Dimopoulos and H. Georgi, "Softly broken supersymmetry and SU(5)", *Nucl. Phys. B*
472 **193** (1981) 150, doi:10.1016/0550-3213(81)90522-8.
- 473 [6] R. K. Kaul and P. Majumdar, "Cancellation of quadratically divergent mass corrections in
474 globally supersymmetric spontaneously broken gauge theories", *Nucl. Phys. B* **199**
475 (1982) 36, doi:10.1016/0550-3213(82)90565-X.
- 476 [7] J. Wess and B. Zumino, "Supergauge transformations in four-dimensions", *Nucl. Phys. B*
477 **70** (1974) 39, doi:10.1016/0550-3213(74)90355-1.
- 478 [8] G. R. Farrar and P. Fayet, "Phenomenology of the Production, Decay, and Detection of
479 New Hadronic States Associated with Supersymmetry", *Phys. Lett. B* **76** (1978) 575,
480 doi:10.1016/0370-2693(78)90858-4.
- 481 [9] C. Boehm, A. Djouadi, and M. Drees, "Light scalar top quarks and supersymmetric dark
482 matter", *Phys. Rev. D* **62** (2000) 035012, doi:10.1103/PhysRevD.62.035012,
483 arXiv:hep-ph/9911496.
- 484 [10] C. Balázs, M. Carena, and C. E. M. Wagner, "Dark matter, light stops and electroweak
485 baryogenesis", *Phys. Rev. D* **70** (2004) 015007, doi:10.1103/PhysRevD.70.015007,
486 arXiv:hep-ph/403224.
- 487 [11] G. Jungman, M. Kamionkowski, and K. Griest, "Supersymmetric dark matter", *Phys.
488 Rept.* **267** (1996) 195, doi:10.1016/0370-1573(95)00058-5,
489 arXiv:hep-ph/9506380.
- 490 [12] CMS Collaboration, "Search for supersymmetry in proton-proton collisions at 13 tev
491 using identified top quarks", *Phys. Lett. D* **97** (2018)
492 doi:10.1103/PhysRevD.97.012007, arXiv:1710.11188.
- 493 [13] ATLAS Collaboration, "Search for supersymmetry in final states with missing transverse
494 momentum and multiple b-jets in proton–proton collisions at $\sqrt{s}=13$ tev with the atlas
495 detector",.
- 496 [14] LEP SUSY Working Group (ALEPH, DELPHI, L3, OPAL) (2004). Notes
497 LEPSUSYWG/04-01.1.
- 498 [15] ATLAS Collaboration, "Search for the direct production of charginos, neutralinos and
499 staus in final states with at least two hadronically decaying taus and missing transverse
500 momentum in pp collisions at $\sqrt{s} = 8$ TeV with the ATLAS detector", *JHEP* **10** (2014) 96,
501 doi:10.1007/JHEP10(2014)096, arXiv:1407.0350.

- 502 [16] ATLAS Collaboration, “Search for the electroweak production of supersymmetric
503 particles in $\sqrt{s} = 8$ TeV pp collisions with the ATLAS detector”, *Phys. Rev. D* **93** (2016)
504 052002, doi:10.1103/PhysRevD.93.052002, arXiv:1509.07152.
- 505 [17] CMS Collaboration, “Search for electroweak production of charginos in final states with
506 two tau leptons in pp collisions at $\sqrt{s} = 8$ TeV”, *JHEP* **04** (2017) 018,
507 doi:10.1007/JHEP04(2017)018, arXiv:1610.04870.
- 508 [18] CMS Collaboration Collaboration, “Search for pair production of tau sleptons in
509 $\sqrt{s} = 13$ TeV pp collisions in the all-hadronic final state”, Technical Report
510 CMS-PAS-SUS-17-003, CERN, Geneva, 2017.
- 511 [19] CMS Collaboration Collaboration, “Search for supersymmetry in events with tau leptons
512 and missing transverse momentum in proton-proton collisions at $\sqrt{s}=13$ TeV”,
513 Technical Report CMS-PAS-SUS-17-002, CERN, Geneva, 2017.
- 514 [20] B. Fuks, M. Klasen, D. R. Lamprea, and M. Rothering, “Revisiting slepton pair
515 production at the Large Hadron Collider”, *JHEP* **01** (2014) 168,
516 doi:10.1007/JHEP01(2014)168, arXiv:1310.2621.
- 517 [21] M. Cepeda et al., “Search for stau production in the all-hadronic final state”, CMS Analysis
518 Note 2016/436, 2016.
- 519 [22] M. Cacciari, G. P. Salam, and G. Soyez, “The anti- k_T jet clustering algorithm”, *JHEP* **04**
520 (2008) 063, doi:10.1088/1126-6708/2008/04/063, arXiv:0802.1189.
- 521 [23] M. Cacciari, G. P. Salam, and G. Soyez, “FastJet user manual”, *Eur. Phys. J. C* **72** (2012)
522 1896, doi:10.1140/epjc/s10052-012-1896-2, arXiv:1111.6097.
- 523 [24] CMS Collaboration, “Performance of tau-lepton reconstruction and identification in
524 CMS”, *JINST* **7** (2012) P01001, doi:10.1088/1748-0221/7/01/P01001,
525 arXiv:1109.6034.
- 526 [25] CMS Collaboration, “Reconstruction and identification of τ lepton decays to hadrons and
527 ν_τ at CMS”, *JINST* **11** (2016) P01019, doi:10.1088/1748-0221/11/01/P01019,
528 arXiv:1510.07488.
- 529 [26] CMS Collaboration, “Performance of reconstruction and identification of tau leptons in
530 their decays to hadrons and tau neutrino in LHC Run-2”, CMS Physics Analysis
531 Summary CMS-PAS-TAU-16-002, 2016.
- 532 [27] “Tau Id for 13 TeV run”.
533 <https://twiki.cern.ch/twiki/bin/view/CMS/TauIDRecommendation13TeV>.
- 534 [28] “Muon identification for Run II”. https://twiki.cern.ch/twiki/bin/view/CMS/SWGuideMuonIdRun2#Medium_Muon.
- 536 [29] “Cut-based electron identification for Run II”.
537 https://twiki.cern.ch/twiki/bin/view/CMS/CutBasedElectronIdentificationRun2#Spring15_selection_25ns.
- 539 [30] C. G. Lester and D. J. Summers, “Measuring masses of semiinvisibly decaying particles
540 pair produced at hadron colliders”, *Phys. Lett. B* **463** (1999) 99,
541 doi:10.1016/S0370-2693(99)00945-4, arXiv:hep-ph/9906349.

- 542 [31] A. Barr, C. Lester, and P. Stephens, “m(T2): The truth behind the glamour”, *J. Phys. G* **29**
543 (2003) 2343, doi:10.1088/0954-3899/29/10/304, arXiv:hep-ph/0304226.
- 544 [32] H. Bakhshian et al., “Computing the contamination from fakes in leptonic final states”,
545 CMS Analysis Note 2010/261, 2010.
- 546 [33] CMS Collaboration, “Interpretation of searches for supersymmetry with simplified
547 models”, *Phys. Rev. D* **88** (2013) 052017, doi:10.1103/PhysRevD.88.052017,
548 arXiv:1301.2175.
- 549 [34] J. Alwall, P. Schuster, and N. Toro, “Simplified models for a first characterization of new
550 physics at the lhc”, *Phys. Rev. D* **79** (2009) 075020,
551 doi:10.1103/PhysRevD.79.075020.
- 552 [35] J. Alwall, M.-P. Le, M. Lisanti, and J. Wacker, “Model-independent jets plus missing
553 energy searches”, *Phys. Rev. D* **79** (2009) 015005,
554 doi:10.1103/PhysRevD.79.015005.
- 555 [36] LHC New Physics Working Group, D. Alves et al., “Simplified models for LHC new
556 physics searches”, *J. Phys. G* **39** (2012) 105005,
557 doi:10.1088/0954-3899/39/10/105005, arXiv:1105.2838.
- 558 [37] T. Junk, “Confidence level computation for combining searches with small statistics”,
559 *Nucl. Instrum. Meth. A* **434** (1999) 435, doi:10.1016/S0168-9002(99)00498-2,
560 arXiv:hep-ex/9902006.
- 561 [38] A. L. Read, “Presentation of search results: the CL_S technique”, *J. Phys. G* **28** (2002) 2693,
562 doi:10.1088/0954-3899/28/10/313.
- 563 [39] ATLAS and CMS Collaborations, LHC Higgs Combination Group, “Procedure for the
564 LHC Higgs boson search combination in Summer 2011”, Technical Report
565 ATL-PHYS-PUB 2011-11, CMS NOTE 2011/005, 2011.
- 566 [40] G. Cowan, K. Cranmer, E. Gross, and O. Vitells, “Asymptotic formulae for
567 likelihood-based tests of new physics”, *Eur. Phys. J. C* **71** (2011) 1554,
568 doi:10.1140/epjc/s10052-011-1554-0, arXiv:1007.1727. [Erratum:
569 doi:10.1140/epjc/s10052-013-2501-z].

570 A DeepPF Isolation

571 The DeepPF isolation takes the raw, pre-processed particle-flow inputs listed in Table 15, and
 572 feeds them into a deep convolutional neural network. The final output is averaged with the
 573 high-level 2016 Tau POG MVA (ByIsolationMVA3oldDMwoLTraw) to ensure a strong corre-
 574 lation and to combat some mismodeling. Selected candidates must be within $\Delta R < .5$ of the
 575 reconstructed tau candidate Variables that are only recorded for charged candidates are im-
 576 puted with the listed values below for neutral candidates.

577 The selected PF Candidates are sorted according to particle p_T in ascending order. Up to 60
 578 particles are fed in per a given tau candidate. The dimensionality of the table is 60 by 48, after
 579 accounting for the one-hot-encoding of the variable categorical variables listed below. Charged
 580 candidates that are not associated with a primary vertex or candidates with $p_T < .5$ GeV are
 581 not included.

582 The deep neural net is trained on Keras with over 100 million simulated tau candidates. The
 583 network is a 12 layer deep convolutional neural network that flattens out into a deep connected
 584 neural network. The ADAM algorithm with a small learning rate is used to fit the weights. In
 585 order to prevent biasing from the training sample kinematics the signal and background tau
 586 candidates p_T spectrum is re-weighted to match that of a flat distribution.

587 For tau candidates with less than 60 PF Candidates null-vectors are appended to the top of the
 588 tabulated list.

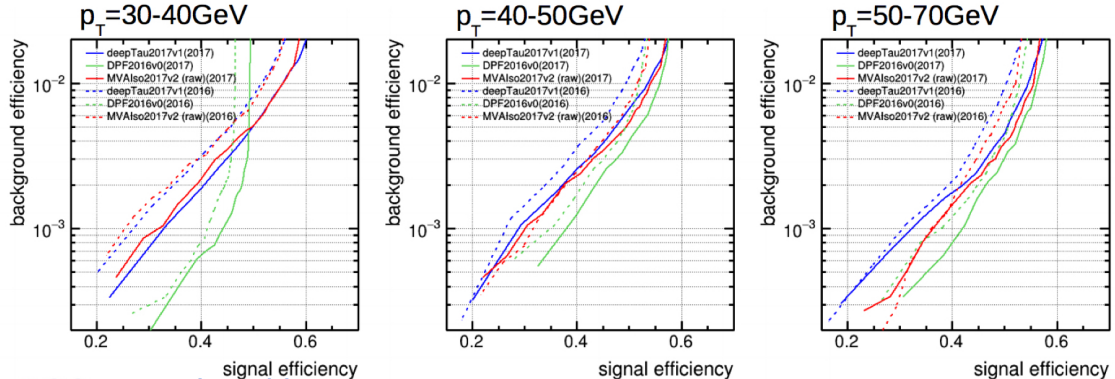


Figure 18: ROC Curves as measured by the Tau POG for objects used in this analysis. Dotted curves show the response in 2016 MC, whereas solid curves are the 2017 MC.

Table 15: Input variables for DeepPF algorithm

PFCand Variable	Pre-Processing (charged pf)	Imputed Value (neutral)	Figure
$p_T(\text{cand})$	$\max(1, \text{var}/500)$	-	26
$p_z(\text{cand})$	$\max(1, \text{var}/1000)$	-	28
$p_T(\text{cand})/p_T(\tau)$	$\max(1, \text{var})$	-	27
$p_z(\text{cand})/p_z(\tau)$	$\max(1, \text{var}/100)$	-	29
$\eta(\text{cand})$	$\text{var}/.5$	-	30
$\Delta R(\text{cand}, \tau)$	$\text{var}/.5$	-	33
$\Delta\phi(\text{cand}, \tau)$	$\text{var}/.5$	-	32
$\Delta\eta(\text{cand}, \tau)$	$\text{var}/.5$	-	31
$d_z(\text{cand})$	$\max(1, \text{var} /5) * \text{sign}(\text{var})$	(-1 or 1, by pseud-random number)	37
$\sigma(d_z)(\text{cand})$	$\max(1, \text{var})$	1	36
$d_0(\text{cand})$	$\max(1, \text{var} /5) * \text{sign}(\text{var})$	(-1 or 1, by pseud-random number)	38
$\sigma(d_0)(\text{cand})$	$\max(1, \text{var})$	1	39
$d_z/\sigma(d_z)(\text{cand})$	$\max(1, \text{var} /3) * \text{sign}(\text{var})$	(-1 or 1, by pseud-random number)	34
$d_0/\sigma(d_0)(\text{cand})$	$\max(1, \text{var} /3) * \text{sign}(\text{var})$	(-1 or 1, by pseud-random number)	34
$d_0 d_0(\text{cand})$	Pre-processed d_0^2	1	-
$d_0 d_z(\text{cand})$	Pre-processed $d_0 d_z$	(-1 or 1, by pseud-random number)	40
$d_0(\text{cand})\Delta\phi(\text{cand}, \tau)$	Pre-processed $d_0 \Delta\phi$	(-1 or 1, by pseud-random number)	41
Charge	One-Hot-Encoded	-	-
PdgId	One-Hot-Encoded	-	-
$(p_T(\text{cand})/p_T(\tau))^2$	Pre-Proccsed Var Squared	-	-
NPixHits	$\text{var}/30.$	0	44
NHits	$\text{var}/7.$	0	45
Lost Inner Hits	One-Hot-Encoded	-	43
pfCandPuppiWeight	-	-	42
Vertex Quality	One-Hot-Encoded	-	50
From PV	One-Hot-Encoded	-	46
In Barrel? ($ \eta < 1.4$)	-	-	48
High Purity track?	-	-	47
HPS Signal Candidate?	-	-	49

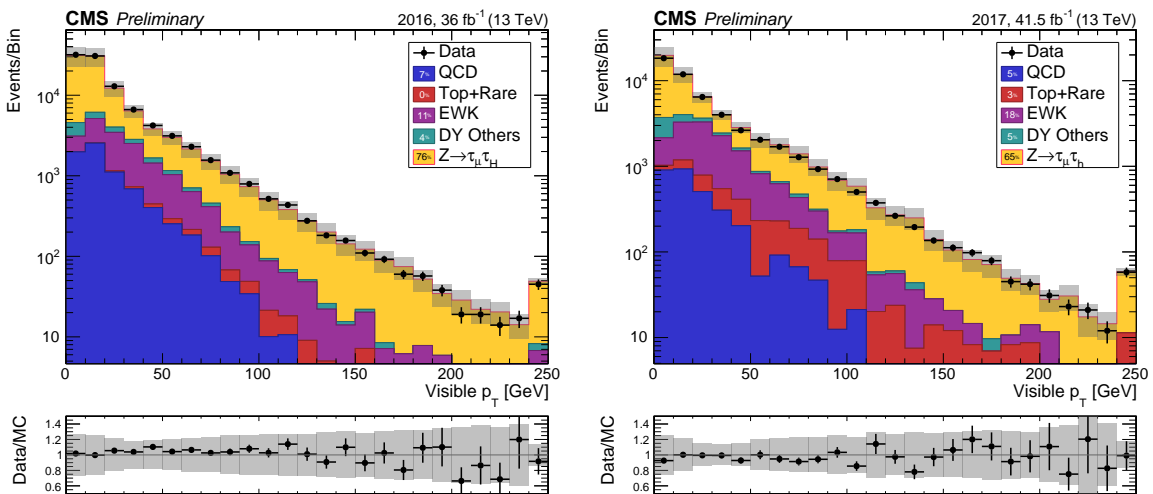
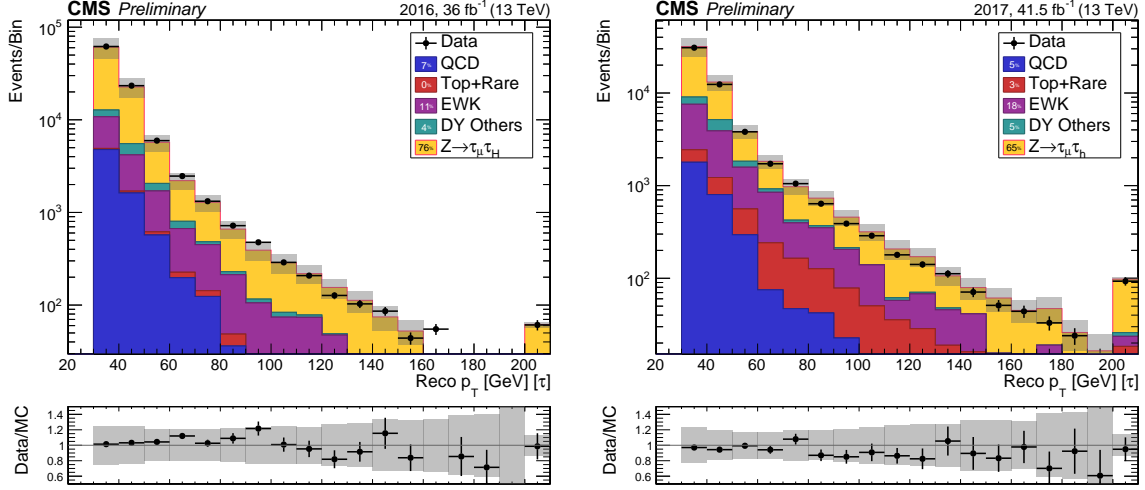
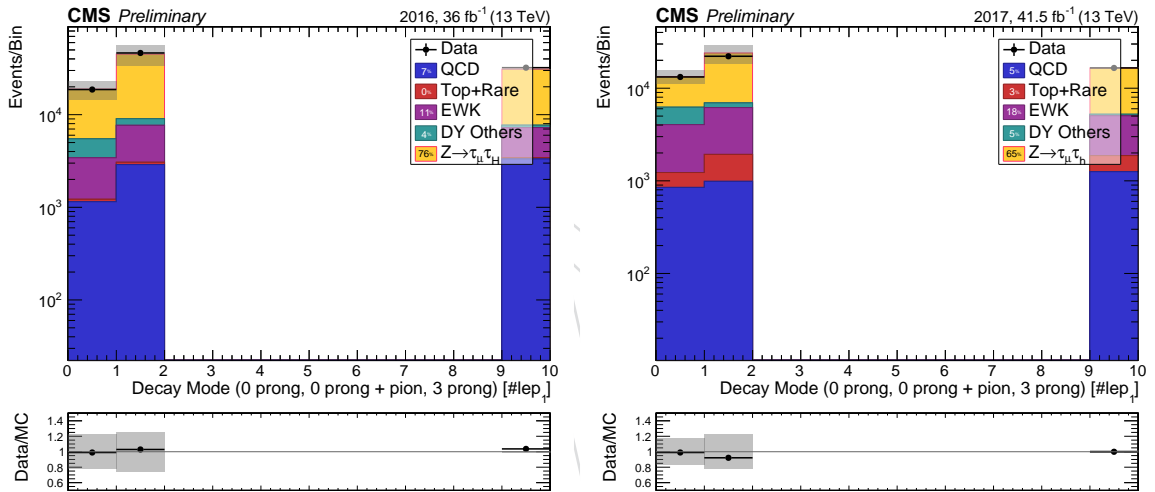
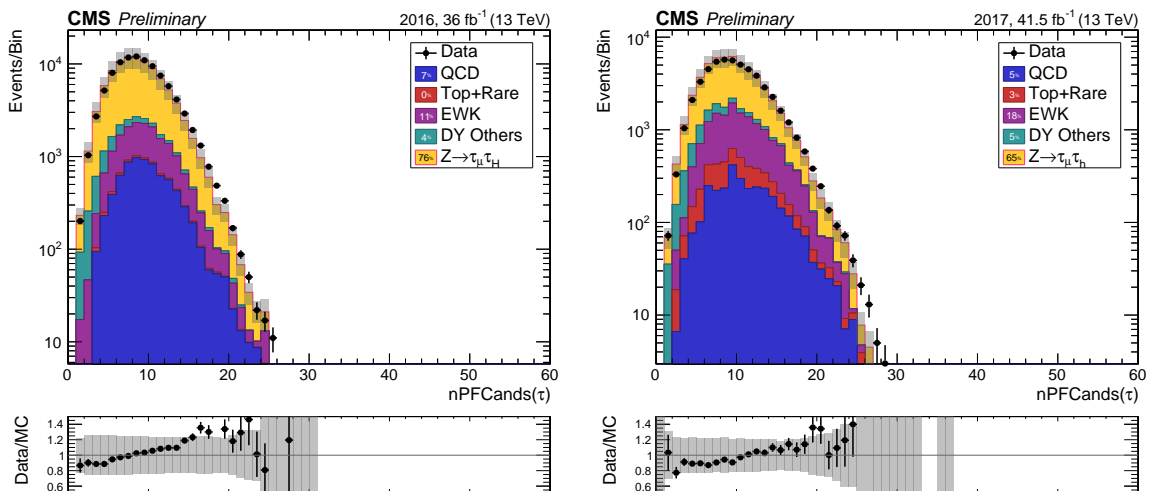
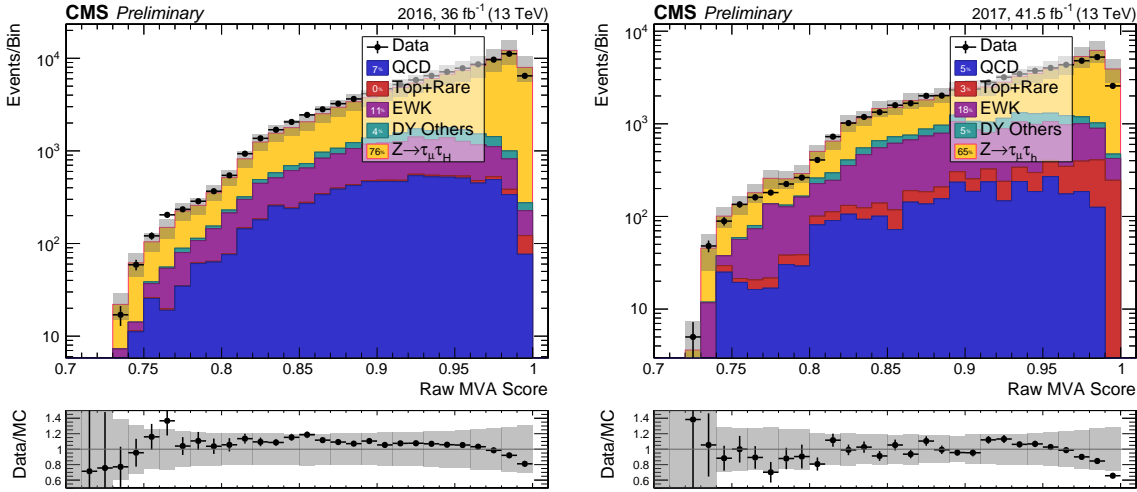
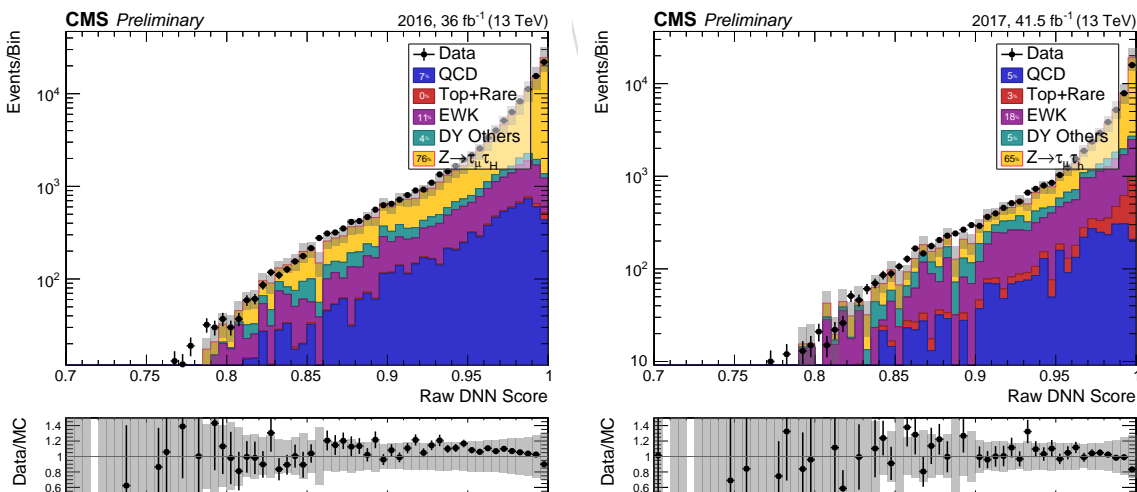


Figure 19: Extended validation of the DeepPF isolation in the mu-tau channel (2016 top, 2017 bottom). A scale factor of .93 has been applied in 2016 and .95 in 2017. From the above, and additional checks of the DY mass and p_T modelling in the mu-tau channel we draw evidence that there is no significant SF dependency on tau p_T or decay mode.

Figure 20: Probe τ reconstructed p_T Figure 21: Probe τ decay modeFigure 22: Probe τ number of particle flow candidates

Figure 23: Probe τ MVA isolationFigure 24: Probe τ DNN Isolation, this raw value is averaged with the MVA score above to form DeepPF isolation

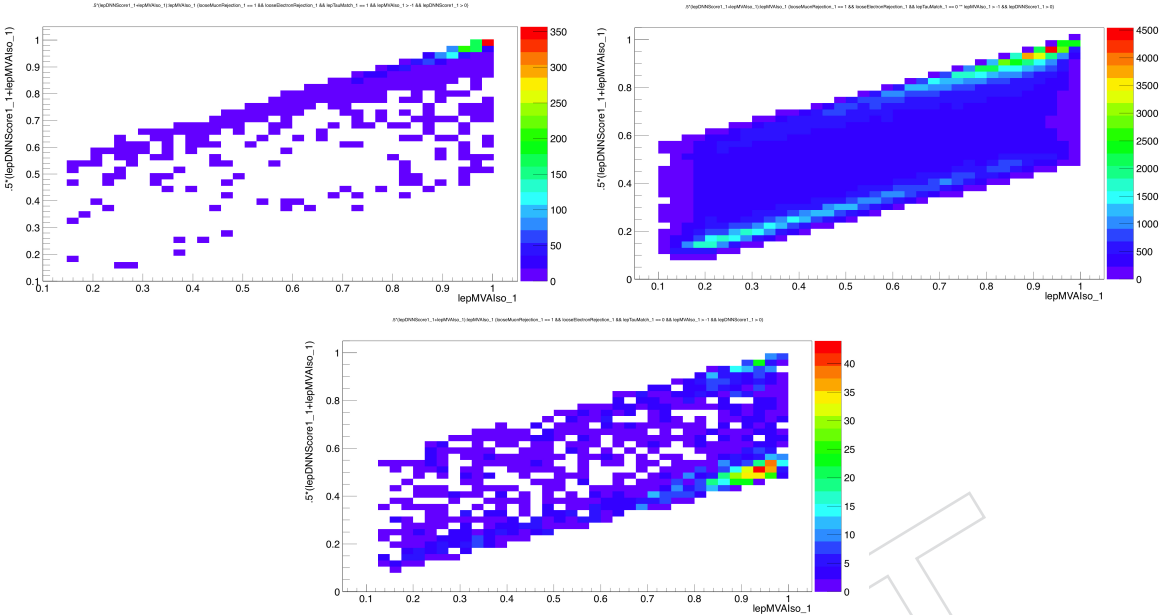


Figure 25: Correlation of MVA isolation to DeepPF Isolation for taus candidates in the single muon channel. Results are shown for genuine taus, jet to fake, and muon to fake taus (left to right). In general a very high correlation between the two scores is seen for genuine taus, whereas fake tau candidates score higher values from the nominal MVA than from DeepPF. One can see from the bottom plot that the muon to tau fake rate is greatly reduced by applying the DeepPF isolation.

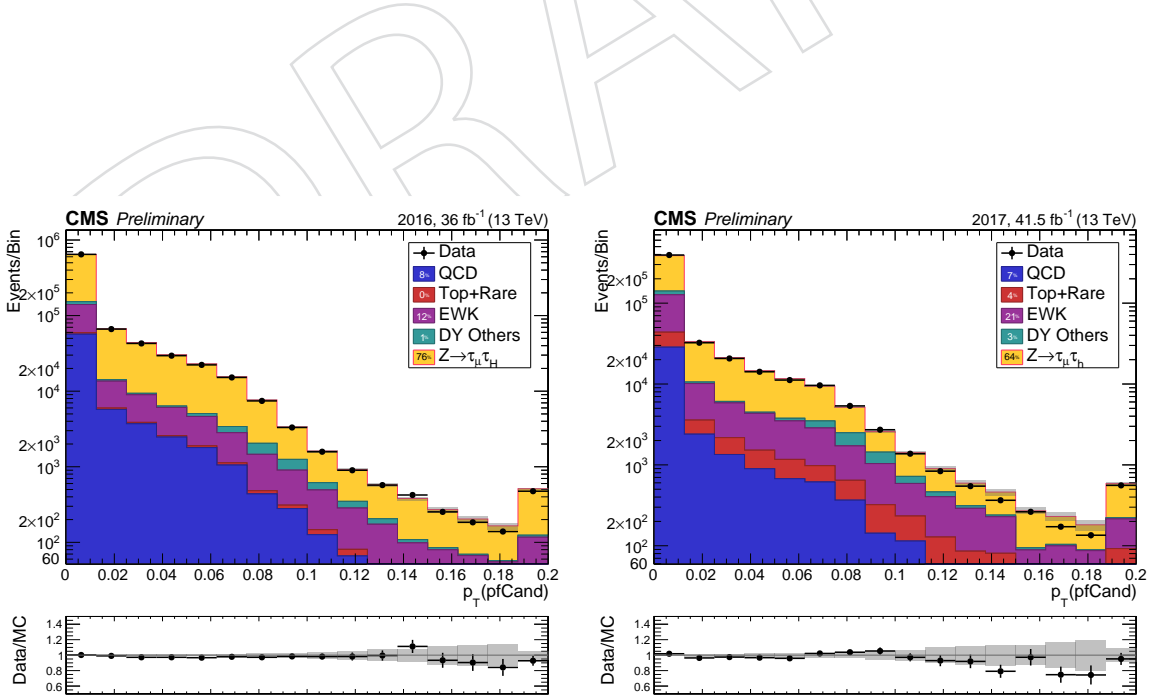
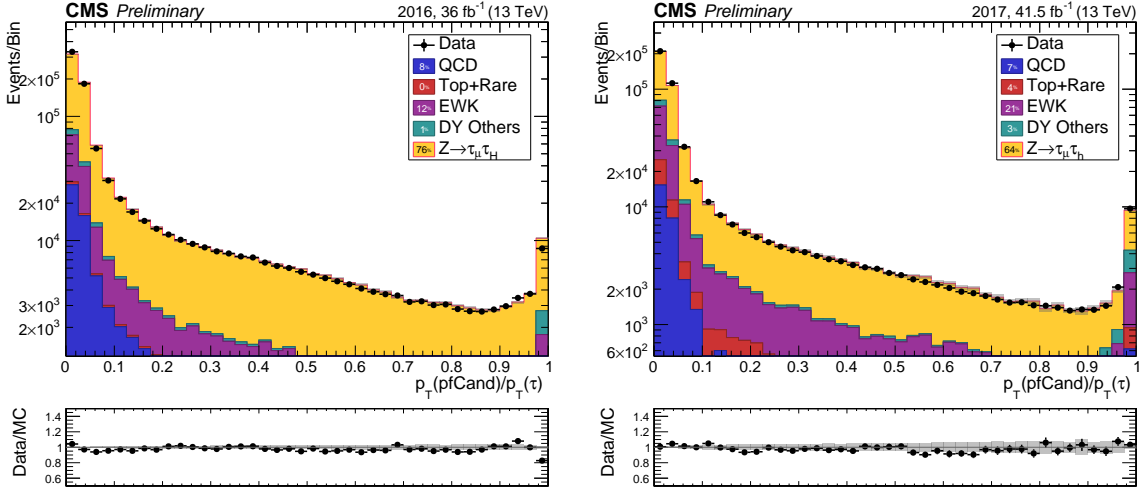
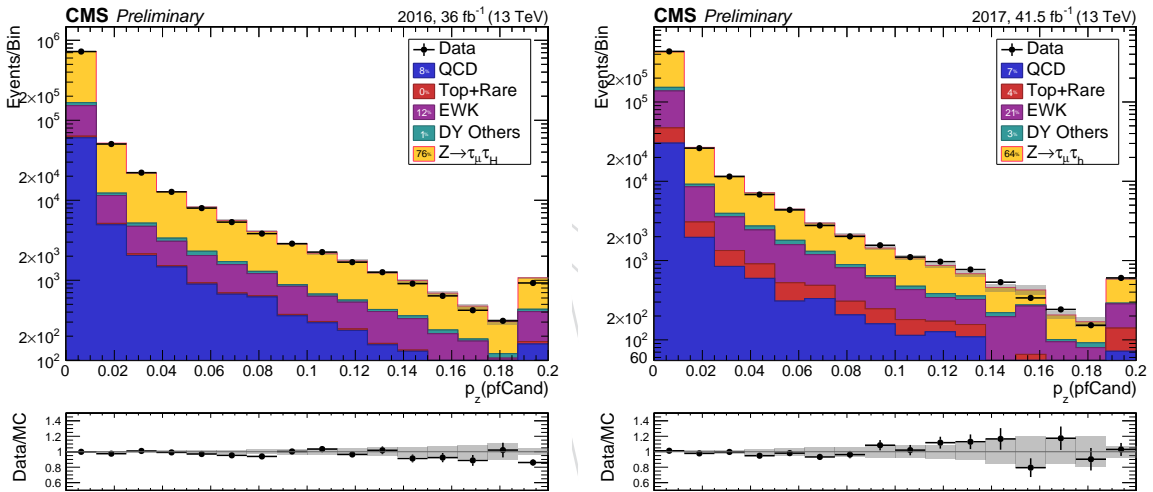
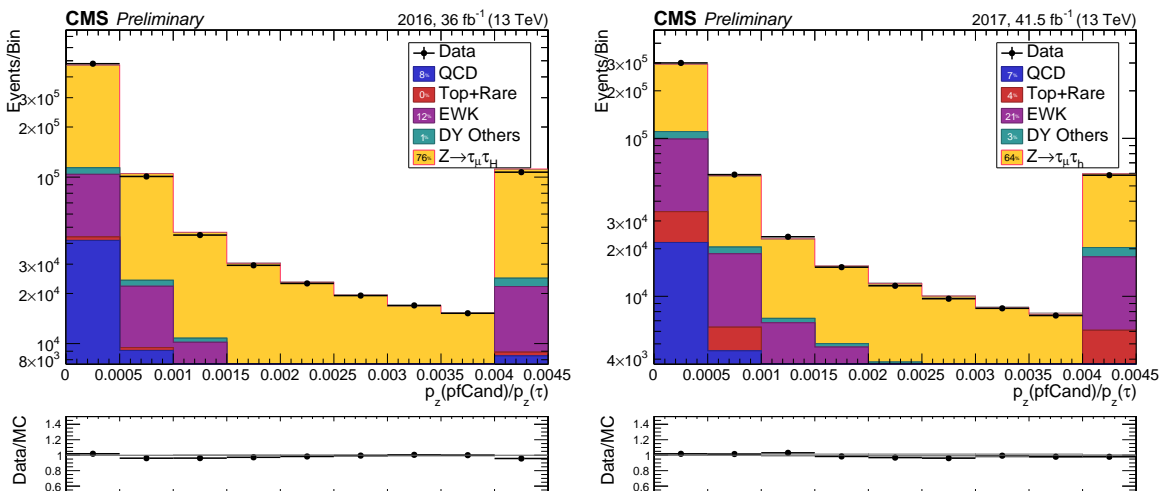
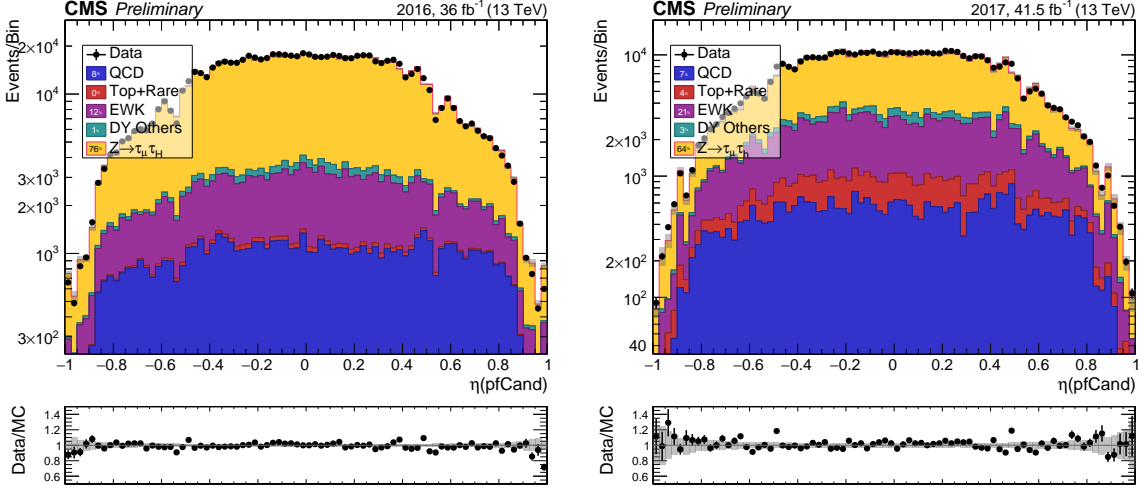
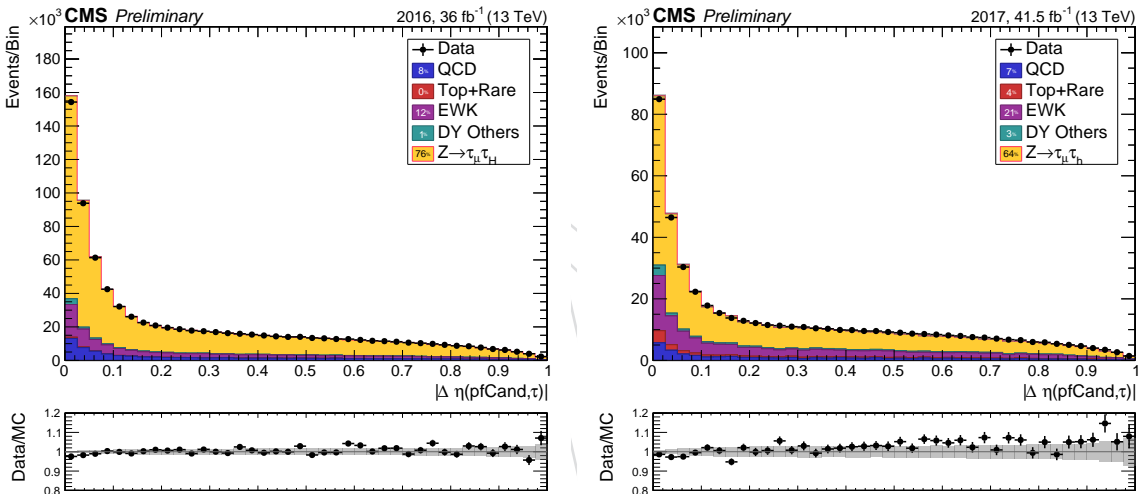
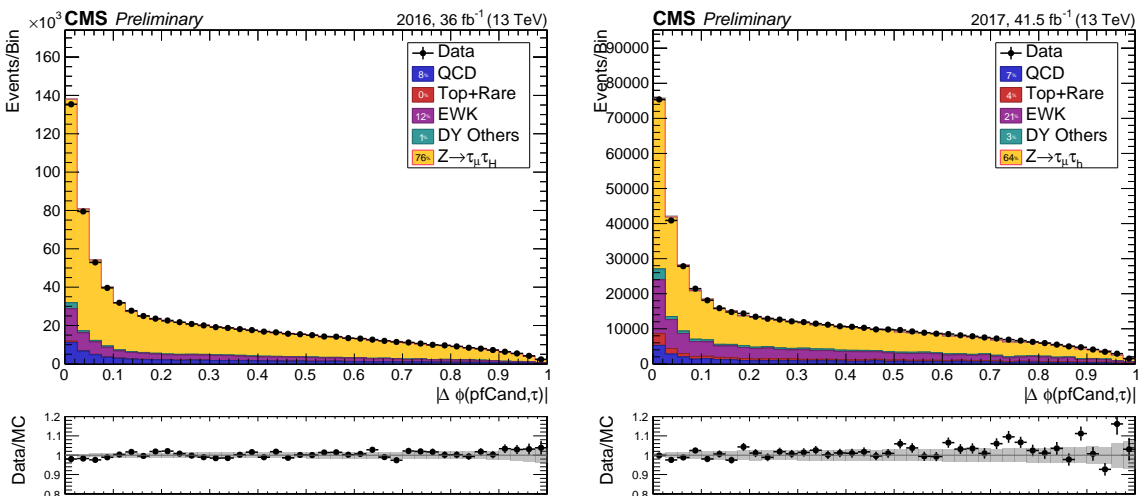
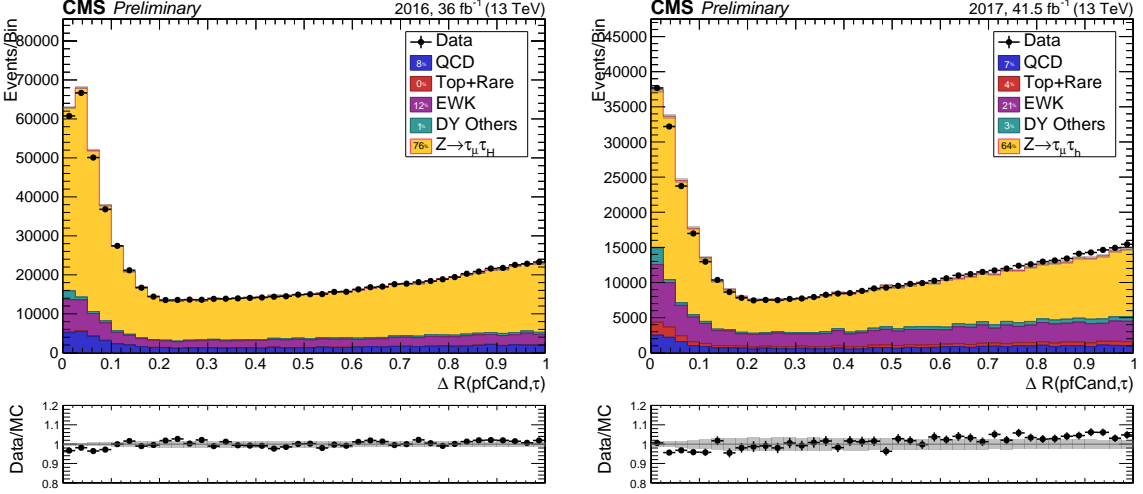
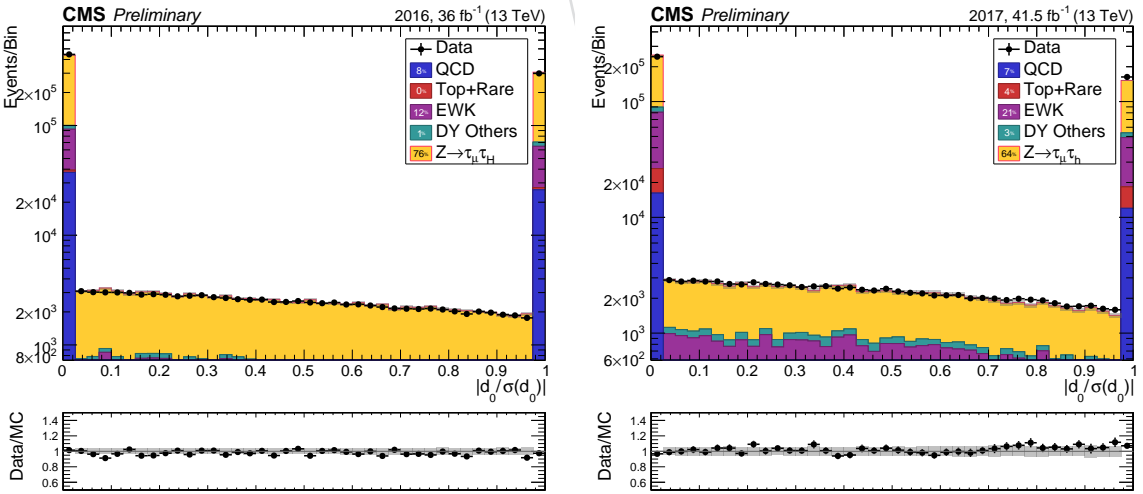


Figure 26: p_T of PF Candidates associated to the probe τ

Figure 27: Relative p_T of PF Candidates associated to the probe τ Figure 28: p_z of PF Candidates associated to the probe τ Figure 29: Relative p_z of PF Candidates associated to the probe τ

Figure 30: Reconstructed $|\eta|$ of PF Candidates associated to the probe τ Figure 31: $\Delta \eta$ between the probe τ and associated particle flow candidatesFigure 32: $\Delta \phi$ between the probe τ and associated particle flow candidates

Figure 33: ΔR between the probe τ and associated particle flow candidatesFigure 34: Significance of d_0 for the particle flow candidates associated to the probe τ

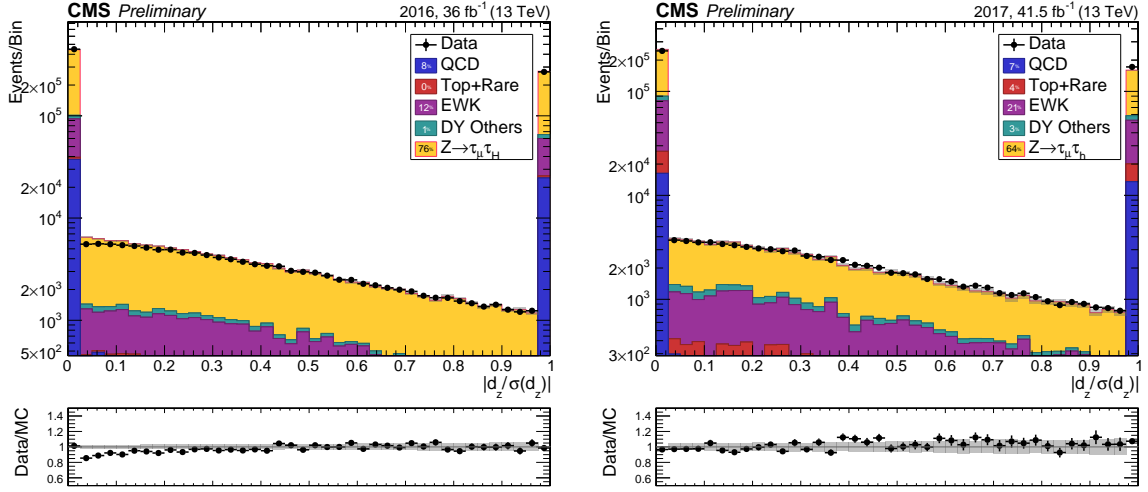


Figure 35: Significance of d_z for the particle flow candidates associated to the probe τ

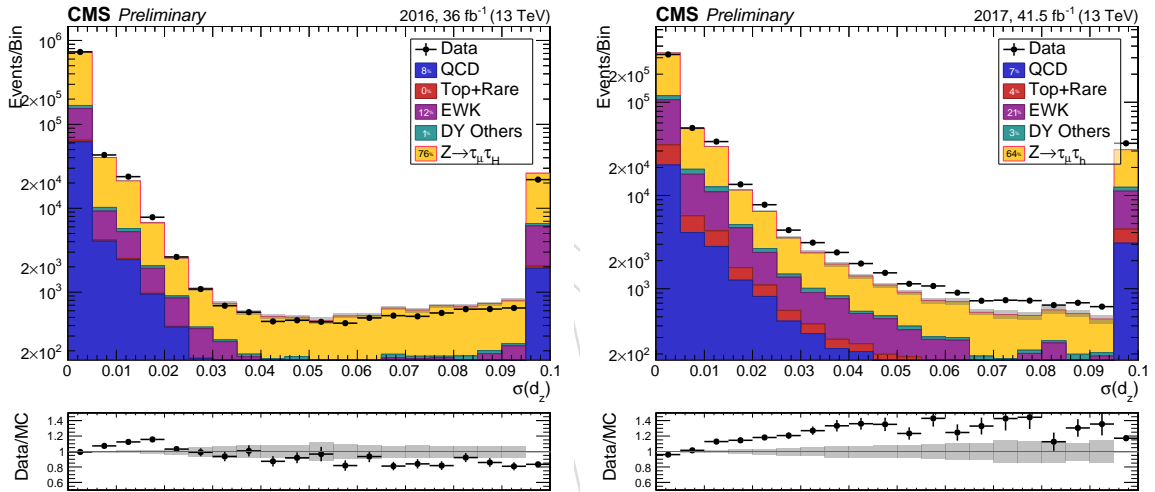


Figure 36: Error of measured d_z for the particle flow candidates associated to the probe τ

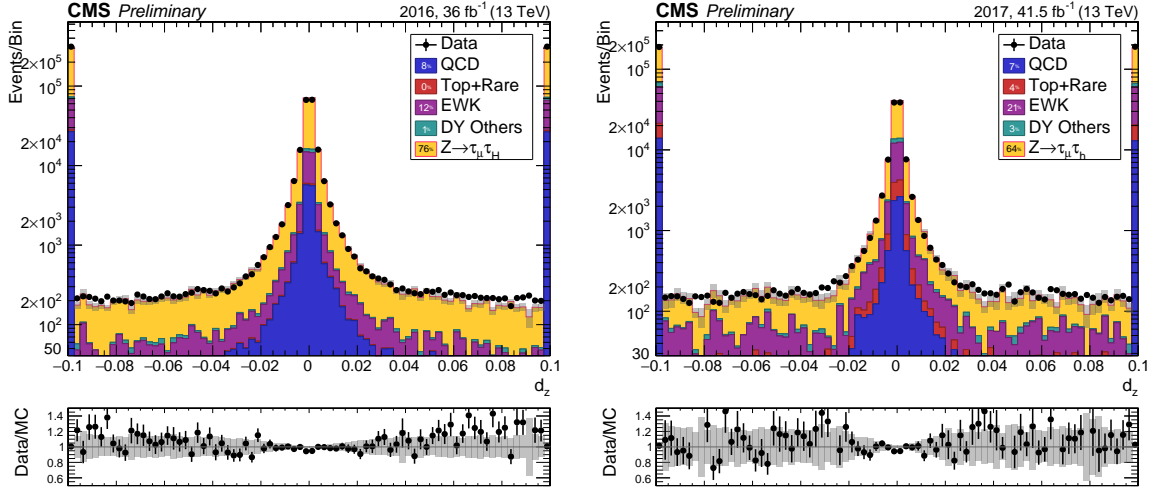


Figure 37: Measured d_z for the particle flow candidates associated to the probe τ

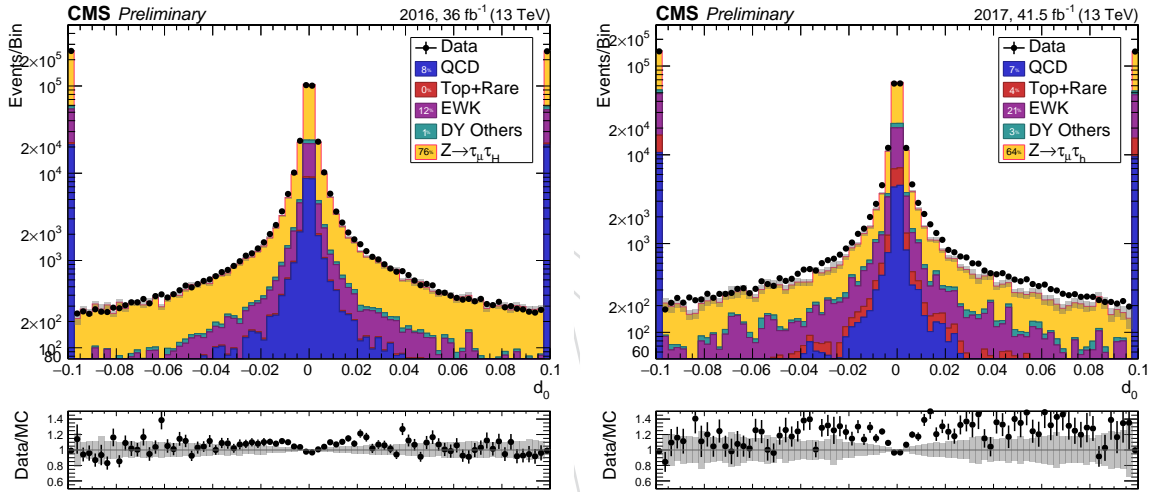


Figure 38: Measured d_0 for the particle flow candidates associated to the probe τ

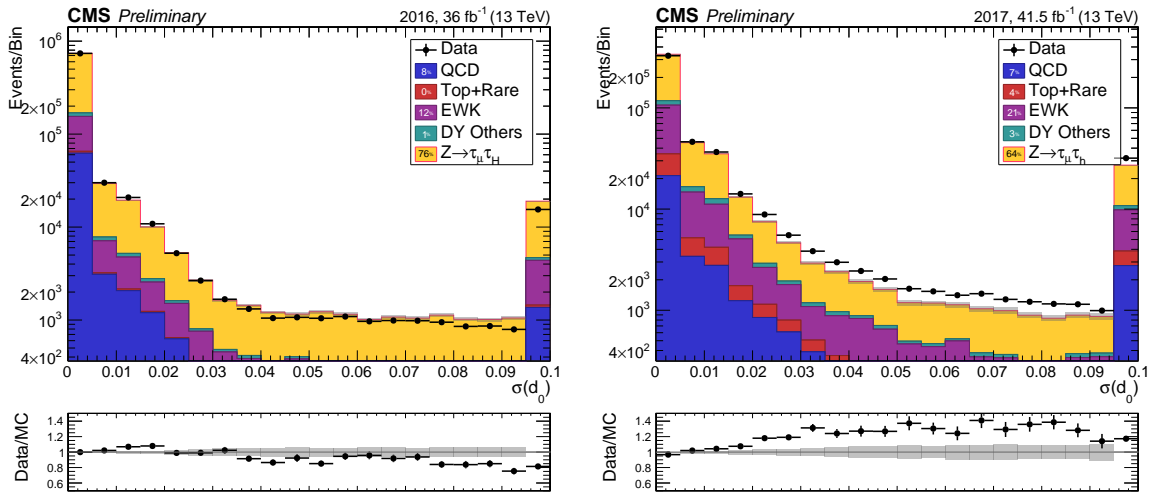
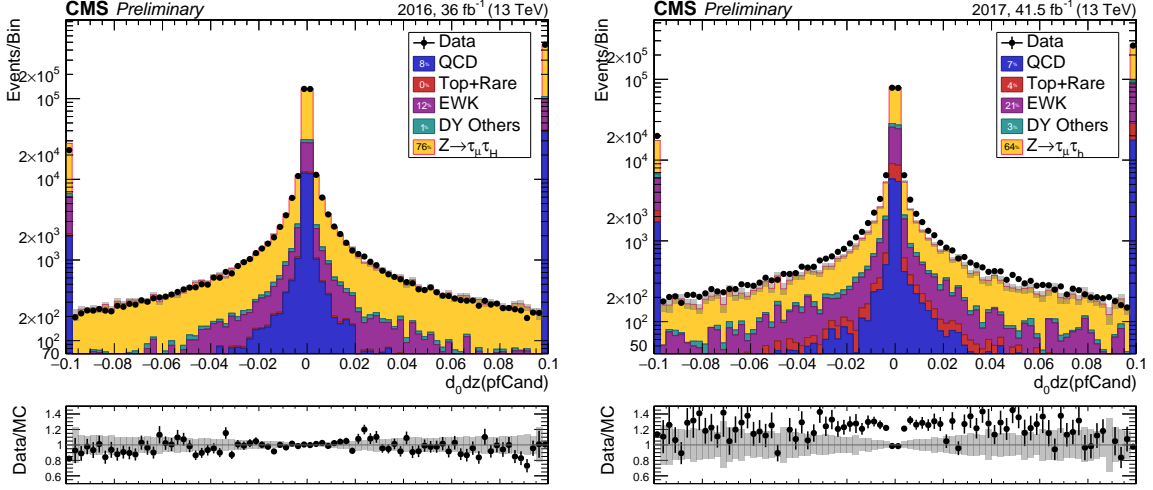
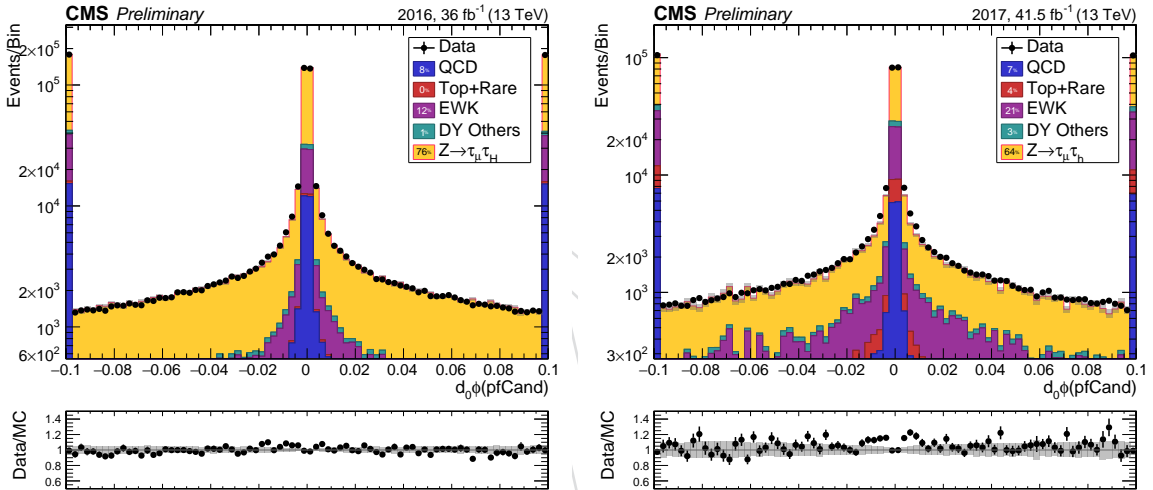
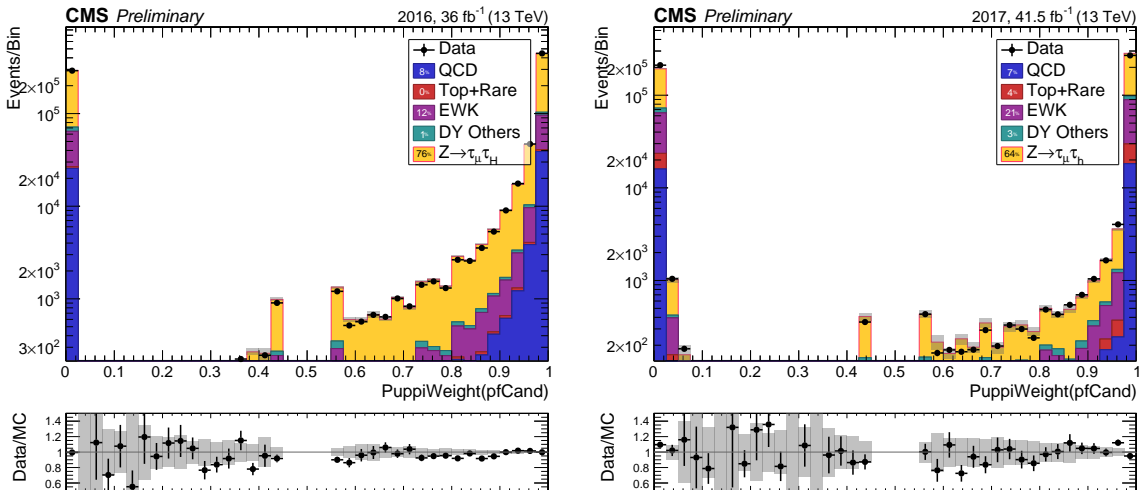


Figure 39: Error of measured d_0 for the particle flow candidates associated to the probe τ

Figure 40: $d_0 d_z$ for the particle flow candidates associated to the probe τ Figure 41: $d_0 \Delta\phi$ for the particle flow candidates associated to the probe τ Figure 42: Puppi weight for the particle flow candidates associated to the probe τ

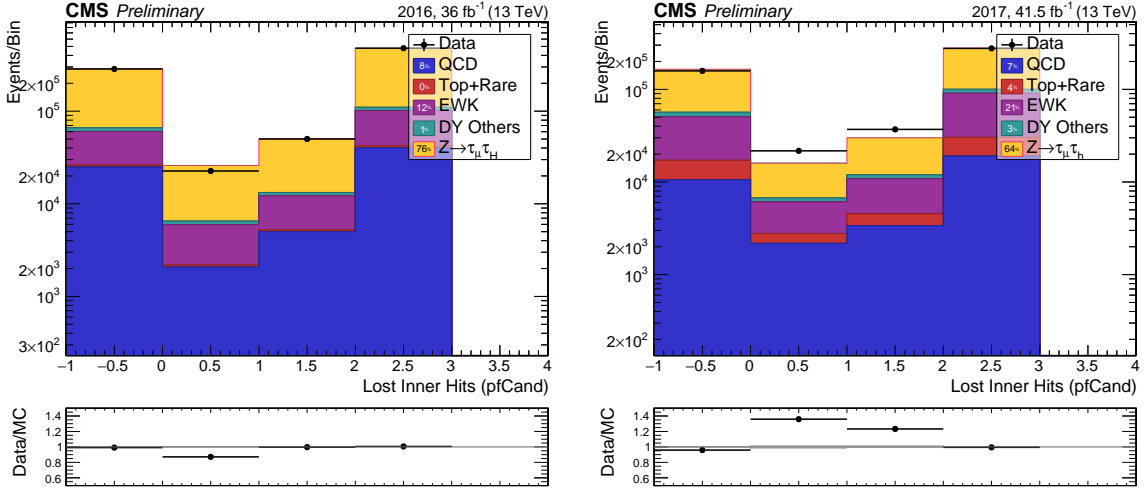


Figure 43: Lost Inner Hits for the particle flow candidates associated to the probe τ

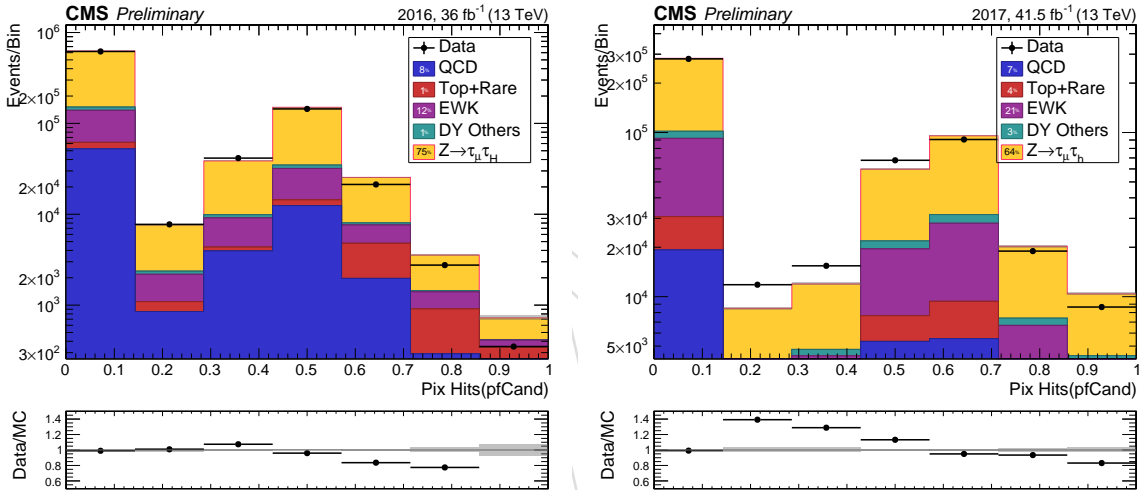


Figure 44: Pixel Hits for the particle flow candidates associated to the probe τ

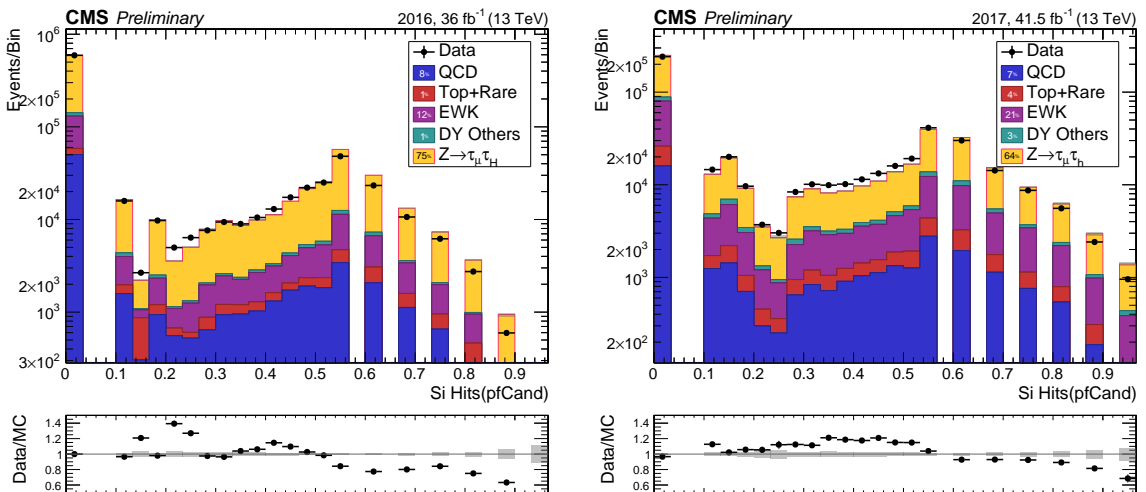


Figure 45: Strip Hits for the particle flow candidates associated to the probe τ

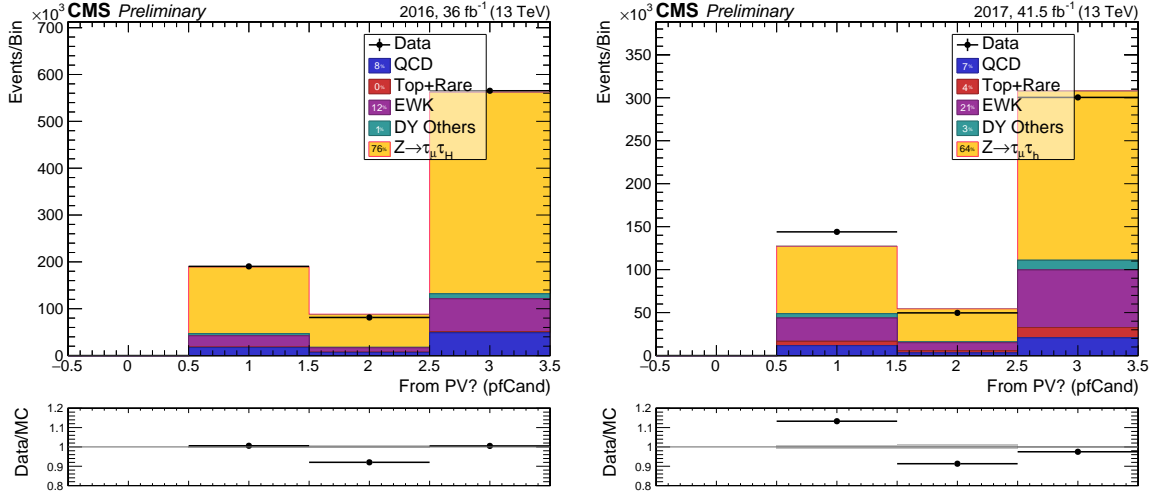


Figure 46: FromPV flag for the particle flow candidates associated to the probe τ

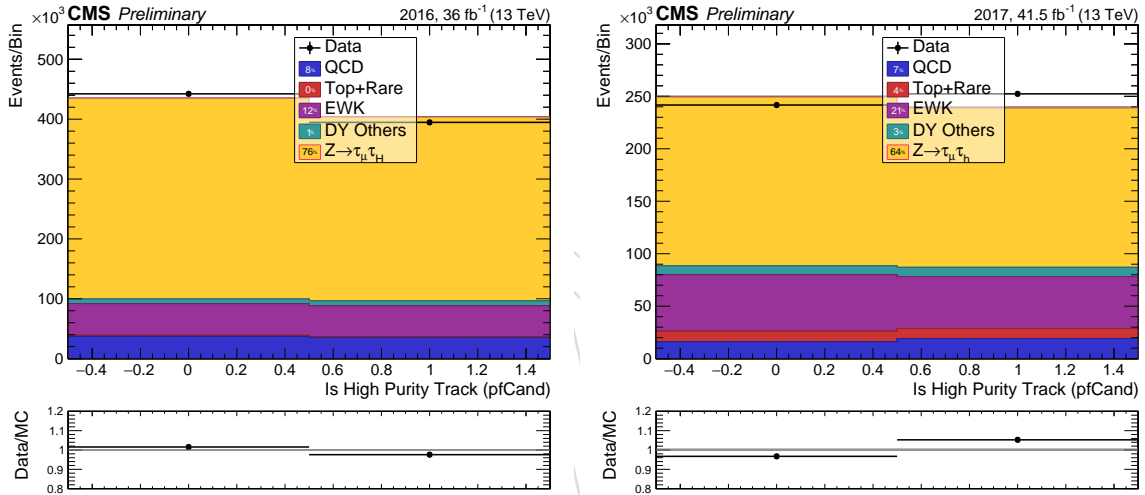


Figure 47: High Purity flag for the particle flow candidates associated to the probe τ

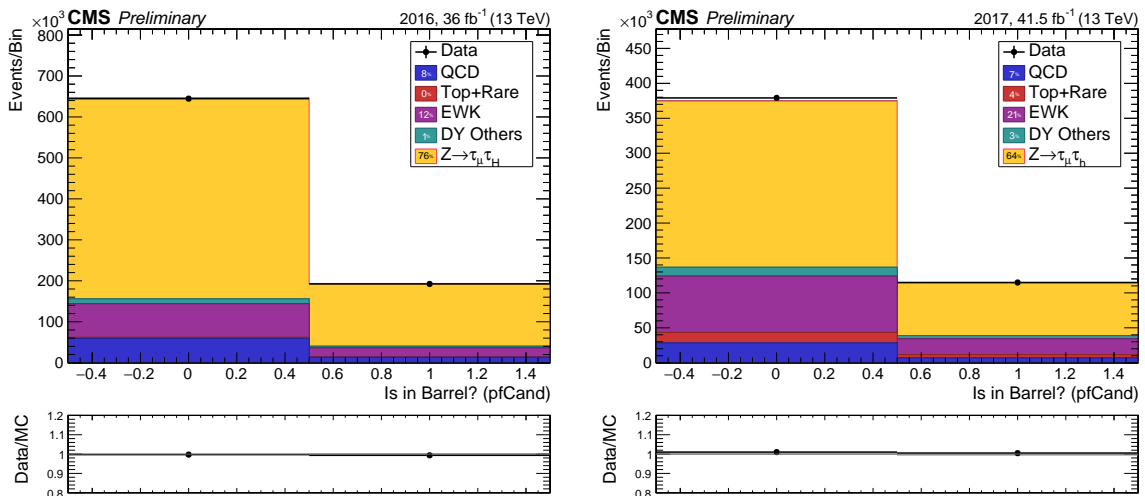


Figure 48: IsBarrel flag for the particle flow candidates associated to the probe τ

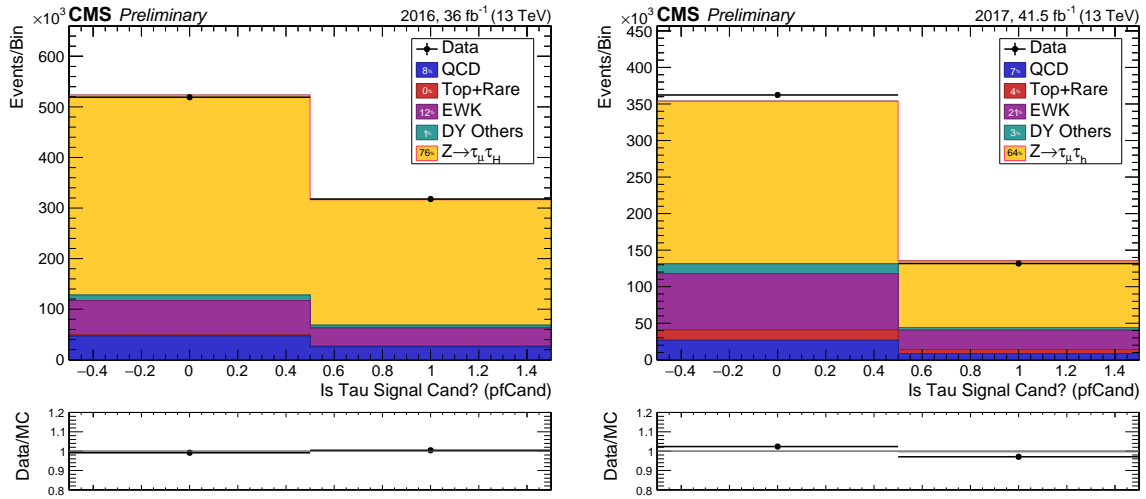


Figure 49: Signal Candidate flag for the particle flow candidates associated to the probe τ

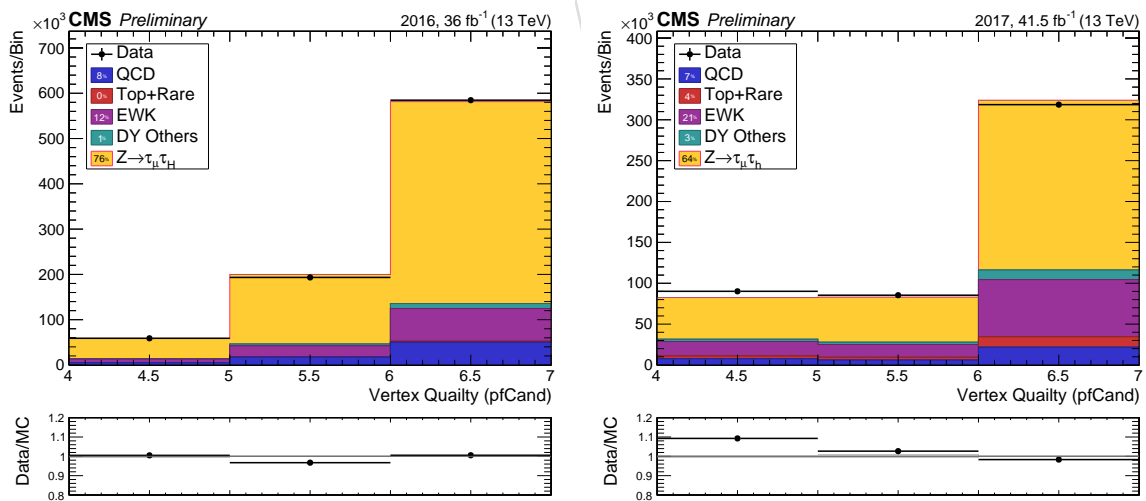


Figure 50: Vertex Quality flag for the particle flow candidates associated to the probe τ

589 B Additional Checks Era Dependency

590 We validate the performance of tau reconstruction across detector conditions by separating the
 591 collected data into multiple eras. HIP issues in 2016 and large dead areas in the pixel detector
 592 for 2017 could have potential impacts on data quality. We check the visible mass in 2016 51
 593 after binning our events by-era, and we check the visible mass in 52 2017 after doing the same
 594 and applying by-era pileup corrections.

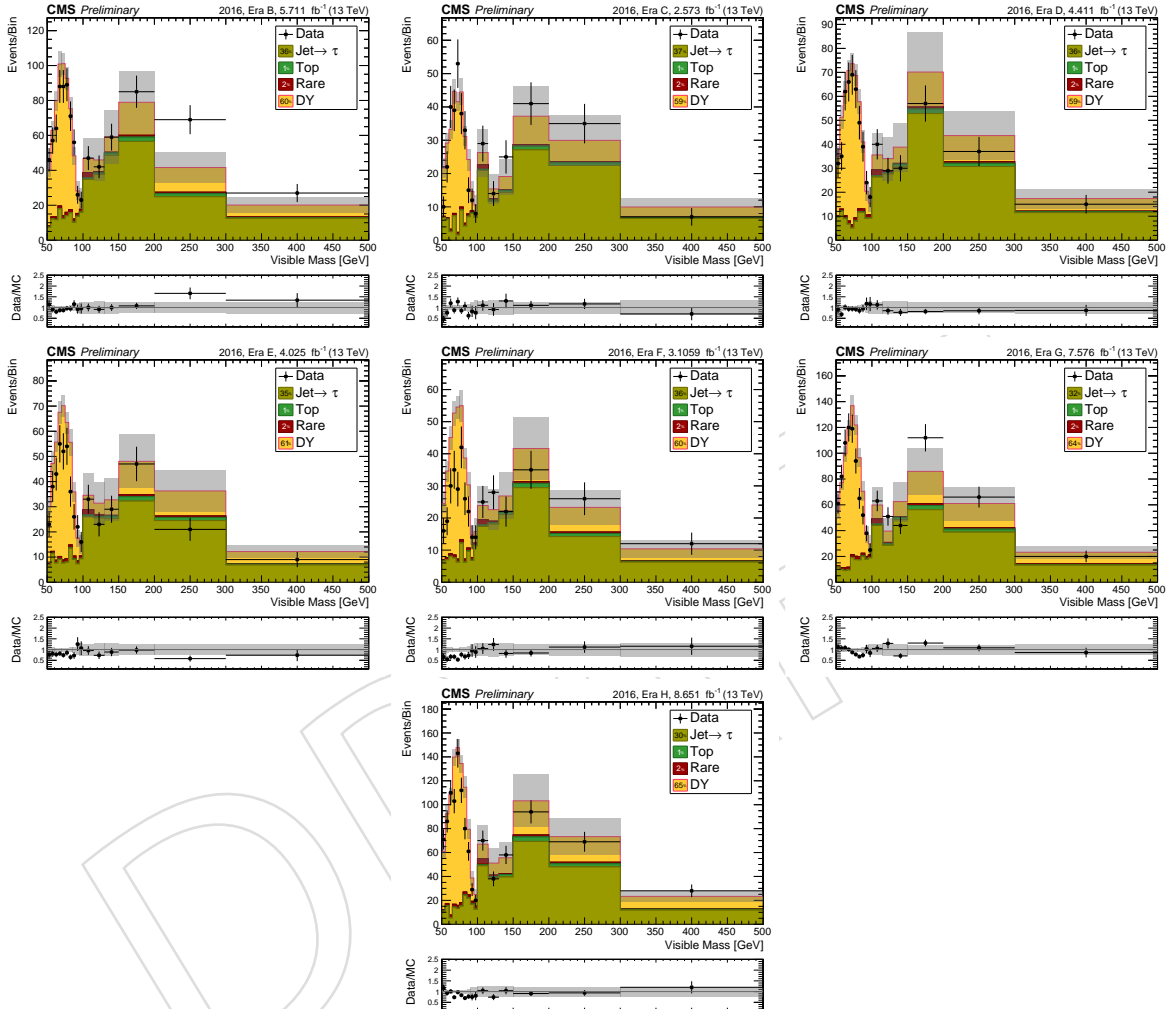


Figure 51: Visible Z mass probes the performance of tau reconstruction for every era of data collection in 2016.

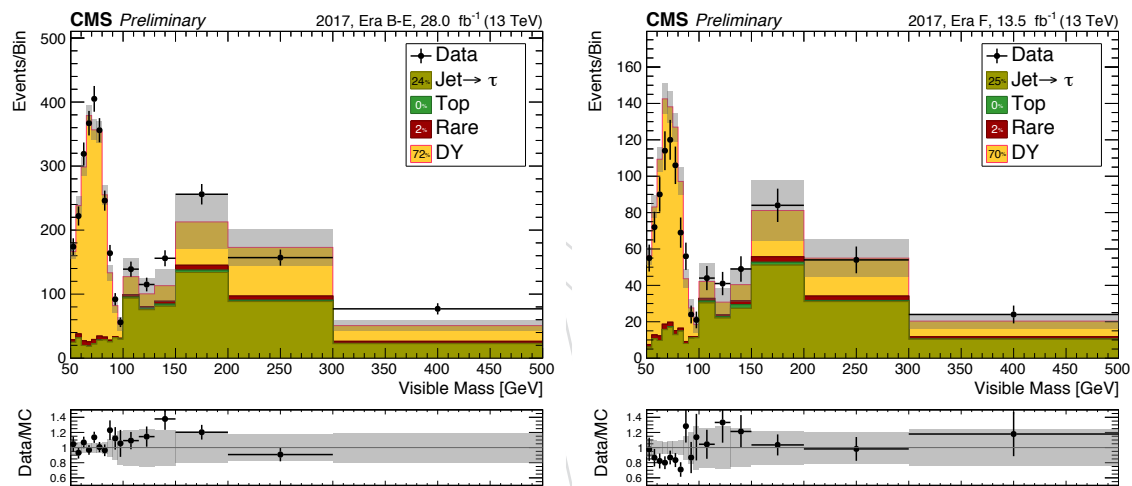


Figure 52: Again, visible Z mass probes the performance of tau reconstruction. This time we consider separately the aggregate regions of eras B-E and eras F.

595

C Additional Checks on Measured Fake Rate

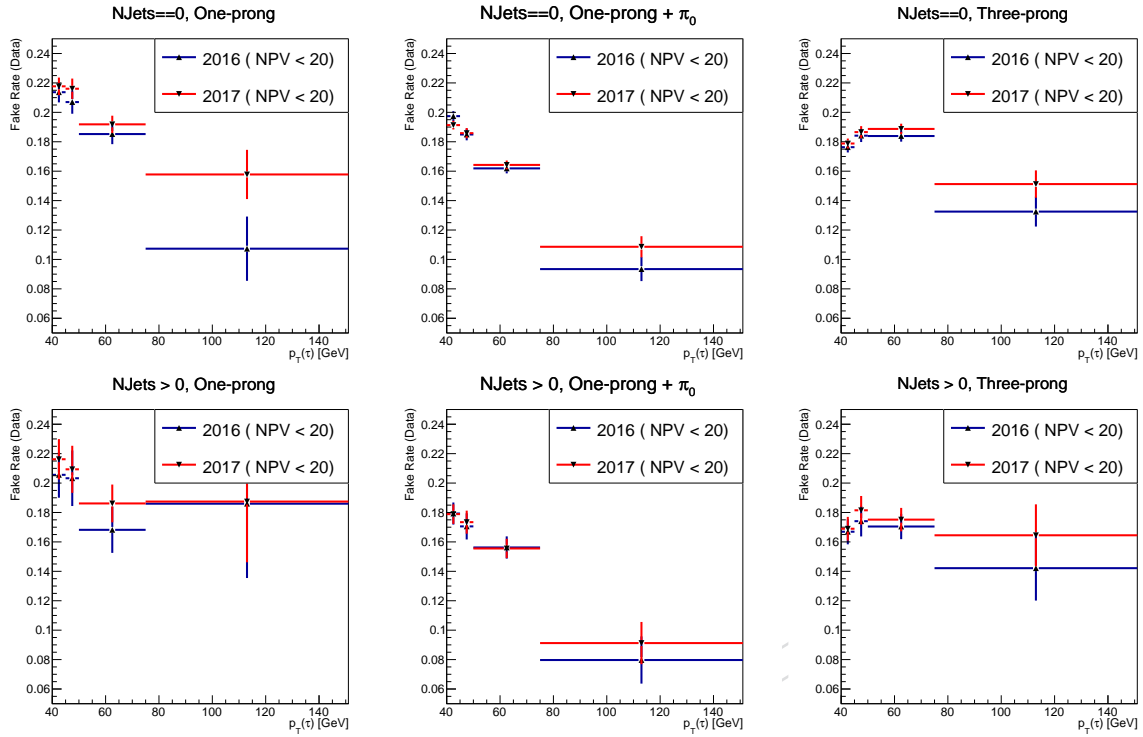


Figure 53: Fake rates measured in (2016, 2017) data for the different τ_h decay modes (left: one-prong, middle: one-prong+ π_0 , right: three-prong) as a function of τ_h p_T , for $N_j == 0$ (upper row) and $N_j > 0$ (lower row). Note that a selection of NPV < 20 has been applied.

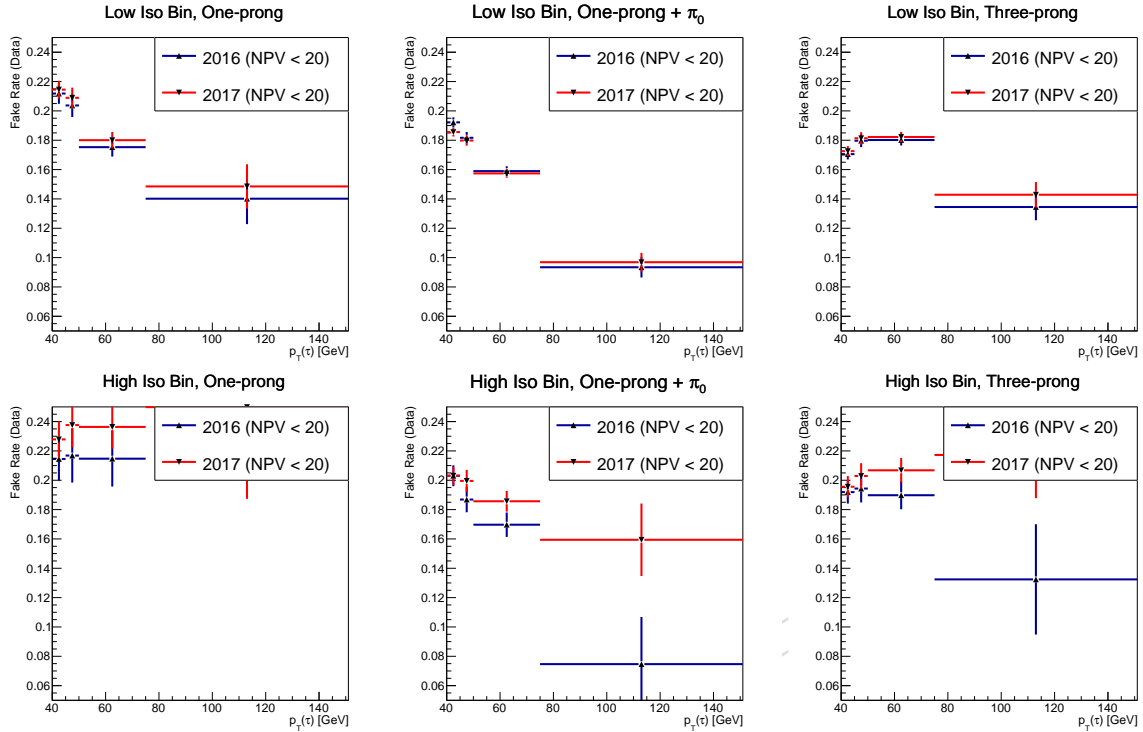


Figure 54: Fake rates measured in (2016, 2017) data for the different τ_h decay modes (left: one-prong, middle: one-prong+ π_0 , right: three-prong) as a function of τ_h p_T , for Opposite Tau isIsolated = False (upper row) and Opposite Tau isIsolated = True (bottom row). Note that a selection of NPV < 20 has been applied.

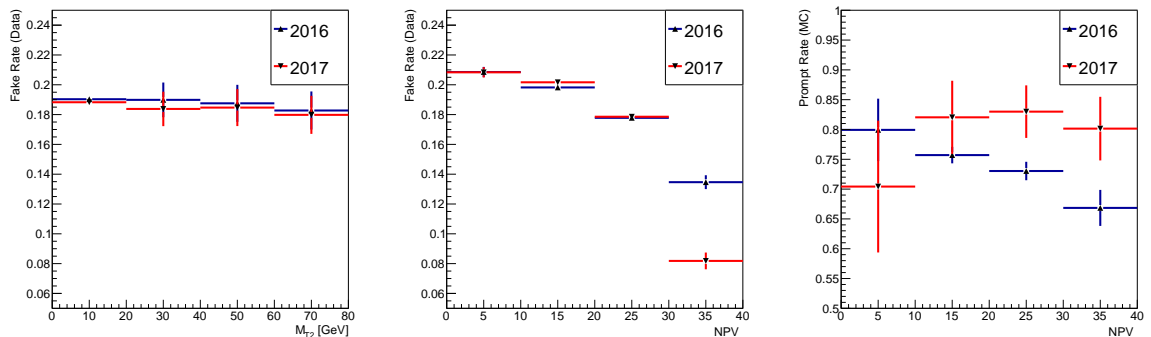


Figure 55: Fake/prompt rates measured in 2016 and 2017 data/MC vs M_{T2} and NPV, left to right respectively. The dependence on prompt rate vs. M_{T2} is found to be flat in simulation (not shown). Together plots illustrate the benefit of binning in NPV and also validate the application of the fake rate method.

596 D Background Validation

597 D.0.1 $\tau_h\tau_h$ -VR

598 Validation of distributions of the relevant kinematic variables in a DY and fake enriched control
 599 region specified by selecting events passing the baseline selection, with $p_T(\tau, \tau) > 50$ GeV and
 600 $\Sigma M_T < 250$ GeV or $M_{T2} < 50$. Lepton and b-tagging vetos are applied.

601 Figs. 57, 58, 59, show the excellent agreement between data and the predicted background
 602 for DY kinematics, tau kinematics and search region variables.

603 In all regions of tau phase space and provides evidence that the constant scale factor applied
 604 for the τ_h selection efficiency is sufficient to capture data/MC differences in τ_h modelling.

605 D.0.2 $\tau_h\tau_h+b$ -VR

606 Validation of distributions of the relevant kinematic variables in a Top enriched control region
 607 specified by selecting events passing the baseline selection, with $p_T(\tau_h, \tau_h) > 50$ GeV and ΣM_T
 608 < 250 GeV or $M_{T2} < 50$. Lepton vetos are applied, whereas the nominal b-tagging veto is
 609 inverted to create a top enriched region.

610 Figs. 60, 61, 62, show the excellent agreement between data and the predicted top background.

611 In all regions of tau phase space and provides evidence that the constant scale factor applied
 612 for the τ_h selection efficiency is sufficient to capture data/MC differences in τ_h modelling.

613 D.0.3 $\mu\tau_h$ -VR

614 Validation of distributions of the relevant kinematic variables in region specified by selecting
 615 event passing the single-muon trigger. The tagged tau must pass $p_T(\tau_h) \geq 40$ GeV, whereas
 616 the isolated muon must pass $p_T(\mu) \geq 30$ GeV. On top of that with selections are applied to
 617 mirror the nominal search region selections, $p_T(\mu, \tau_h) > 50$ GeV and $\Sigma M_T < 250$ GeV or M_{T2}
 618 < 50 . Additional lepton vetos are applied.

619 Figs. 63, 64, 65, show the excellent agreement between data and the predicted background
 620 for both top and DY.

621 In all regions of tau phase space and provides evidence that the constant scale factor applied
 622 for the τ_h selection efficiency is sufficient to capture data/MC differences in τ_h modelling.

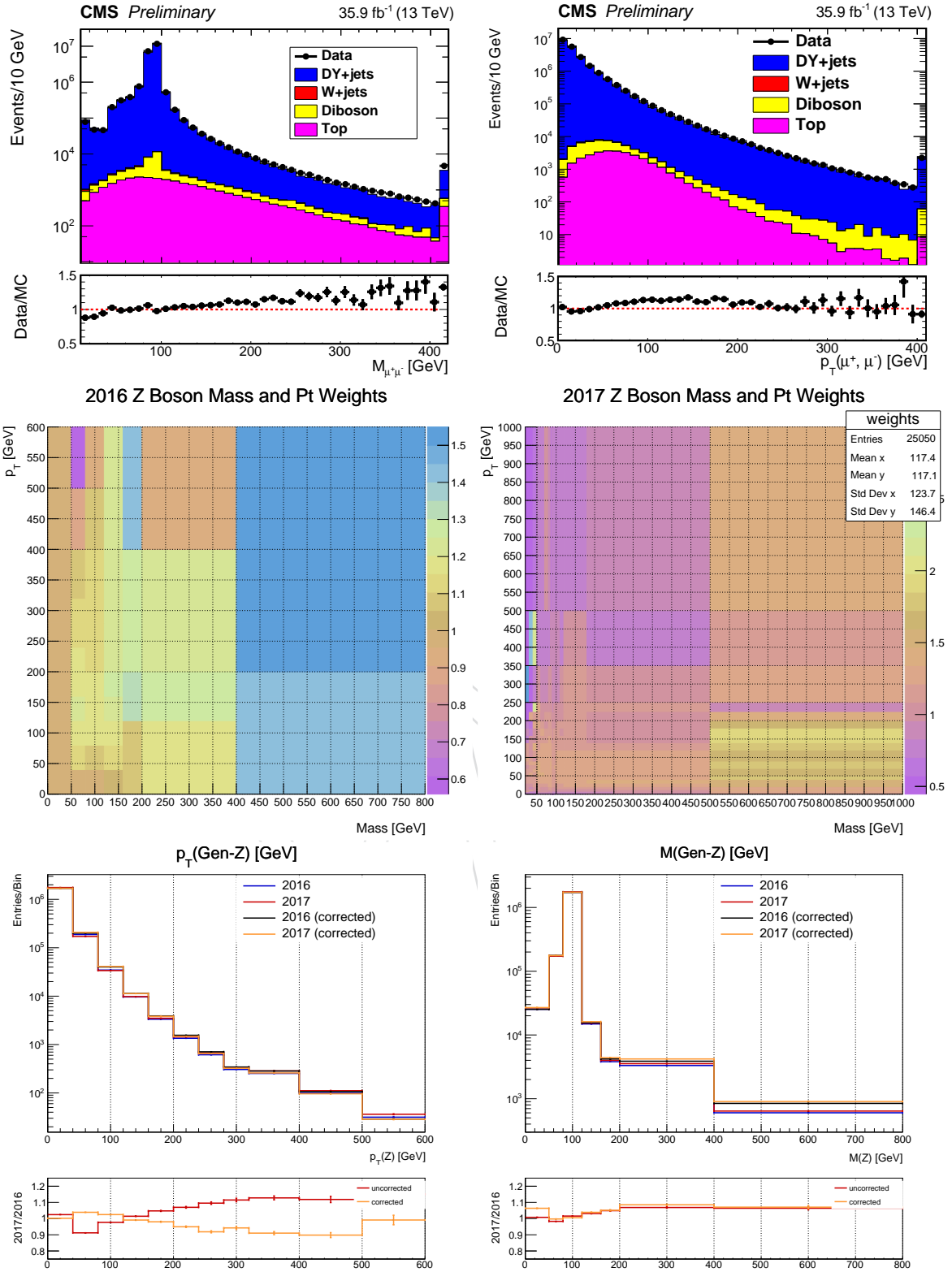


Figure 56: Comparison of Drell-Yan mass shape and p_T spectrum in $Z \rightarrow \mu\mu$ events between data and simulation (2016, top). The discrepancies are partially due to the use of LO simulation, which has known limitations in the description of these spectra. The measured weights for 2016 and 2017 are then shown (middle). Lastly we show the generator mass and p_T spectrums for DY before and after corrections in 2016 and 2017 (bottom).

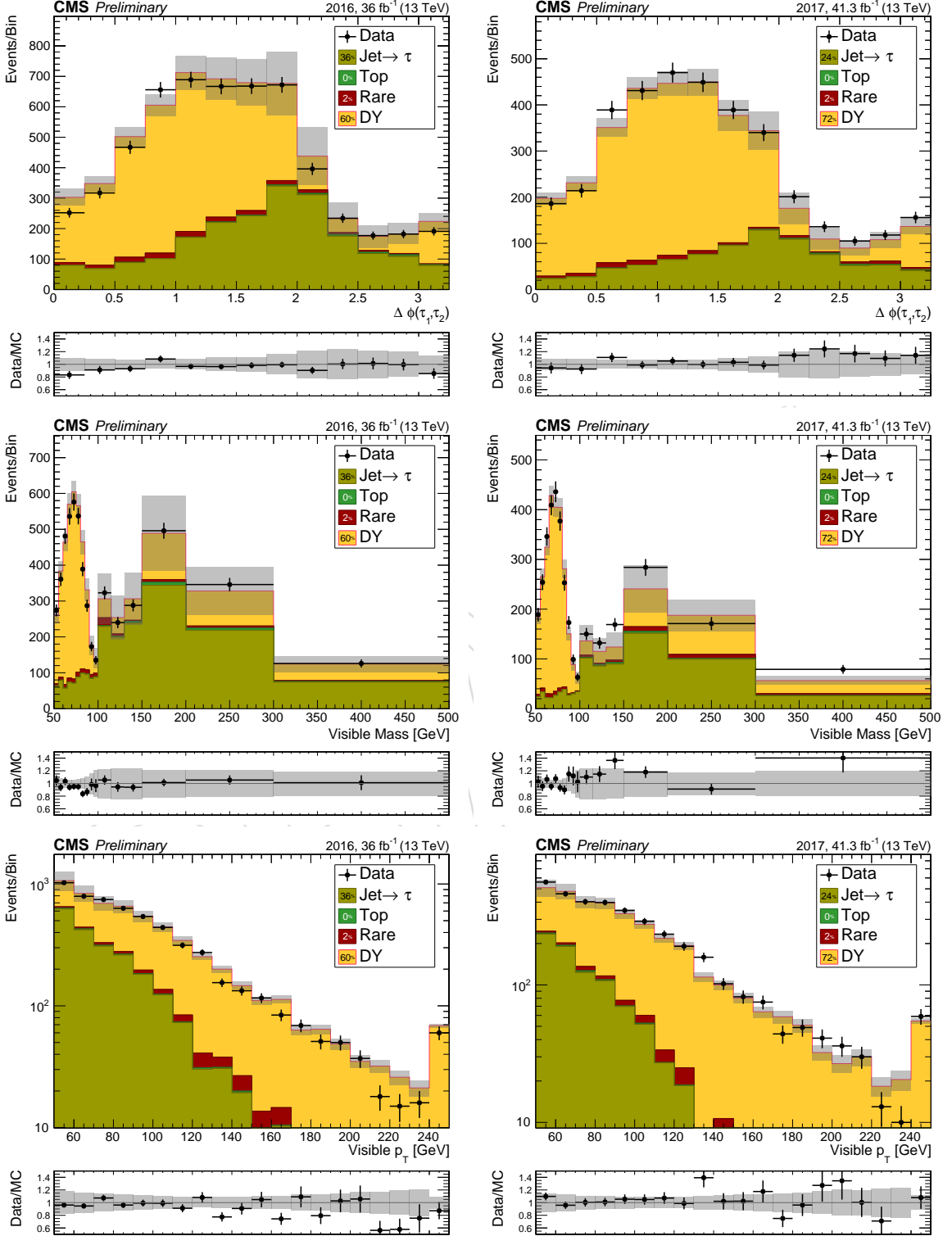


Figure 57: From top to bottom : $\Delta\phi(\tau, \tau)$, visible mass, visible p_T and p_T^{miss} for $\tau\tau$ -VR in Data/MC (2016 on left, 2017 on right).

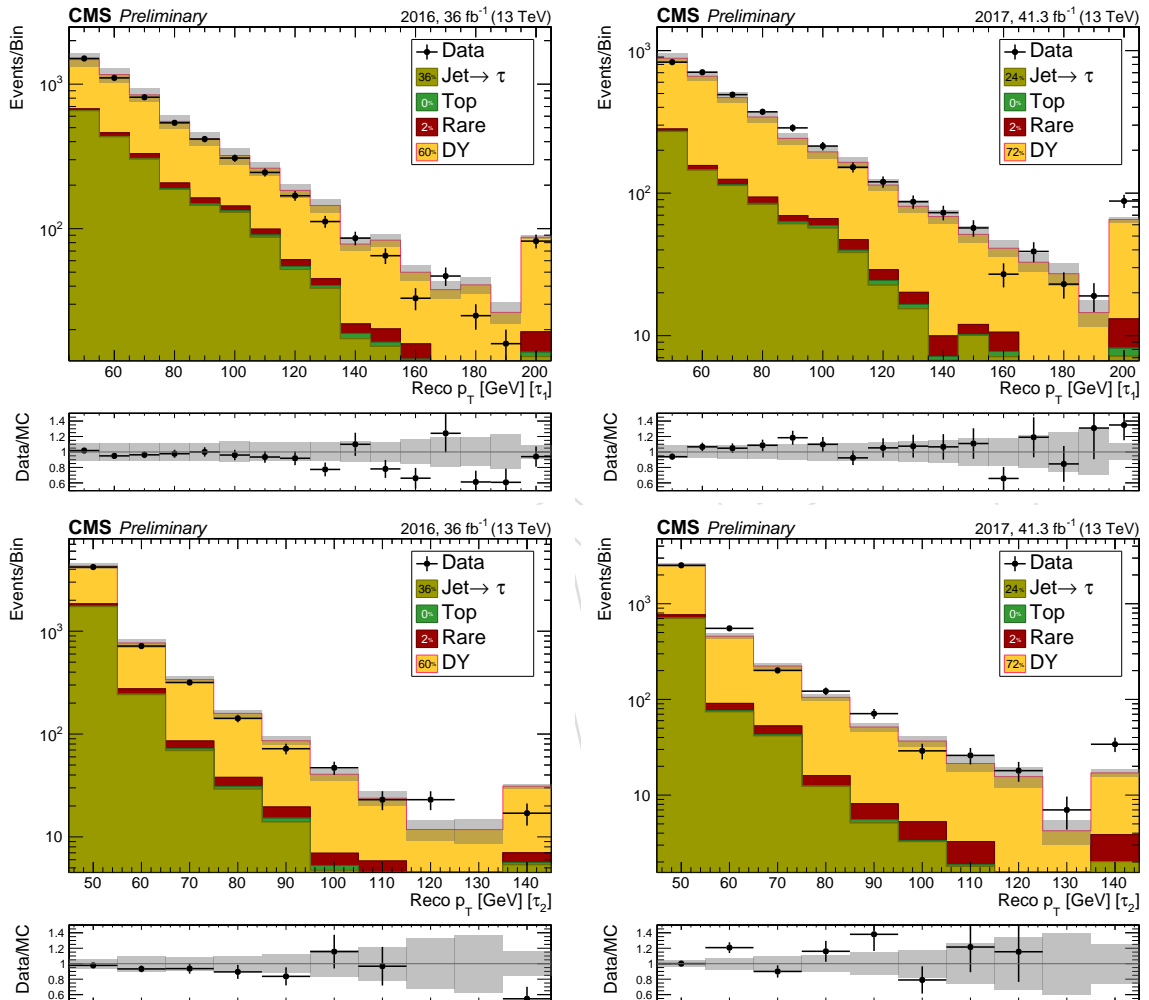


Figure 58: From top to bottom : Leading and sub-leading tau p_T for $\tau\tau$ -VR in Data/MC (2016 on left, 2017 on right).

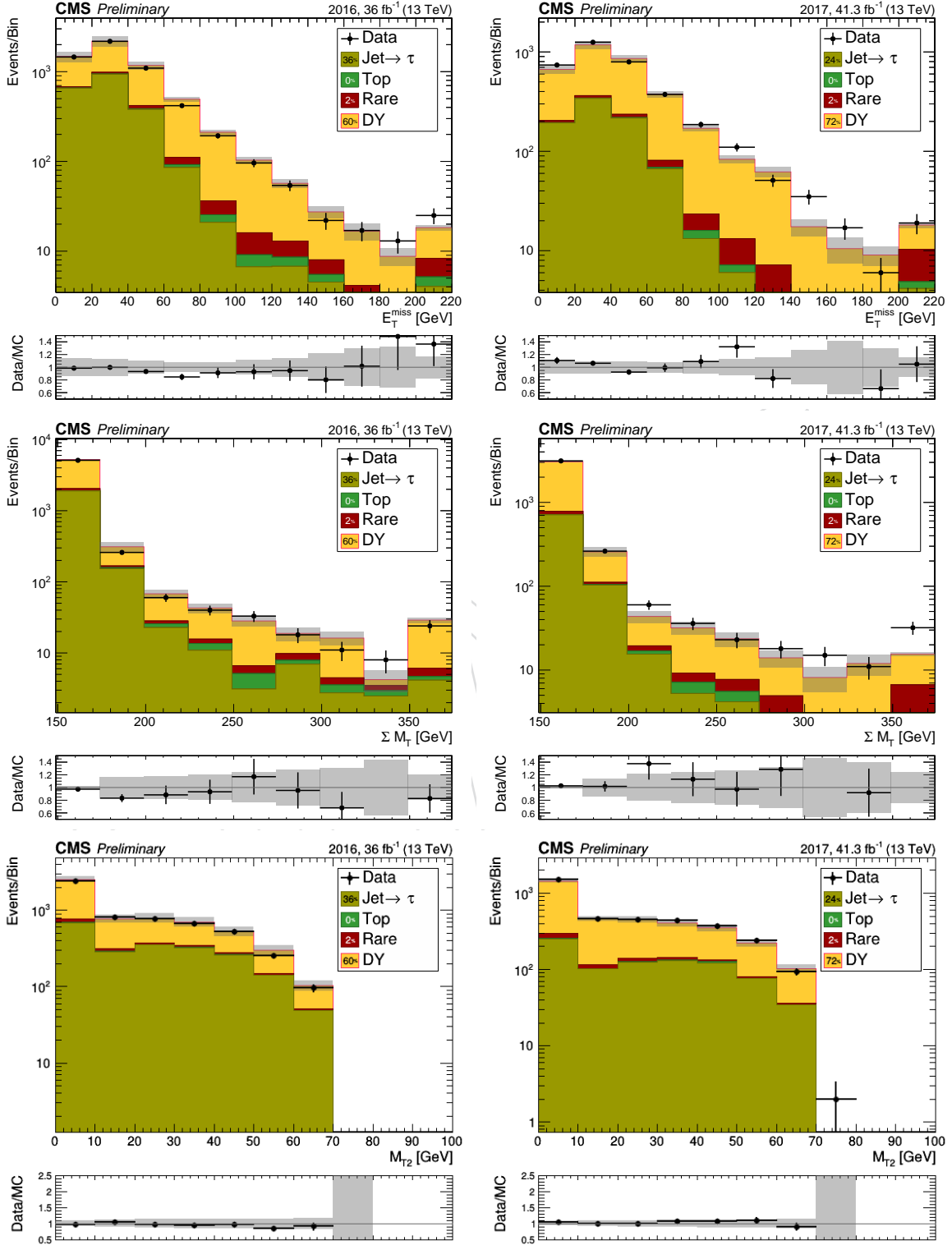


Figure 59: ΣM_T spectrums for $\tau\tau$ -VR in Data/MC 2016 (2017) on left (right)

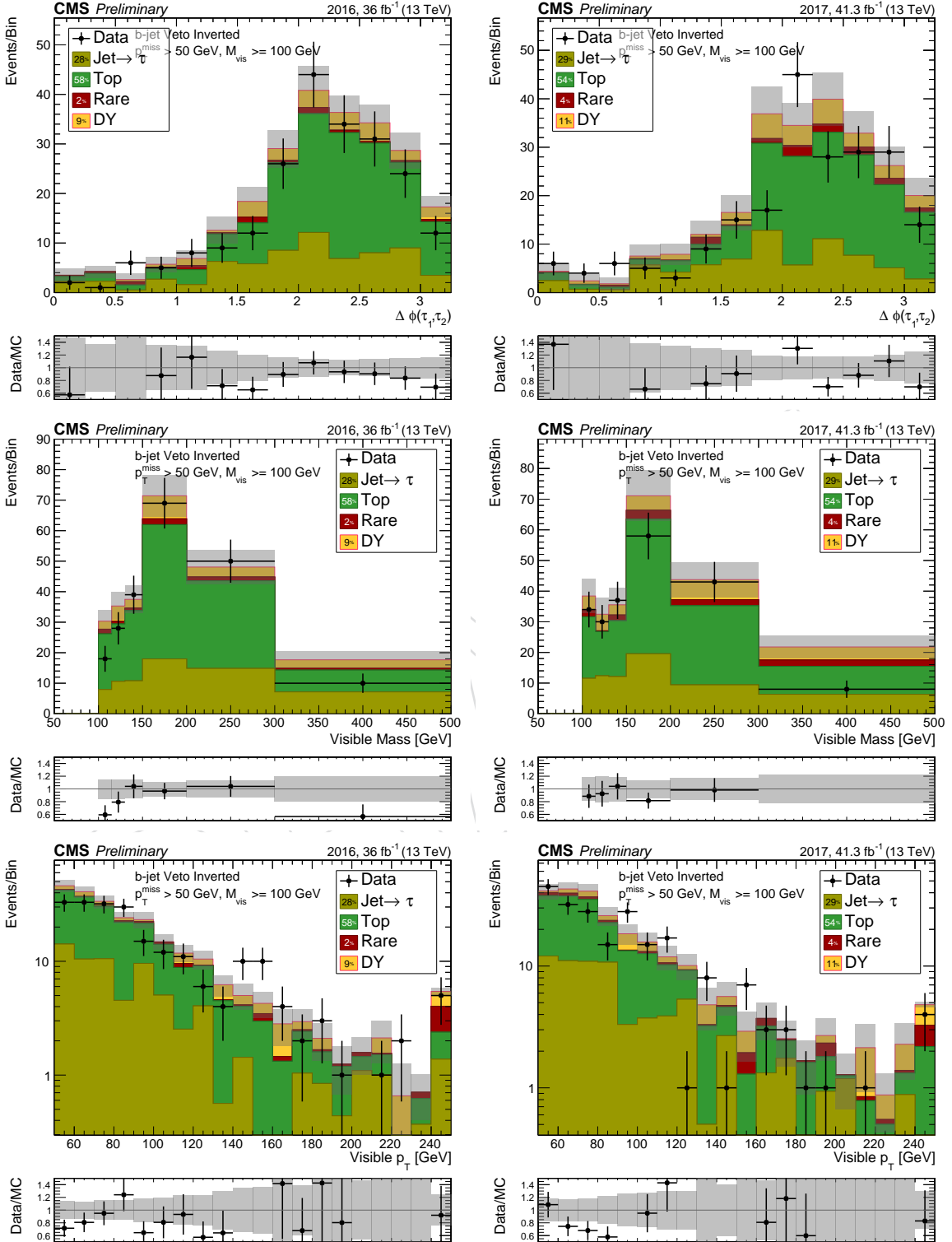


Figure 60: From top to bottom : visible mass, visible p_T and p_T^{miss} for $\tau\tau + b\text{-VR}$ in Data/MC (2016 on left, 2017 on right).

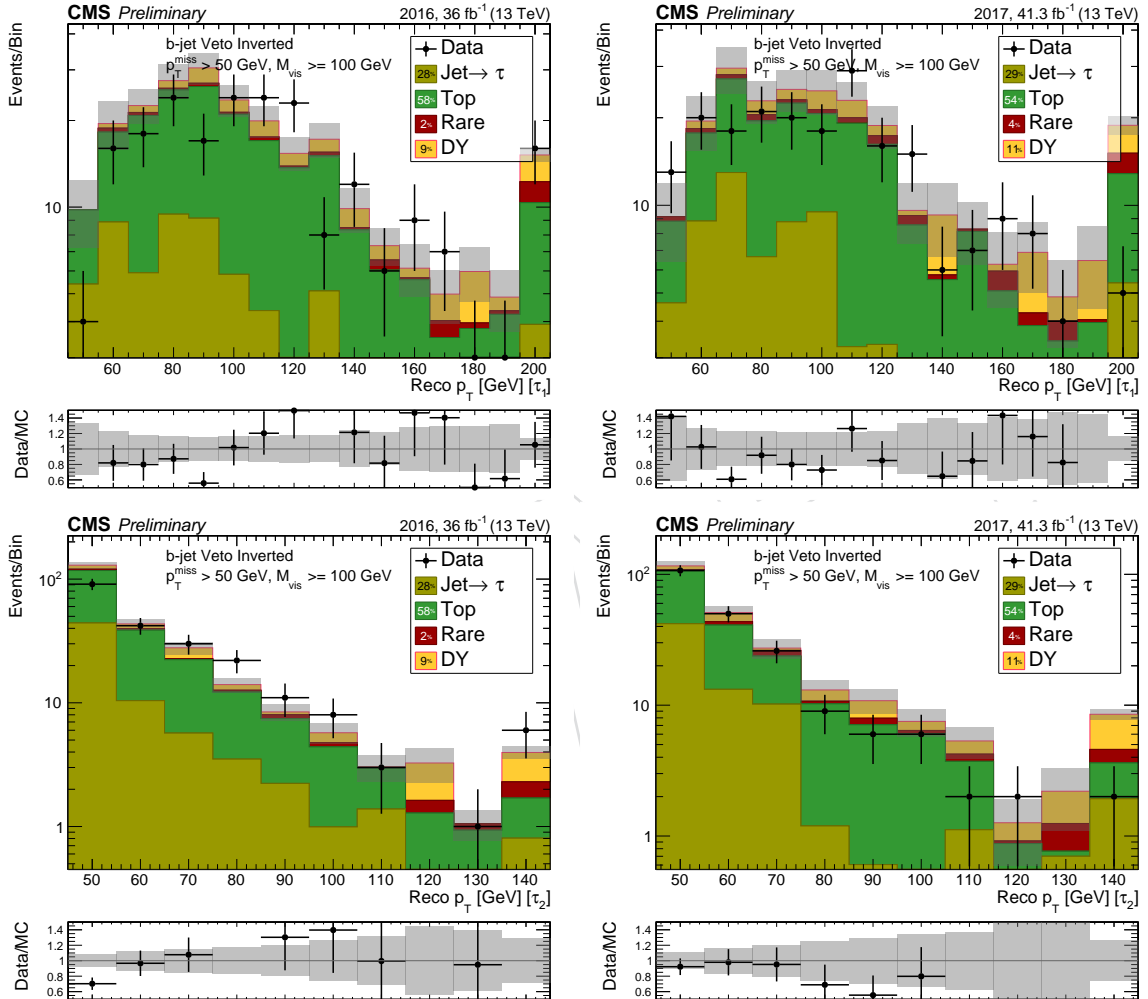
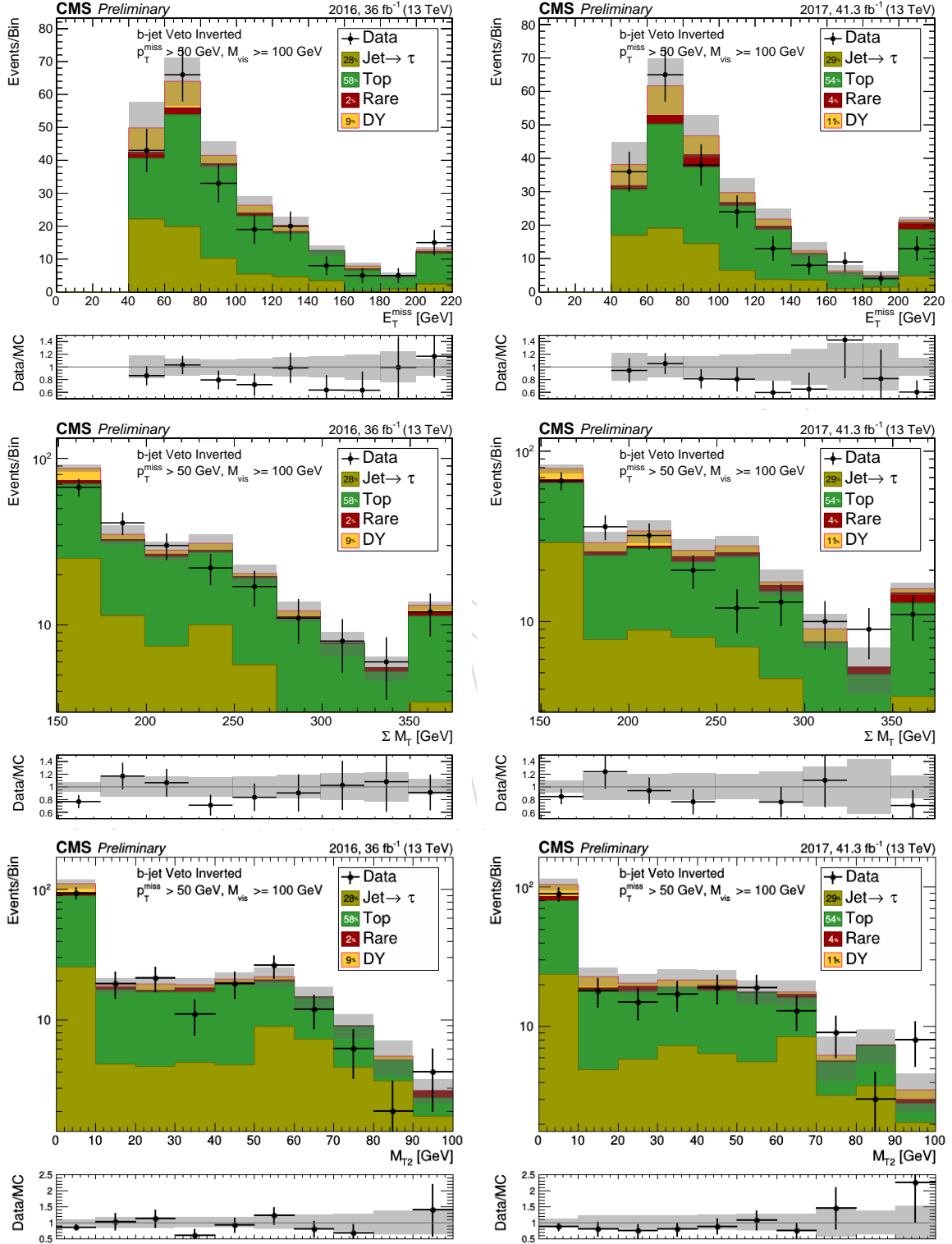


Figure 61: From top to bottom : Leading and sub-leading tau p_T for $\tau\tau+b\text{-VR}$ in Data/MC (2016 on left, 2017 on right).

Figure 62: ΣM_T spectrums for $\tau\tau+b$ -VR in 2016 (2017) on left (right)

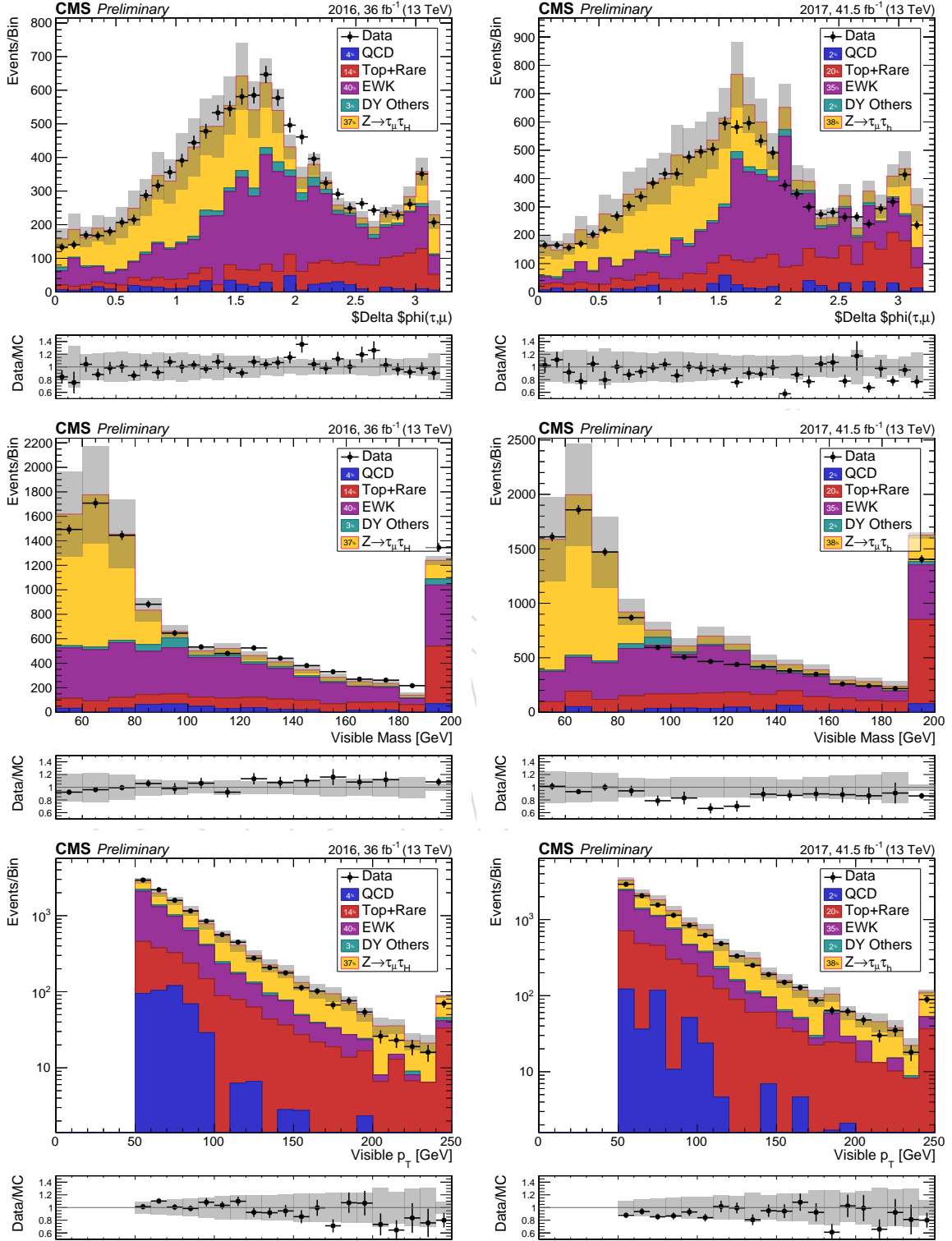


Figure 63: From top to bottom : visible mass, visible p_T and p_T^{miss} for $\tau\mu$ -VR in Data/MC (2016 on left, 2017 on right).

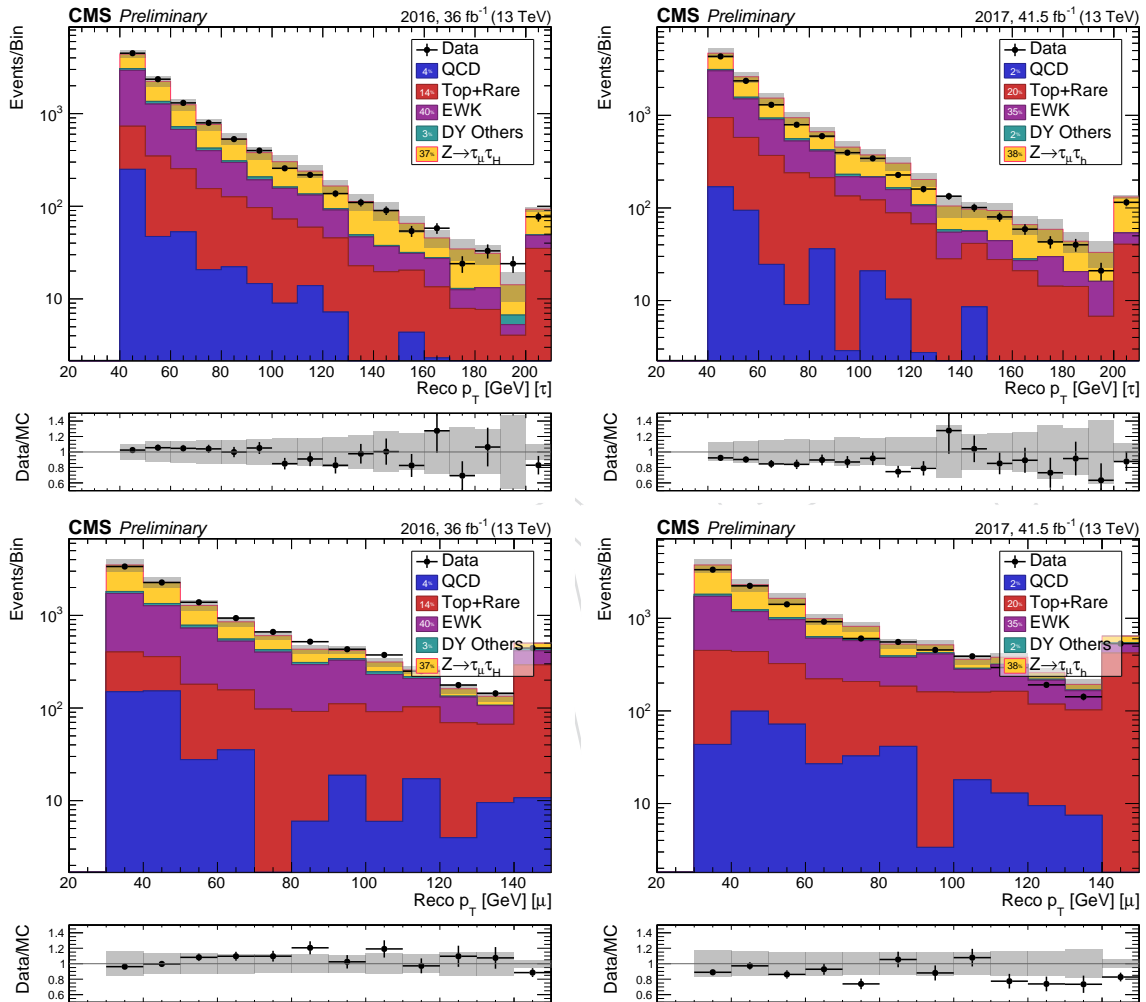


Figure 64: From top to bottom : Leading and sub-leading tau p_T for $\tau\mu$ -VR in Data/MC (2016 on left, 2017 on right).

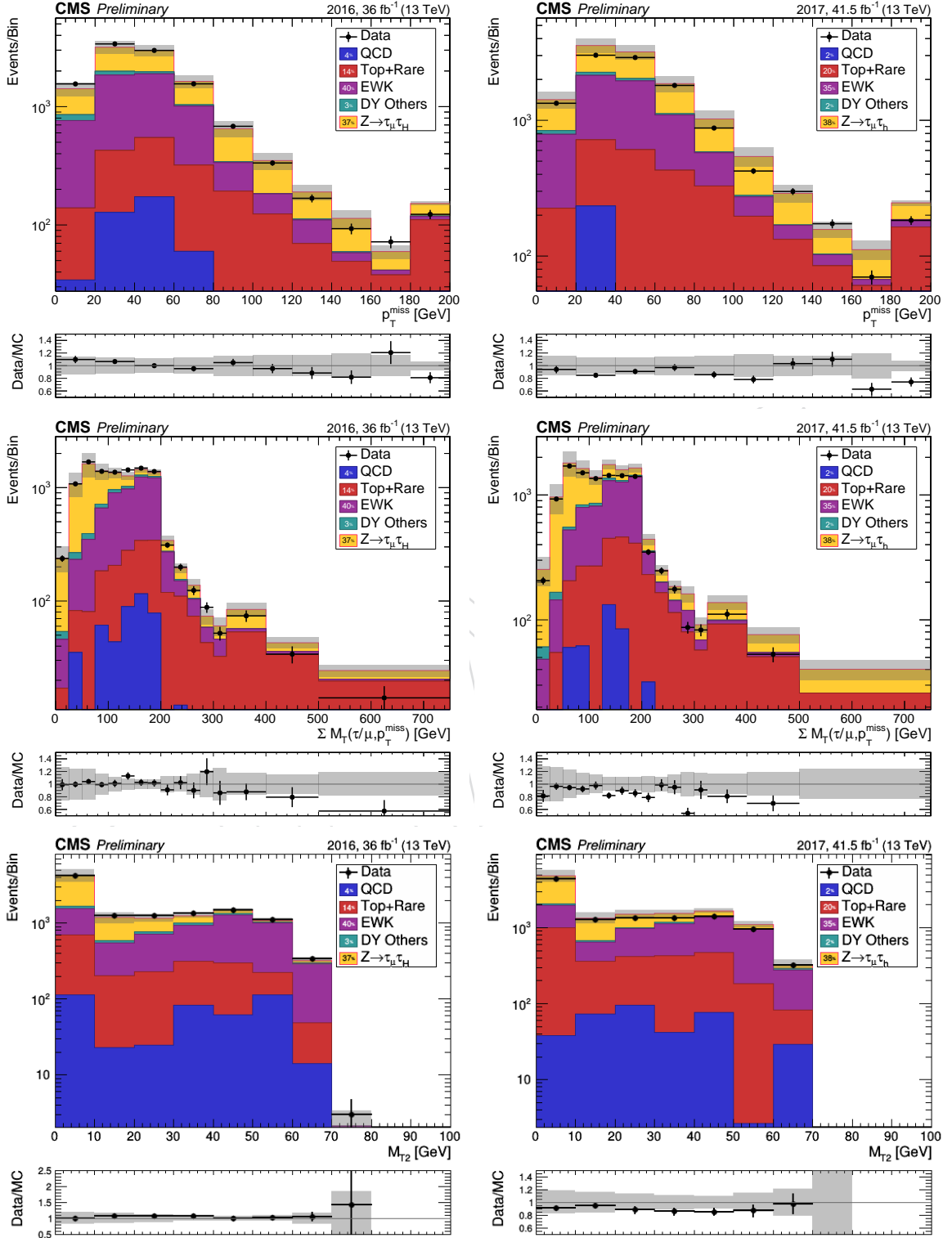


Figure 65: ΣM_T spectrums for $\tau\mu+VR$ in 2016 (2017) on left (right)

623 **E Impact of Pre-fire Issue**

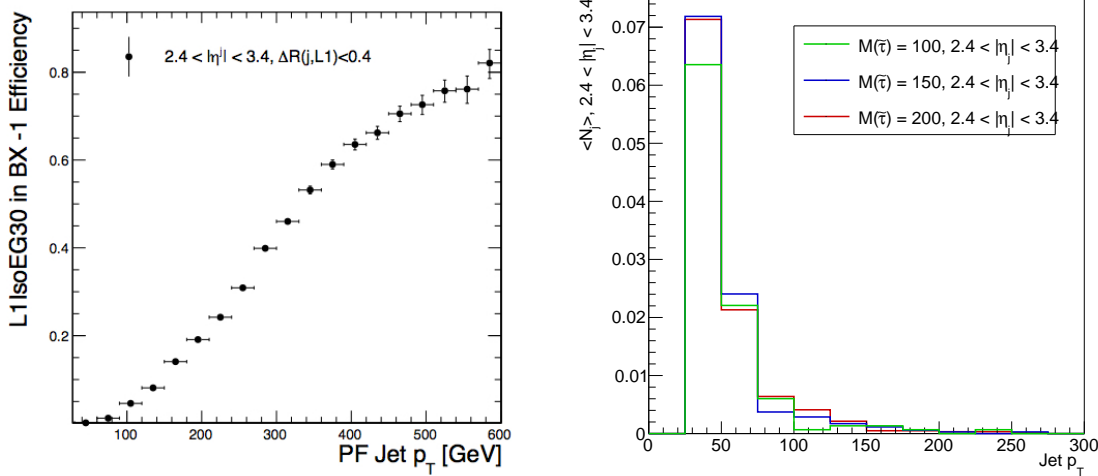


Figure 66: Pre-fire rate is shown on the left, whereas the expected number of high p_T forward jets per signal event are shown on the right.

624 L1 trigger rules forbid consecutive bunch crossings to fire. The ECAL pre-fire issue then causes
 625 events with high p_T forward objects to suffer from reduced trigger efficiency. The pre-fire
 626 efficiency is measured in orthogonal trigger sets to be below 5% for forward jets with $p_T < 100$
 627 GeV, and between 5-20 % for jets with $100 < p_T < 200$ GeV. By inspecting the expected number
 628 of hard forward jets per signal event, and the pre-fire efficiency we conclude that the pre-fire
 629 issue will not significantly impact our analysis. Intuitively we understand this to be because
 630 we are targetting weakly produced SUSY events, rather than strongly produced events which
 631 typically have more ISR/FSR jets.

632 **F Tau Trigger Impact**

633 The tau POG provided trigger scale factors are provided as a function of offline isolation, p_T ,
 634 and decay mode (phi) in 2016 (2017). Because we are using our own custom tau identification
 635 algorithm
 636 From the correlation between the DeepPF tau isolation, the good agreement seen in the di-
 637 tau validation region, and from the minimal expected variation for of the trigger scale factor
 638 versus isolation (for tightly isolated taus), we conclude that the very tight trigger scale-factors
 639 provided by the tau pog prove adequate for our analysis' needs.

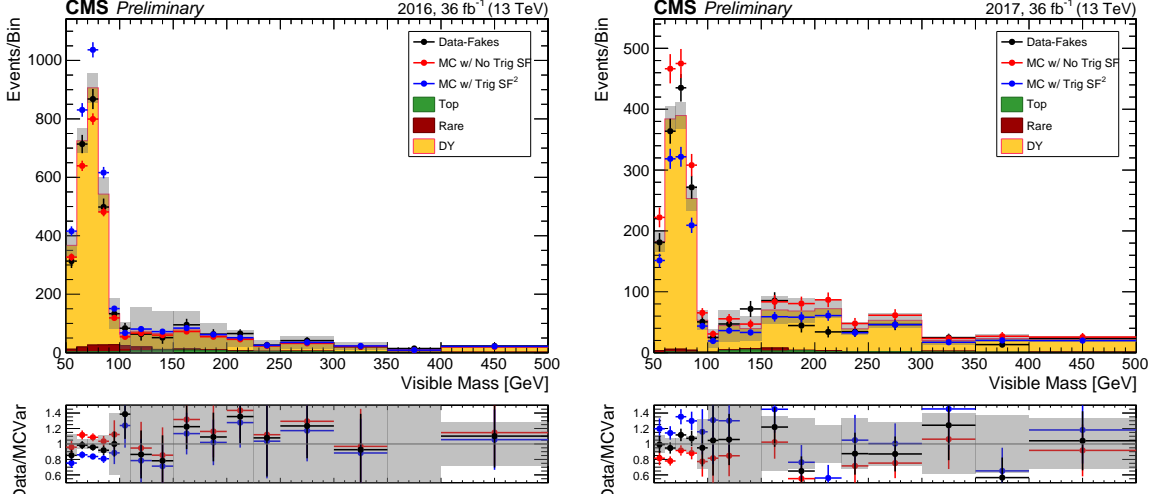


Figure 67: Fake-subtracted data yields for 2016 and 2017 data samples. The MC predictions are shown with the measured trigger scale-factor varied from 1 to the square if it's value.

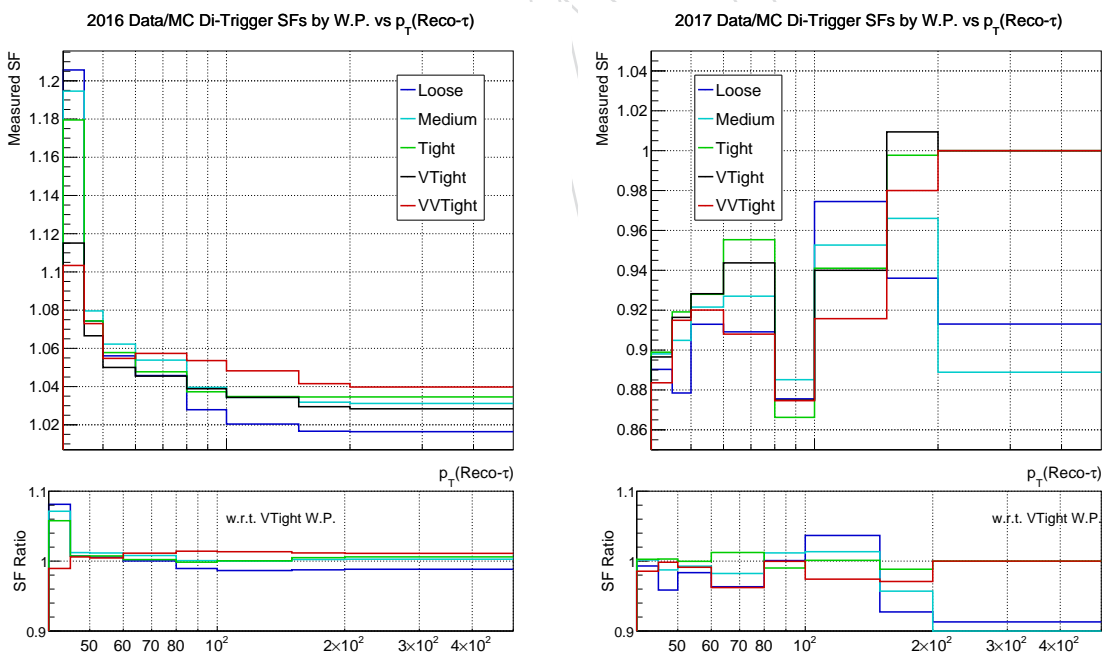


Figure 68: Measured scale-factor variation by offline MVA working point is shown above as a function of the reconstructed tau p_T . Overall a relatively minimal variation is seen for tightly isolated taus.

640 **G p_T^{miss} Recipe Impact**

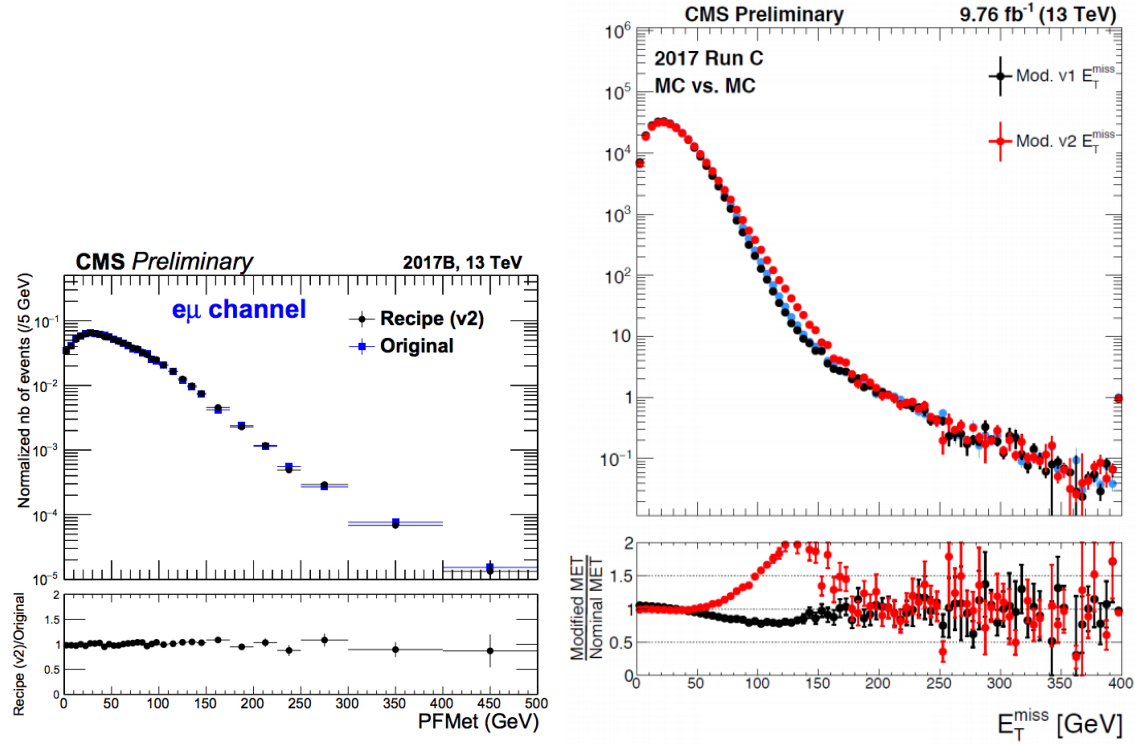


Figure 69: Left plot above shows that the 2017 MET recipe does not significantly impact genuine p_T^{miss} distributions, however, the right shows that the tails from instrumental effects in DY+jets is increased by as much as a factor of two

641 H_T (Soft, Forward) Veto

642 As described in Sec. G there exists a data-MC discrepancy due to noise issues in the forward
 643 ECAL. To mitigate the increased background and chance for spurious events we introduce a
 644 new variable, H_T (Soft,Forward), which is defined as the H_T of the jets neglected from the p_T^{miss}
 645 V2 calculation. Events with large H_T (Soft,Forward) may contain genuine underlying soft activi-
 646 ty which in turn is not included in the p_T^{miss} calculation, and therefore backgrounds associated
 647 with Drell-Yan and misidentified τ_h are increased. To control this new background we intro-
 648 duce a veto: H_T (Soft,Forward) < 50 GeV after correcting the distribution in simulation for the
 649 discrepancies observed between data and simulation. Further checks validated that this does
 not adversely impact the data-MC agreement.

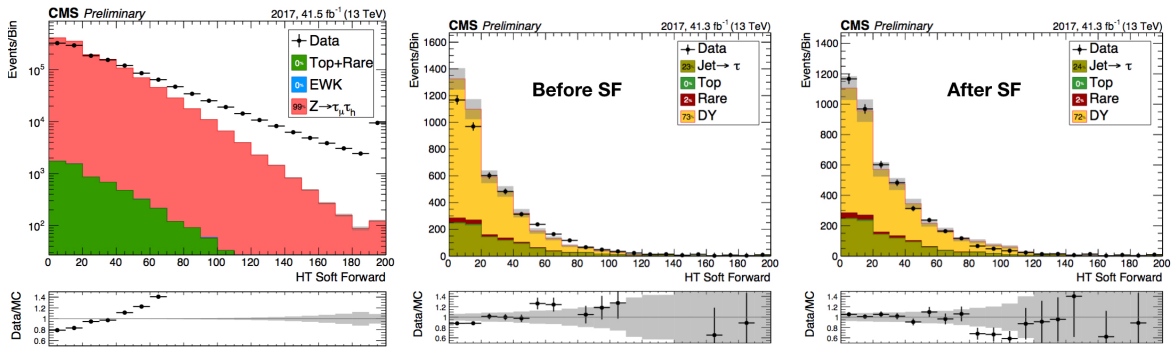


Figure 70: The left plot above shows the 2017 data/MC agreement for H_T (Soft,Forward) in a di-muon validation region. The large discrepancies in the tail are verified to be coming from Eras E and F. This issue is due to the noise in the forward ECAL readout system. We measure scale-factors in this channel and apply them in the di- τ_h channel. The effect of the scale factor can be seen by comparing the unweighted H_T (Soft,Forward) in the di- τ_h region (middle) to the post-weighting distribution (right).

651 **I Additional Validation Regions**

Table 16: Additional Validation Regions for the 2016 datasets

Search Region	Fake	DY	Top	Rare	Total Pred.	Obs
Low M_{T2} VR						
300 < $\sum M_T, N_J = 0$	4.08 ± 1.41 ± 2.67	26.9 ± 5.59 ± 9.24	0.154 ± 0.0755 ± 0.0396	0.509 ± 0.288 ± 0.238	31.6 ± 5.78 ± 9.62	25
300 < $\sum M_T, N_J >= 1$	2.88 ± 0.991 ± 1.86	6.83 ± 1.82 ± 3.19	0.941 ± 0.199 ± 0.475	1.15 ± 0.387 ± 0.682	11.8 ± 2.12 ± 3.78	14
250 < $\sum M_T < 300, N_J = 0$	3.55 ± 1.38 ± 1.78	21.9 ± 4.91 ± 6.15	0.788 ± 0.195 ± 0.347	1.2 ± 0.495 ± 0.546	27.4 ± 5.13 ± 6.44	27
250 < $\sum M_T < 300, N_J >= 1$	4 ± 1.23 ± 2.02	11.9 ± 2.91 ± 3.86	1.25 ± 0.224 ± 0.599	0.734 ± 0.287 ± 0.55	17.8 ± 3.18 ± 4.43	17
200 < $\sum M_T < 250, N_J = 0$	19.4 ± 3.14 ± 4.46	50.4 ± 7.91 ± 17	1.72 ± 0.276 ± 0.492	1.26 ± 0.475 ± 0.741	72.8 ± 8.53 ± 17.6	84
200 < $\sum M_T < 250, N_J >= 1$	15.8 ± 2.35 ± 7.36	22.9 ± 3.71 ± 6.98	4.05 ± 0.403 ± 1.51	2.96 ± 0.674 ± 1.14	45.7 ± 4.46 ± 10.3	25
High M_{T2} Same-Sign VR						
300 < $\sum M_T, N_J = 0$	0.743 ± 0.398 ± 0.403	< .7	< .2	0.0348 ± 0.0233 ± 0.0514	0.777 ± 0.399 ± 0.406	1
300 < $\sum M_T, N_J >= 1$	0.702 ± 0.478 ± 0.25	< .7	0.0952 ± 0.0561 ± 0.0238	0.149 ± 0.0493 ± 0.0841	0.945 ± 0.484 ± 0.265	0
250 < $\sum M_T < 300, N_J = 0$	0.234 ± 0.721 ± 0.316	< .7	< .2	0.0524 ± 0.0263 ± 0.0512	0.287 ± 0.722 ± 0.32	4
250 < $\sum M_T < 300, N_J >= 1$	2.28 ± 1.05 ± 0.372	< .7	0.082 ± 0.0519 ± 0.0796	0.062 ± 0.0283 ± 0.0755	2.43 ± 1.06 ± 0.388	2
200 < $\sum M_T < 250, N_J = 0$	5.57 ± 1.75 ± 1.17	< .7	0.0365 ± 0.0365 ± 0.0131	0.0389 ± 0.0219 ± 0.0285	5.65 ± 1.75 ± 1.17	7
200 < $\sum M_T < 250, N_J >= 1$	11.8 ± 2.44 ± 0.784	< .7	0.132 ± 0.0888 ± 0.0929	0.151 ± 0.0445 ± 0.0735	12.1 ± 2.44 ± 0.793	9
Low M_{T2} Same-Sign VR						
300 < $\sum M_T, N_J = 0$	1.24 ± 0.644 ± 0.382	< .7	< .2	0.106 ± 0.0368 ± 0.0482	1.34 ± 0.645 ± 0.385	2
300 < $\sum M_T, N_J >= 1$	3.33 ± 0.916 ± 1.8	< .7	0.0245 ± 0.00595 ± 0.0565	0.421 ± 0.077 ± 0.197	3.77 ± 0.919 ± 1.81	3
250 < $\sum M_T < 300, N_J = 0$	2.97 ± 0.963 ± 0.78	1.95 ± 1.53 ± 0.482	< .7	0.129 ± 0.0409 ± 0.0658	5.05 ± 1.8 ± 0.919	2
250 < $\sum M_T < 300, N_J >= 1$	3.3 ± 1.2 ± 0.467	0.375 ± 0.375 ± 0.181	0.296 ± 0.113 ± 0.14	0.441 ± 0.079 ± 0.179	4.41 ± 1.27 ± 0.55	3
200 < $\sum M_T < 250, N_J = 0$	18.9 ± 2.92 ± 1.28	1.51 ± 0.878 ± 1.68	0.152 ± 0.0902 ± 0.107	0.257 ± 0.0596 ± 0.187	20.8 ± 3.06 ± 2.13	14
200 < $\sum M_T < 250, N_J >= 1$	19.7 ± 2.9 ± 4.04	< .7	0.787 ± 0.177 ± 0.401	0.97 ± 0.223 ± 0.3	21.4 ± 2.91 ± 4.07	18
High M_{T2} B-Enriched VR						
300 < $\sum M_T, N_J >= 1$	2.52 ± 0.989 ± 1.72	< .7	4.66 ± 0.467 ± 1.92	0.0962 ± 0.0357 ± 0.0449	7.27 ± 1.09 ± 2.58	12
250 < $\sum M_T < 300, N_J >= 1$	4.31 ± 1.31 ± 2.5	0.37 ± 0.37 ± 0.232	8.14 ± 0.625 ± 3.22	0.0511 ± 0.0255 ± 0.0438	12.9 ± 1.5 ± 4.09	11
200 < $\sum M_T < 250, N_J >= 1$	6.33 ± 1.97 ± 1.94	1.97 ± 1.06 ± 2.84	11.1 ± 0.723 ± 3.57	0.341 ± 0.122 ± 0.188	19.7 ± 2.36 ± 4.96	20
Low M_{T2} B-Enriched VR						
300 < $\sum M_T, N_J >= 1$	3.82 ± 1.07 ± 2.75	0.777 ± 0.55 ± 1.52	14.2 ± 0.823 ± 4.27	0.726 ± 0.321 ± 0.269	19.6 ± 1.49 ± 5.31	12
250 < $\sum M_T < 300, N_J >= 1$	2.89 ± 1.67 ± 1.44	2.45 ± 1.11 ± 1.88	20.3 ± 0.971 ± 5.58	0.15 ± 0.0373 ± 0.228	25.8 ± 2.22 ± 6.07	29
200 < $\sum M_T < 250, N_J >= 1$	17.6 ± 2.91 ± 10.3	5.85 ± 1.69 ± 3.59	55.2 ± 1.62 ± 14.3	1.5 ± 0.483 ± 0.658	80.2 ± 3.77 ± 18	59
High M_{T2} , Small $\Delta\phi$ VR						
300 < $\sum M_T, N_J = 0$	0 ± 0.416 ± 0.336	< .7	< .2	1.92 ± 0.122 ± 0.441	1.82 ± 0.433 ± 0.554	3
300 < $\sum M_T, N_J >= 1$	0.714 ± 0.898 ± 0.0551	1.58 ± 0.918 ± 1.32	0.106 ± 0.0596 ± 0.0531	2.23 ± 0.271 ± 0.557	4.63 ± 1.31 ± 1.44	9
250 < $\sum M_T < 300, N_J = 0$	2.12 ± 0.78 ± 1.27	0.658 ± 0.658 ± 0.17	0.0859 ± 0.0859 ± 0.0629	0.621 ± 0.072 ± 0.137	3.49 ± 1.03 ± 1.29	0
250 < $\sum M_T < 300, N_J >= 1$	2.23 ± 1.26 ± 1.01	9.18 ± 2.31 ± 6.19	0.0781 ± 0.0531 ± 0.145	0.926 ± 0.116 ± 0.275	12.4 ± 2.64 ± 6.28	5
200 < $\sum M_T < 250, N_J = 0$	5.1 ± 1.87 ± 2.01	1.18 ± 0.836 ± 1.71	0.0753 ± 0.0753 ± 0.0898	0.422 ± 0.0609 ± 0.12	6.78 ± 2.05 ± 2.64	12
200 < $\sum M_T < 250, N_J >= 1$	19.3 ± 3.49 ± 4.82	22 ± 3.58 ± 24.2	0.723 ± 0.189 ± 0.238	1.72 ± 0.315 ± 0.425	43.8 ± 5.02 ± 24.7	41

652 **J Systematic Checks**

- 653 Figs. 71, show the post-fit (floating r) covariance matrices for the background-only and signal+background Asimov datasets.
- 654 Figs. 72, 73, show the post-fit constraints on the most significant sources of uncertainty in the analysis. Only the fake rate systematic appears to be constrained (at the order of $\approx 50\%$). Moreover, the fake rate appears underestimated in the signal regions as we see a small positive shift on the nuisance.

Table 17: Additional Validation Regions for the 2017 datasets

Search Region	Fake	DY	Top	Rare	Total Pred.	Obs
Low M_{T2} VR						
$300 < \sum M_T, N_j = 0$	$0.942 \pm 1.31 \pm 0.22$	$16.9 \pm 4.95 \pm 7.39$	$0.413 \pm 0.298 \pm 0.137$	$0.67 \pm 0.361 \pm 0.631$	$18.9 \pm 5.14 \pm 7.42$	29
$300 < \sum M_T, N_j >= 1$	$3.32 \pm 1.34 \pm 2.47$	$4.22 \pm 1.25 \pm 3.28$	$0.443 \pm 0.377 \pm 0.186$	$4.24 \pm 1.04 \pm 1.33$	$12.2 \pm 2.15 \pm 4.32$	16
$250 < \sum M_T < 300, N_j = 0$	$2.93 \pm 1.47 \pm 0.965$	$13.8 \pm 4.05 \pm 8.51$	$0.0582 \pm 0.0582 \pm 0.2$	$0.644 \pm 0.359 \pm 0.274$	$17.4 \pm 4.32 \pm 8.57$	21
$250 < \sum M_T < 300, N_j >= 1$	$1.49 \pm 1.03 \pm 0.319$	$12 \pm 3.15 \pm 3.31$	$0.00149 \pm 0.00111 \pm 0.00701$	$2.18 \pm 0.696 \pm 1.01$	$15.7 \pm 3.38 \pm 3.48$	16
$200 < \sum M_T < 250, N_j = 0$	$12.9 \pm 3.1 \pm 3.53$	$43.2 \pm 7.56 \pm 18.6$	$0.546 \pm 0.37 \pm 0.732$	$1.49 \pm 0.575 \pm 0.902$	$58.2 \pm 8.2 \pm 19$	56
$200 < \sum M_T < 250, N_j >= 1$	$11.3 \pm 2.37 \pm 4.27$	$15.4 \pm 2.62 \pm 4.46$	$1.94 \pm 0.808 \pm 1.41$	$2.54 \pm 0.708 \pm 1.42$	$31.2 \pm 3.69 \pm 6.49$	26
High M_{T2} Same-Sign VR						
$300 < \sum M_T, N_j = 0$	$0.679 \pm 0.404 \pm 0.413$	< 1	$< .2$	$0.0101 \pm 0.00224 \pm 0.00388$	$0.689 \pm 0.404 \pm 0.413$	1
$300 < \sum M_T, N_j >= 1$	$1.42 \pm 0.782 \pm 0.214$	< 1	$0.0125 \pm 0.0046 \pm 0.0082$	$0.0362 \pm 0.0209 \pm 0.00878$	$1.47 \pm 0.782 \pm 0.214$	0
$250 < \sum M_T < 300, N_j = 0$	$0.858 \pm 0.906 \pm 0.668$	< 1	$< .2$	$0.0117 \pm 0.00223 \pm 0.00417$	$0.869 \pm 0.906 \pm 0.668$	5
$250 < \sum M_T < 300, N_j >= 1$	$2.7 \pm 1.12 \pm 0.0236$	< 1	$0.00382 \pm 0.00237 \pm 0.00563$	$0.0123 \pm 0.00245 \pm 0.00588$	$2.71 \pm 1.12 \pm 0.0249$	0
$200 < \sum M_T < 250, N_j = 0$	$2.01 \pm 1.36 \pm 1.81$	< 1	$< .2$	$0.0146 \pm 0.00257 \pm 0.00651$	$2.03 \pm 1.36 \pm 1.81$	4
$200 < \sum M_T < 250, N_j >= 1$	$7.64 \pm 2.05 \pm 0.46$	< 1	$0.000815 \pm 0.000815 \pm 0.000751$	$0.0163 \pm 0.00283 \pm 0.0156$	$7.65 \pm 2.05 \pm 0.46$	4
Low M_{T2} Same-Sign VR						
$300 < \sum M_T, N_j = 0$	$1.11 \pm 0.573 \pm 0.457$	< 1	$< .2$	$0.0232 \pm 0.0032 \pm 0.00761$	$1.13 \pm 0.573 \pm 0.457$	1
$300 < \sum M_T, N_j >= 1$	$2.51 \pm 0.846 \pm 1.37$	< 1	$0.0315 \pm 0.007 \pm 0.0734$	$0.241 \pm 0.161 \pm 0.0603$	$2.78 \pm 0.861 \pm 1.37$	2
$250 < \sum M_T < 300, N_j = 0$	$0.0864 \pm 0.769 \pm 2.2$	< 1	$< .2$	$0.0178 \pm 0.00291 \pm 0.00455$	$0.104 \pm 0.769 \pm 2.2$	2
$250 < \sum M_T < 300, N_j >= 1$	$3.06 \pm 1.13 \pm 0.798$	< 1	$0.343 \pm 0.226 \pm 0.413$	$0.0418 \pm 0.00446 \pm 0.011$	$3.45 \pm 1.15 \pm 0.899$	3
$200 < \sum M_T < 250, N_j = 0$	$17.5 \pm 3.14 \pm 3.68$	< 1	$0.000345 \pm 0.000345 \pm 0.000848$	$0.0495 \pm 0.0048 \pm 0.0135$	$17.6 \pm 3.14 \pm 3.68$	17
$200 < \sum M_T < 250, N_j >= 1$	$11.3 \pm 2.52 \pm 2.43$	< 1	$0.0379 \pm 0.00778 \pm 0.0201$	$0.956 \pm 0.439 \pm 0.267$	$12.3 \pm 2.56 \pm 2.44$	12
High M_{T2} B-Enriched VR						
$300 < \sum M_T, N_j >= 1$	$0.535 \pm 0.743 \pm 0.134$	< 1	$4.25 \pm 1.37 \pm 0.9$	$0.237 \pm 0.185 \pm 0.182$	$5.03 \pm 1.57 \pm 0.928$	7
$250 < \sum M_T < 300, N_j >= 1$	$3.02 \pm 1.16 \pm 1.46$	$0.471 \pm 0.471 \pm 0.416$	$6.57 \pm 1.63 \pm 4.35$	$0.449 \pm 0.394 \pm 0.628$	$10.5 \pm 2.09 \pm 4.65$	8
$200 < \sum M_T < 250, N_j >= 1$	$6.07 \pm 1.54 \pm 3.13$	$0.974 \pm 0.691 \pm 1.6$	$6.06 \pm 1.61 \pm 2.31$	$0.294 \pm 0.205 \pm 0.534$	$13.4 \pm 2.34 \pm 4.24$	8
Low M_{T2} B-Enriched VR						
$300 < \sum M_T, N_j >= 1$	$1.82 \pm 0.894 \pm 1.09$	$1.2 \pm 0.949 \pm 1.46$	$9.85 \pm 1.81 \pm 4.41$	$2.1 \pm 0.915 \pm 0.759$	$15 \pm 2.41 \pm 4.83$	9
$250 < \sum M_T < 300, N_j >= 1$	$4.54 \pm 1.33 \pm 3.19$	$2.07 \pm 1 \pm 2.42$	$17.8 \pm 2.6 \pm 6.85$	$0.692 \pm 0.385 \pm 0.929$	$25.1 \pm 3.12 \pm 7.99$	17
$200 < \sum M_T < 250, N_j >= 1$	$10.4 \pm 2.54 \pm 5.48$	$6.17 \pm 2.01 \pm 4.01$	$32.5 \pm 3.34 \pm 7.44$	$2.1 \pm 0.804 \pm 1.39$	$51.1 \pm 4.72 \pm 10.2$	46
High M_{T2} , Small $\Delta\phi$ VR						
$300 < \sum M_T, N_j = 0$	$0.949 \pm 0.521 \pm 0.488$	$1e-07 \pm 0 \pm 2e-07$	$0.000895 \pm 0.000895 \pm 0.000192$	$1.81 \pm 0.405 \pm 0.388$	$2.75 \pm 0.66 \pm 0.623$	0
$300 < \sum M_T, N_j >= 1$	$1.04 \pm 1.02 \pm 0.359$	$6.98 \pm 2.07 \pm 3.91$	$0.00474 \pm 0.0022 \pm 0.00127$	$1.87 \pm 0.455 \pm 0.42$	$9.9 \pm 2.36 \pm 3.95$	11
$250 < \sum M_T < 300, N_j = 0$	$0.91 \pm 0.692 \pm 0.0505$	$3.11 \pm 1.95 \pm 4.28$	$0.00202 \pm 0.00202 \pm 0.00121$	$0.354 \pm 0.21 \pm 0.16$	$4.38 \pm 2.08 \pm 4.28$	2
$250 < \sum M_T < 300, N_j >= 1$	$3.36 \pm 1.61 \pm 0.821$	$9.1 \pm 2.5 \pm 6.48$	$0.00101 \pm 0.00101 \pm 0.00114$	$0.751 \pm 0.302 \pm 1.07$	$13.2 \pm 2.99 \pm 6.57$	17
$200 < \sum M_T < 250, N_j = 0$	$1.59 \pm 1.02 \pm 0.466$	$1.26 \pm 0.936 \pm 3.79$	$1e-07 \pm 0 \pm 0$	$0.106 \pm 0.0238 \pm 0.0502$	$2.95 \pm 1.38 \pm 3.81$	5
$200 < \sum M_T < 250, N_j >= 1$	$4.07 \pm 2.45 \pm 2.92$	$22 \pm 3.86 \pm 9.69$	$0.492 \pm 0.491 \pm 0.116$	$1.13 \pm 0.425 \pm 0.906$	$27.7 \pm 4.62 \pm 10.2$	43

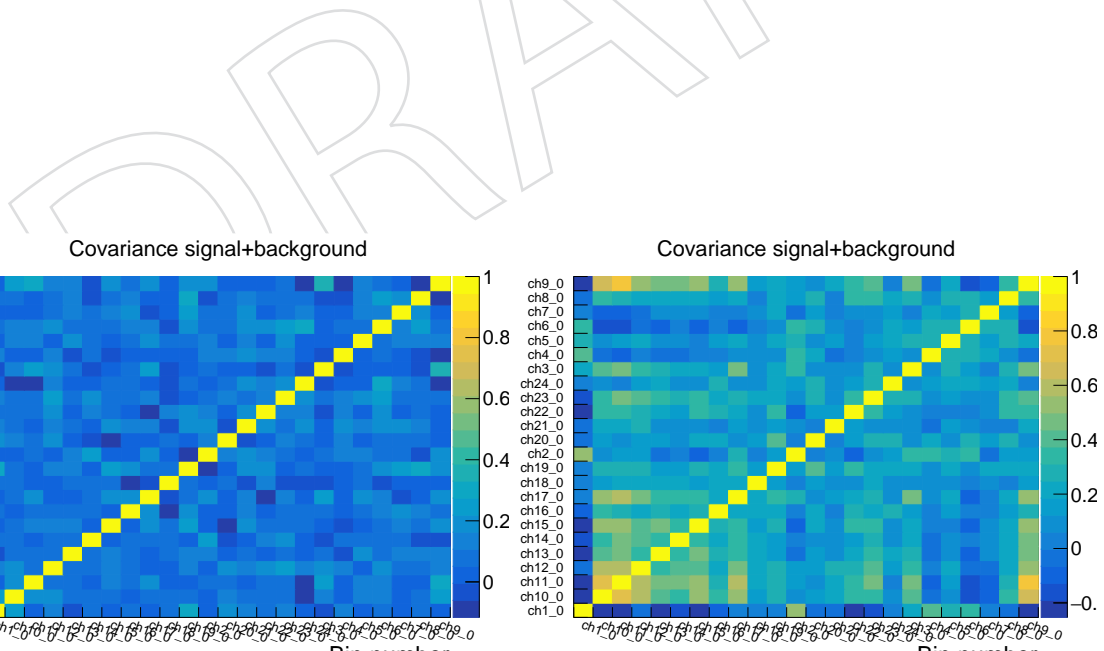


Figure 71: Post-fit (floating r) covariance matrices for the background-only (right) and background+signal (left) Asimov datasets.

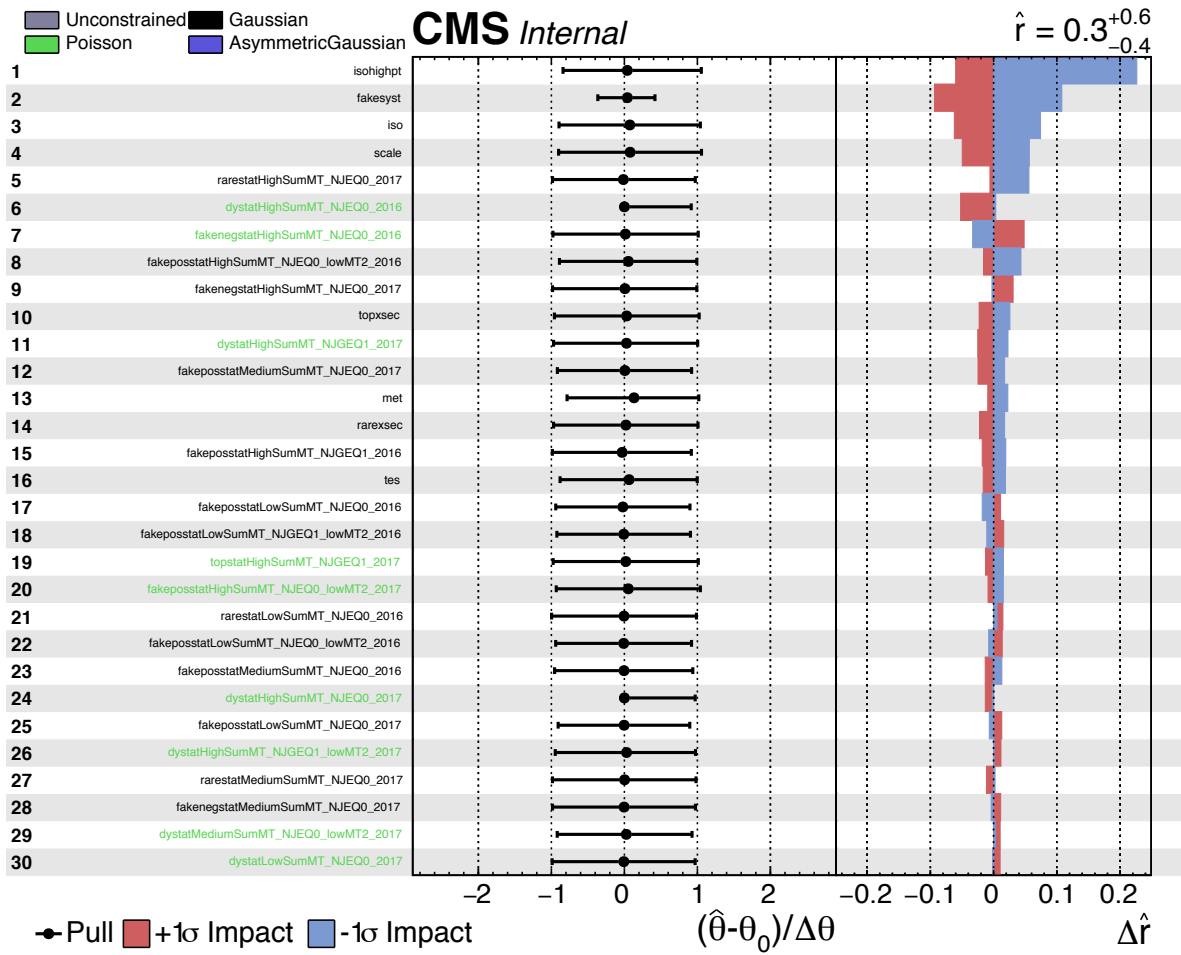


Figure 72: Impact plot for background-only Asimov dataset.

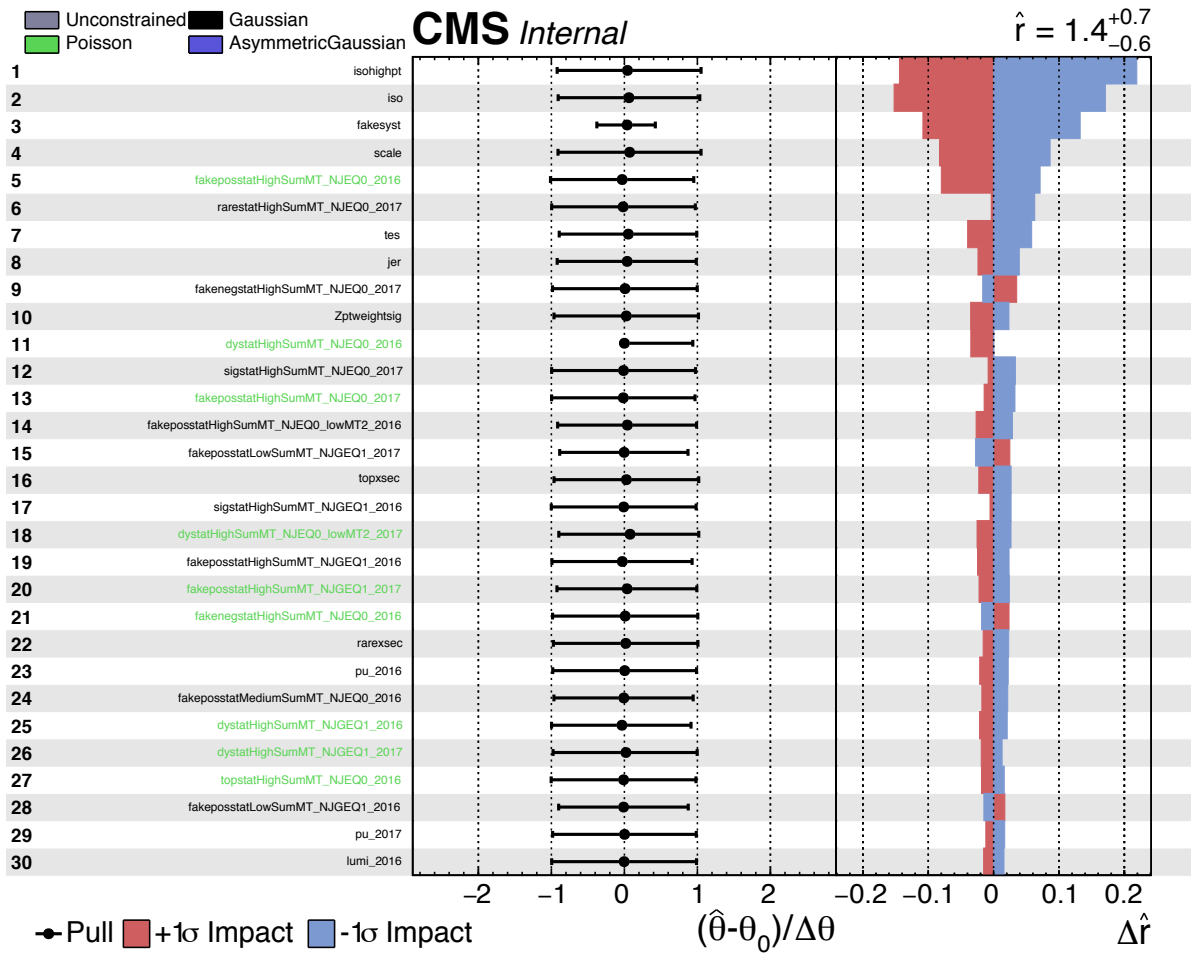


Figure 73: Impact plot for signal+background Asimov dataset.